

## PAPER NAME

**FP2 Draft\_Revised (2).docx**

## WORD COUNT

**22344**

## RESULTS COUNT

**29**

## SUBMISSION DATE

**8 Jul 2025, 11:31:08 pm GMT+7**

## REPORT DATE

**8 Jul 2025, 11:40:27 pm GMT+7****1%**

The combined total of all matches, including overlapping sources, for each database.

## Results

The results include any sources we have found in your submitted document that includes the following: identical text and slightly changed text.

<b>1. hal.science</b> <a href="https://hal.science/hal-01571683v1/html_references">https://hal.science/hal-01571683v1/html_references</a>	100%
<b>2. www.mdpi.com</b> <a href="https://www.mdpi.com/2226-4310/8/6/161/reprints">https://www.mdpi.com/2226-4310/8/6/161/reprints</a>	92%
<b>3. www.mdpi.com</b> <a href="https://www.mdpi.com/2073-4441/15/10/1824/reprints">https://www.mdpi.com/2073-4441/15/10/1824/reprints</a>	91%
<b>4. www.icao.int</b> <a href="https://www.icao.int/safety/meteorology/amofsg/amofsg%20meeting%20material/amofsg.9.sn.015.5.en.pdf">https://www.icao.int/safety/meteorology/amofsg/amofsg%20meeting%20material/amofsg.9.sn.015.5.en.pdf</a>	88%
<b>5. www.faa.gov</b> <a href="https://www.faa.gov/sites/faa.gov/files/2022-11/NTSReport.pdf">https://www.faa.gov/sites/faa.gov/files/2022-11/NTSReport.pdf</a>	86%
<b>6. link.springer.com</b> <a href="https://link.springer.com/content/pdf/10.1007/978-1-84628-812-8_9">https://link.springer.com/content/pdf/10.1007/978-1-84628-812-8_9</a>	83%
<b>7. www.grafinati.com</b> <a href="https://www.grafinati.com/en/literature-selections/simulation-mcmc/">https://www.grafinati.com/en/literature-selections/simulation-mcmc/</a>	83%
<b>8. digitalcommons.calpoly.edu</b> <a href="https://digitalcommons.calpoly.edu/stat_fac/27/">https://digitalcommons.calpoly.edu/stat_fac/27/</a>	75%
<b>9. www.scribd.com</b> <a href="https://www.scribd.com/document/57371814/TC1-237">https://www.scribd.com/document/57371814/TC1-237</a>	74%
<b>10. mediatum.ub.tum.de</b> <a href="https://mediatum.ub.tum.de/603830?nodes_per_page=10&amp;sortfield0=-type&amp;sortfield1=title&amp;change_language=en&amp;searchmode=ex">https://mediatum.ub.tum.de/603830?nodes_per_page=10&amp;sortfield0=-type&amp;sortfield1=title&amp;change_language=en&amp;searchmode=ex</a>	72%
<b>11. groundschool.weebly.com</b> <a href="https://groundschool.weebly.com/uploads/2/3/6/7/2367787/2223_nbd_other_np_approaches.pdf">https://groundschool.weebly.com/uploads/2/3/6/7/2367787/2223_nbd_other_np_approaches.pdf</a>	71%

**12. sites.google.com**

<https://sites.google.com/view/how-many-black-boxes-are-on/>

70%

**13. courses.grainger.illinois.edu**

<https://courses.grainger.illinois.edu/ece541/fa2016/state-space-complete.pdf>

70%

**14. arc.aiaa.org**

<https://arc.aiaa.org/doi/pdf/10.2514/6.2022-3778>

69%

**15. en.wikipedia.org**

[https://en.wikipedia.org/wiki/Instrument\\_approach](https://en.wikipedia.org/wiki/Instrument_approach)

69%

**16. theses.hal.science**

[https://theses.hal.science/tel-00865829v1/html\\_references](https://theses.hal.science/tel-00865829v1/html_references)

68%

**17. www.scribd.com**

<https://www.scribd.com/document/57371814/TC1-237>

67%

**18. isjem.com**

<https://isjem.com/download/marker-beacon/>

66%

**19. www.faa.gov**

[https://www.faa.gov/regulations\\_policies/rulemaking/committees/documents/media/TAOARC-2192002.pdf](https://www.faa.gov/regulations_policies/rulemaking/committees/documents/media/TAOARC-2192002.pdf)

65%

**20. meetingorganizer.copernicus.org**

<https://meetingorganizer.copernicus.org/EGU24/EGU24-1427.html>

65%

**21. lib.hku.hk**

[https://lib.hku.hk/files/general/research/guides/HK\\_AviationBib.pdf](https://lib.hku.hk/files/general/research/guides/HK_AviationBib.pdf)

64%

**22. www.scribd.com**

<https://www.scribd.com/document/98399360/Causation-Factors-for-the-Banjar-Panji-No-1-Blowout-Neil-Adams-C>

63%

**23. medium.com**

<https://medium.com/@paulynnat/ground-school-day-2-pitch-roll-yaw-bde00ffec015>

62%

**24. www.iris.unict.it**

[https://www.iris.unict.it/retrieve/dfe4d227-a8d2-bb0a-e053-d805fe0a78d9/jucs\\_palesi.pdf](https://www.iris.unict.it/retrieve/dfe4d227-a8d2-bb0a-e053-d805fe0a78d9/jucs_palesi.pdf)

62%

**25. webthesis.biblio.polito.it**

<https://webthesis.biblio.polito.it/34310/1/tesi.pdf>

61%

**26. albrechtlawfirm.com**

<https://albrechtlawfirm.com/aviation-accidents/>

61%

**27. www.icao.int**

[https://www.icao.int/safety/airnavigation/AIG/Documents/ADREP%20Taxonomy/ECCAIRS%20Aviation%201.3.0.12%20\(VL%20for%20-%20Event%20Phase%20-%20Pha](https://www.icao.int/safety/airnavigation/AIG/Documents/ADREP%20Taxonomy/ECCAIRS%20Aviation%201.3.0.12%20(VL%20for%20-%20Event%20Phase%20-%20Pha)

61%

**28. appliedmath.arizona.edu**

[https://appliedmath.arizona.edu/sites/default/files/0f04d86a836182cbf608dfc86c7a70f5e5f6\\_0.pdf](https://appliedmath.arizona.edu/sites/default/files/0f04d86a836182cbf608dfc86c7a70f5e5f6_0.pdf)

61%

**29. mcp.dev.academyart.edu**

<https://mcp.dev.academyart.edu/controls-of-aircraft>

61%

**Scanned Text**

Risk Quantification Of Aerodynamic Stall and In-Flight Loss Of Control (LOC-I) Events During Aircraft Approach

Final Project

Submitted as one of the requirements to obtain a bachelor's degree in

Aerospace Engineering from the Bandung Institute of Technology

By:

**Daniel Alexander**

**13621021**

Supervisor:

**Dr. -Ing. Ir. Javensius Sembiring**



Aerospace Engineering Program

Faculty of Mechanical and Aerospace Engineering

Institut Teknologi Bandung

2025

**Abstract**

Risk Quantification Of Aerodynamic Stall and In-Flight Loss Of Control (LOC-I) Events During Aircraft Approach

By:

**Daniel Alexander**

**13621021**

This thesis employs high-resolution QAR data to forecast aerodynamic stall and in-flight loss of control probability during the final approach phase of Boeing 747-300s. It presents a modeling framework as it calculates the aircraft's total mechanical energy based on the relationships between physical force and motion, comparing measured and simulated energy trajectories throughout a 95 s interval preceding touchdown. Subset simulation utilizing Markov Chain Monte Carlo (MCMC) sampling is implemented to evaluate the likelihood of the failure event, defined by the aircraft's energy dropping below a threshold determined by impaired conditions. The baseline overall failure probability is assessed to be around  $3.57 \times 10^{-6}$ , while the dynamic, per-second evolution is estimated to be an exponential decay (of base 10) towards zero. Two sensitivity analyses are conducted to evaluate the influences of parameters, specifically angle of attack, crosswind speed, and N<sub>1</sub> fan speed, which are the primary factors contributing to the failure event. A mitigation plan is formulated by increasing approach speed by 10 knots while decreasing pitch and angle of attack, resulting in a 45.56% reduction in the probability of LOC-I.

Keywords: *Rare Event, Subset Simulation, Risk Quantification, Final Approach, Loss of Control In-Flight*

**Approval Sheet**

RISK Quantification Of Aerodynamic Stall and IN-FLIGHT Loss Of Control (LOC-I) EVENTS During AIRCRAFT Approach

By:

**Daniel Alexander**

**13621021**

Aerospace Engineering Program

Faculty of Mechanical and Aerospace Engineering

Institut Teknologi Bandung

Has reviewed and approved,

On 2 July 2025

Supervisor

**Dr. -Ing, Ir. Javensius Sembiring**

**NIP: 19810121 201404 1 001**

**Foreword**

First and foremost, all praise to the Lord, God Almighty, I thank Him for His grace and the abundant blessings, knowledge, and opportunities He has given me over my study here at ITB. For their constant love and unflinching belief in me in these past four years, I also want to thank and dedicate this work to my mother Suprihatin and father Rudy Wihardja. Without their ongoing and enduring support, I would not be where I am right now as of writing this.

I am also grateful for my friends in the class of AE 2021, and all other peers I have met outside it and had the pleasure of working with. Special thanks also go to Jason and Rivan for sharing their work on similar topics as well as Dimas Rifqi Mahendra for your master's Thesis as a guide on this research. To all of you, I appreciate your support throughout the years and hope for the best of luck in your futures whatever it may be.

Without the great support and direction of my supervisor, Dr. Javensius Sembiring, whose knowledge of risk quantification gave strong insights and paths for this project, this research would not have been feasible therefore I offer gratitude for the opportunity, mentorship, and access to flight data for this endeavor. I wish him well and may God bless you in your future lectures and research at ITB.

The work of this thesis started with a passion for statistics to better understand the modus operandi of risk quantification. Using stochastic approaches instead of a deterministic one (specifically subset simulation) provided a fresh and demanding way to address this issue of estimating very small probabilities. I hope to you who reads this, who are intrigued or are studying this area of interest can find some use in this work. Thank you.

Bandung, 26 May 2025



Daniel Alexander

Author

## Table Of Contents

[Abstract ii](#)

[Approval Sheet ii](#)

[Foreword iii](#)

[Table Of Contents iv](#)

[List Of Tables vii](#)

[List Of Figures viii](#)

[Chapter 1 Introduction 1](#)

[1.1 Background 1](#)

[1.2 Key Issues 2](#)

[1.3 Objectives 3](#)

[1.4 Scope 3](#)

[1.5 Methodology 3](#)

[1.6 Structure Overview 5](#)

[Chapter 2 Basic Theory and Literature Study 6](#)

[2.1 Theoretical Basis 6](#)

[2.1.1 Aerodynamic Stall and Loss of Control \(LOC\) 6](#)

[2.1.2 Instrument Approach Procedure for Transport Aircraft 7](#)

[2.1.3 Probability Theory for Continuous Random Variables 8](#)

[2.1.4 Stochastic Processes and Markov Chains 11](#)

[2.1.5 Markov Chain Monte Carlo \(MCMC\) 12](#)

[2.1.6 Subset Simulation 14](#)

[2.2 Literature Review 15](#)

[2.3.1 Monte Carlo Methods in Risk Assessment 15](#)

[2.3.2 MCMC Methods in Risk Assessment 16](#)

[2.3.3 Subset Simulation in Risk Assessment 17](#)

[2.3 Research Gap and Framework 17](#)

[Chapter 3 Data Gathering and Preprocessing 18](#)

[3.1 Preprocessing Framework 18](#)

[3.1.1 Raw Data Overview 18](#)

[3.1.2 Preprocessing Steps 20](#)

[3.1.3 MATLAB Algorithm 21](#)

[3.2 Categorization of Flight Phases \(Time Points Identification\) 22](#)

[3.2.1 Criteria for Each Time Point 22](#)

[3.2.2 Time Points Results 25](#)

[3.2.3 Validation of Approach Time Points 28](#)

[3.3 Parameter Measurements at Approach 28](#)

[3.3.1 Candidate Parameters for Measurement 29](#)

[3.3.2 Measurement Results and Analysis at TP5 34](#)

[3.3.3 Measurement Results and Analysis at TP6 37](#)

[Chapter 4 Modelling and Simulation 40](#)

[4.1 Modelling 40](#)

[4.1.1 Model Formulation 40](#)

[4.1.2 Model Simulation 42](#)

[4.1.3 Model Validation 45](#)

[4.1.4 Residual Analysis 47](#)

<a href="#">4.2 Implementation 50</a>
<a href="#">4.2.1 Incident Threshold Assessment 50</a>
<a href="#">4.2.2 Subset Simulation Process 52</a>
<a href="#">4.2.3 Iterative Per-Second Simulation 55</a>
<a href="#">4.2.4 Manual Sensitivity Analysis 57</a>
<a href="#">4.2.5 Toolbox-Assisted Sensitivity Analysis 59</a>

## [Chapter 5 Results and Analysis 63](#)

<a href="#">5.1 Simulation Results 63</a>
<a href="#">5.1.1 Probability Types 63</a>
<a href="#">5.1.2 Risk Scenarios 64</a>
<a href="#">5.1.3 Dynamic Failure Probability 66</a>
<a href="#">5.2 Contributing Factors Breakdown 67</a>
<a href="#">5.2.1 Landing Weight 67</a>
<a href="#">5.2.2 Engine Performance 68</a>
<a href="#">5.2.3 Attitude and Aerodynamic Angles 68</a>
<a href="#">5.2.4 Aircraft Velocity 69</a>
<a href="#">5.2.5 Control Surface Deflection 70</a>
<a href="#">5.2.6 Atmospheric Conditions 70</a>
<a href="#">5.2.7 Rankings Overview and Comparison 71</a>

## [5.3 Proposed Safety Improvement 72](#)

## [Chapter 6 Conclusions and Recommendation 76](#)

<a href="#">6.1 Conclusion 76</a>
<a href="#">6.2 Recommendations and Future Works 78</a>
<a href="#">6.2.1 Mitigation Strategy 78</a>
<a href="#">6.2.2 Future Works 78</a>

## [References 80](#)

## [Appendix A GitHub Repository 83](#)

### [A.1 MATLAB Code 83](#)

### [A.2 Data Files 83](#)

### [Appendix B Sensitivity Plots 84](#)

### [Appendix C Parameter Plots 87](#)

## **List Of Tables**

<a href="#">Table 3.1 Definition of Time Points 22</a>
<a href="#">Table 3.2 Definition of Measurements 28</a>
<a href="#">Table 3.3 TP5 Log Likelihood Values for Each Distribution Fit 34</a>
<a href="#">Table 3.4 Best Distribution Fits for TP5 Measurements 35</a>
<a href="#">Table 3.5 TP6 Log Likelihood Values for Each Distribution Fit 37</a>
<a href="#">Table 3.6 Best Distribution Fits for TP6 Measurements 37</a>
<a href="#">Table 4.1 Energy Area Distribution Comparison 47</a>
<a href="#">Table 4.2 Energy Area Distribution Fits 47</a>
<a href="#">Table 4.3 Ranking and P(F) Change from 10% Parameter Increase 59</a>
<a href="#">Table 4.4 Sensitivity Rankings of Parameters Based on Cumulative Score 62</a>
<a href="#">Table 5.1 List of Probabilities for LOC-I Scenarios 64</a>
<a href="#">Table 5.2 Comparison of Weight Parameters on LOC-I Risk 67</a>
<a href="#">Table 5.3 Comparison of Thrust Parameters on LOC-I Risk 68</a>
<a href="#">Table 5.4 Comparison of Aircraft Angles on LOC-I Risk 68</a>
<a href="#">Table 5.5 Comparison of Velocity Components on LOC-I Risk 69</a>
<a href="#">Table 5.6 Comparison of Control Surface Deflection on LOC-I Risk 70</a>
<a href="#">Table 5.7 Atmospheric Conditions on LOC-I Risk 71</a>
<a href="#">Table 5.8 Compiled Orders of Ranking on Parameter Significance 71</a>

## **List Of Figures**

<a href="#">Figure 1.1 Breakdown of Factors for 68 Fatal Accidents from 2011-2015 (IATA) 1</a>
<a href="#">Figure 1.2 Breakdown of LOC-I Fatal Accidents by Phase of Flight 2010-2014 (IATA) 2</a>
<a href="#">Figure 1.3 Research Flowchart 4</a>
<a href="#">Figure 2.1 C<sub>l</sub>-α Curve for Cambered Airfoil (Anderson, 2024) 6</a>

- [Figure 2.2 Approach Segments and Obstacle Clearance \(FAA\) 7](#)  
[Figure 2.3 KMSP Runway 30R ILS/LOC Approach Guide \(FAA\) 8](#)  
[Figure 2.4 CCDF Plot Construction 11](#)  
[Figure 3.1 Airport Sketch of KMSP \(FAA\) 18](#)  
[Figure 3.2 Origins of All Dataset Flights to KMSP 19](#)  
[Figure 3.3 Typical Flight Profile from Flight Data 19](#)  
[Figure 3.4 Data Plot Comparison \(Typical vs. Problematic\) 20](#)  
[Figure 3.5 Typical Profile of Trailing Flap Position 23](#)  
[Figure 3.6 Typical Profile of Flight ACMS 23](#)  
[Figure 3.7 Landing Minimums for ILS/LOC-I Approach onto KMSP Runway 30R \(FAA\) 24](#)  
[Figure 3.8 Typical Profile of Ground Speed 24](#)  
[Figure 3.9 Typical Profile of Weight on Wheels 25](#)  
[Figure 3.10 Range and Distribution of Flight Time 26](#)  
[Figure 3.11 Flight Phase Identification of Long Flight 26](#)  
[Figure 3.12 Flight Phase Identification of Intermediate Flight 27](#)  
[Figure 3.13 Flight Phase Identification of Short Flight 27](#)  
[Figure 3.14 Range and Distribution of Durations TP5 \(left\) or TP6 \(right\) With TP7 28](#)  
[Figure 3.15 Typical Profile of Pitch Angle 29](#)  
[Figure 3.16 Typical Profile of Roll Angle 30](#)  
[Figure 3.17 Typical Profile of Vertical Speed 30](#)  
[Figure 3.18 Typical Profile of Wind Direction 31](#)  
[Figure 3.19 Typical Profile of Magnetic Heading 31](#)  
[Figure 3.20 Typical Profile of Wind Speed 32](#)  
[Figure 3.21 Extrapolated Profile of Crosswind 32](#)  
[Figure 3.22 Extrapolated Profile of Head/Tailwind 33](#)  
[Figure 3.23 Typical Profile of Angle of Attack 33](#)  
[Figure 3.24 Typical Profile of Drift Angle 34](#)  
[Figure 3.25 GEV Fits onto M1 and M5 \(TP5\) 36](#)  
[Figure 3.26 GEV Fits onto M6 and M8 \(TP5\) 36](#)  
[Figure 3.27 Normal Fits onto M2 and M7 \(TP5\) 36](#)  
[Figure 3.28 Logistic Fits onto M3 and M4 \(TP5\) 37](#)  
[Figure 3.29 Normal Fits onto M1 and M2 \(TP6\) 38](#)  
[Figure 3.30 Normal Fits onto M5 and M8 \(TP6\) 38](#)  
[Figure 3.31 Logistic Fits onto M3 and M4 \(TP6\) 39](#)  
[Figure 3.32 \(left\) GEV Fit onto M6 and \(right\) Logistic Fit onto M7 \(TP6\) 39](#)  
[Figure 4.1 Range of Durations for Final Approach 43](#)  
[Figure 4.2 Total Energy Progression Based on Flight Data 43](#)  
[Figure 4.3 Comparison of Model-Based and Data-Based Total Energy 44](#)  
[Figure 4.4 Total Energy Comparison for a Singular Flight 44](#)  
[Figure 4.5 Final Approach Trajectories onto KMSP Runway 30R 45](#)  
[Figure 4.6 Cumulative Energy Comparison for Integration Upper Limit of \(left\) 90 s and \(right\) 100 s 46](#)  
[Figure 4.7 Cumulative Total Energy Comparison for 95 s Upper Integration Limit 46](#)  
[Figure 4.8 Residuals vs Time Plot 48](#)  
[Figure 4.9 Residuals vs Model Output Plot 49](#)  
[Figure 4.10 Cumulative Residuals \(or Q-Q\) Plot 49](#)  
[Figure 4.11 Comparison of Data and Altered Model-Based Total Energy 51](#)  
[Figure 4.12 Comparison of Data-Based Total Energy and Proposed LOC-I Threshold 51](#)  
[Figure 4.13 Total Energy Areas with LOC-I Threshold Depiction 52](#)  
[Figure 4.14 Outputs of Each Sampling Per Subset 53](#)  
[Figure 4.15 CCDF Plot for Output Energy Area 54](#)  
[Figure 4.16 Sample Acceptances in Each Subset 54](#)  
[Figure 4.17 Output Plots at T = 25 s \(left\) and T = 50 s \(right\) 56](#)  
[Figure 4.18 CCDF Plots for T = 25 s \(bottom\) and T = 50 s \(top\) 56](#)  
[Figure 4.19 Acceptance of Samples for T = 25 s \(left\) and T = 50 s \(right\) 57](#)  
[Figure 4.20 A 10% Increase in Threshold for Angle of Attack Data 58](#)  
[Figure 4.21 Graphical Comparison in P\(F\) Change by 10% Increase of Parameters 58](#)

[Figure 4.22 Sensitivity Plot for Angle of Attack at T = 25 s](#) 60

[Figure 4.23 Sensitivity Plot for Angle of Attack at T = 50 s](#) 60

[Figure 4.24 Progression of Sensitivity Scores on Final Approach](#) 61

[Figure 4.25 Cumulative Score Plot from Toolbox-Assisted Sensitivity Analysis](#) 61

[Figure 5.1 Model Energy Progression with Altered Airspeed](#) 63

[Figure 5.2 Airspeed Criteria Threshold for Total Energy Progression \(left\) and for Parameter Area \(right\)](#) 64

[Figure 5.3 Progression of P<sub>F</sub> During Final Approach](#) 66

[Figure 5.4 Proposed Change for LOC-I Threshold](#) 73

[Figure 5.5 P<sub>F</sub> Change After Safety Proposal](#) 73

[Figure 5.6 Estimated Time of Deceleration from Touchdown to V = 26 m/s](#) 74

[Figure 5.7 Estimated Deceleration Distance from Touchdown to V = 26 m/s](#) 75

[Figure B.1 Fuel Mass Sensitivity Plot at T = 25 s](#) 84

[Figure B.2 N<sub>1</sub> Sensitivity Plot at T = 25 s](#) 84

[Figure B.3 Airspeed Sensitivity Plot at T = 25 s](#) 85

[Figure B.4 Pitch Angle Sensitivity Plot at T = 25 s](#) 85

[Figure B.5 Roll Angle Sensitivity Plot at T = 25 s](#) 85

[Figure B.6 Elevator Deflection Sensitivity Plot at T = 25 s](#) 86

[Figure B.7 Crosswind Sensitivity Plot at T = 25 s](#) 86

[Figure C.1 Fuel Quantity Progression Plot](#) 87

[Figure C.2 N<sub>1</sub> Progression Plot](#) 87

[Figure C.3 Airspeed Progression Plot](#) 88

[Figure C.4 Angle of Attack Progression Plot](#) 88

[Figure C.5 Pitch Angle Progression Plot](#) 89

[Figure C.6 Roll Angle Progression Plot](#) 89

[Figure C.7 Crosswind Progression Plot](#) 90

[Figure C.8 Elevator Deflection Progression Plot](#) 90

[Figure C.9 Flap Deflection Progression Plot](#) 91

[Figure C.10 Air Density Progression Plot](#) 91

## Chapter 1

### Introduction

### Background

The aviation sector has continuously emphasized safety, following rigorous standards to mitigate risks. Nonetheless, loss of control<sup>(14)</sup> in-flight (LOC-I) continues to be a<sup>(14)</sup> predominant cause of<sup>(14)</sup> aviation incidents. Research conducted by the International Air Transport Association (IATA) [1] reveals that low airspeed stalls caused by environmental factors are common precursors to LOC-I incidents, notwithstanding improvements in aircraft technology and pilot training. The report indicates that the bulk of fatal accidents (incidents resulting in deaths) are attributed to this event, as illustrated in Figure 1.1. Therefore, the intricacy of these situations, pilot reactions, and the dynamic interplay of aircraft components renders the prediction and prevention of LOC-I difficult.

Oth  
12.

LOC-I  
45.5%

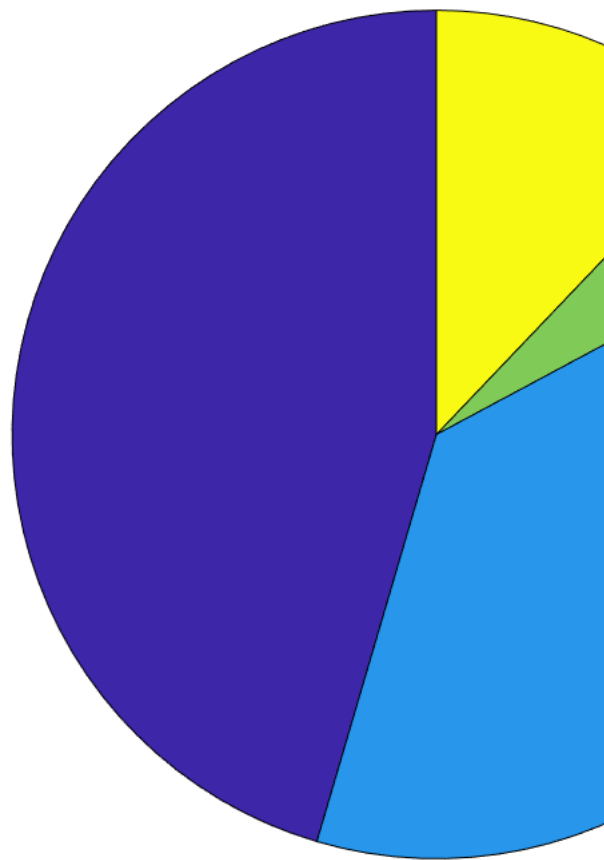


Figure 1.1 Breakdown of Factors for 68 Fatal Accidents from 2011-2015 (IATA)

The landing approach phase is among the most challenging parts of flight, marked by low airspeeds, diminished heights, and constrained time for corrective measures. In this phase, pilots must oversee intricate activities including preparing the aircraft for landing, adhering to air traffic control directives, and adjusting for environmental disruptions such as wind shear or turbulence. These situations not only reduce the margin for recovery from deviations but also elevate the probability of experiencing aerodynamic stall, especially when coupled with latent system defects or delayed pilot reactions resulting in human error [2]. Nevertheless, according to Figure 1.2, it does not appear to be the most perilous period of flight operations for the probability of casualties.

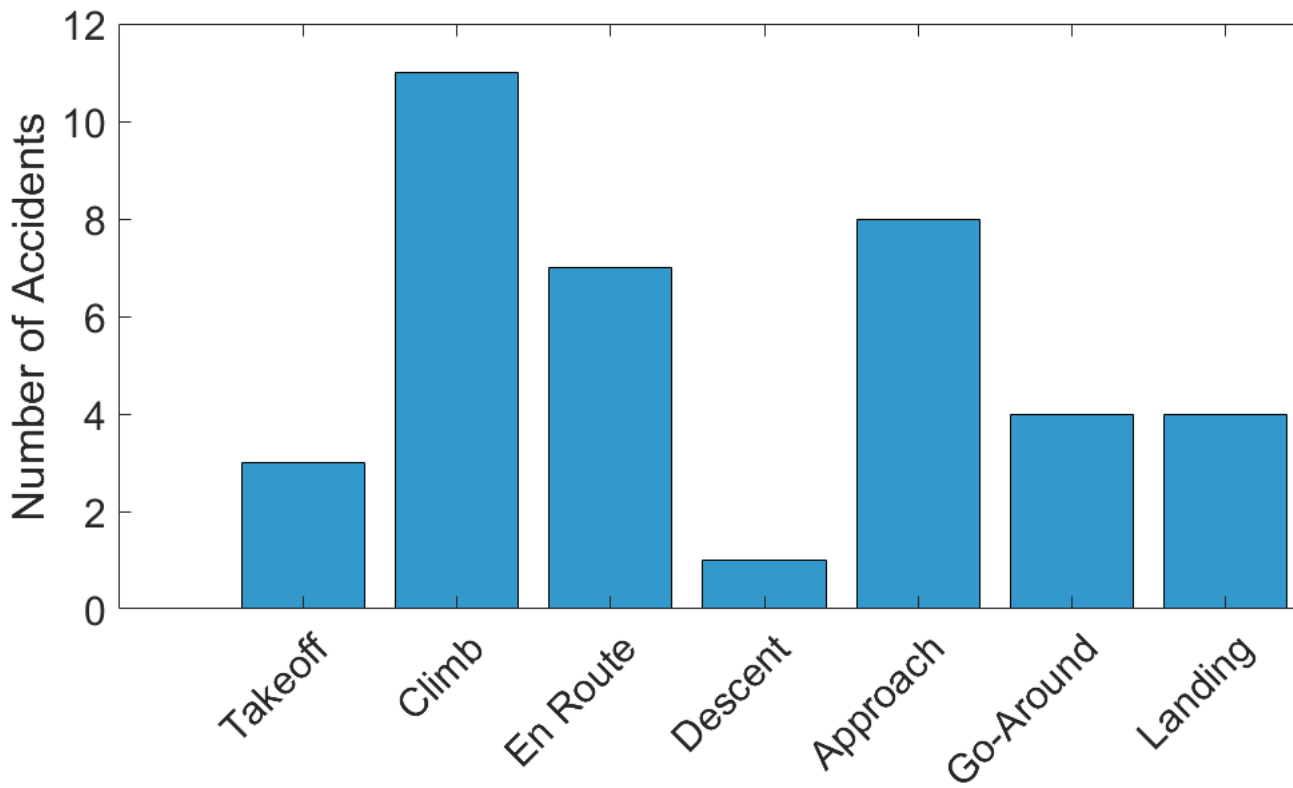


Figure 1.2 Breakdown of LOC-I Fatal Accidents by Phase of Flight from 2010-2014 (IATA)

The increasing accessibility of Flight Data Recorders (FDRs) via Quick Access Recorders (QARs) presents a substantial opportunity to assess aircraft performance during crucial flying phases. These "black boxes" record comprehensive in-flight data, encompassing metrics such as altitude, airspeed, engine performance, and control inputs.<sup>[12]</sup> NASA and several academic institutions frequently utilize these statistics to analyze aircraft performance during flight [3]. To distinguish between the two, FDRs are certified devices required for accident investigations, capturing a limited set of critical flight parameters with high reliability. In contrast, QARs are generally non-certified and utilized for routine monitoring or operational analysis, often recording a wider array of data but with less rigorous standards.

Relatively new in the world of research, subset simulation [4] is a technique in stochastic process analysis that efficiently estimates the likelihood of infrequent events. This method considerably decreases processing expenses by decomposing the rare-event probability into a product of conditional probabilities, while preserving robustness in high-dimensional scenarios. Focusing iteratively on crucial portions of the sample space, in contrast to Monte Carlo simulations, this is especially advantageous for rare events such as LOC-I during the approach, where observational data is limited due to the infrequency of flight operations.

Utilizing QAR data facilitates a high-resolution, parameter-dense dataset that encapsulates diverse flight dynamics and control inputs [5]. These datasets are crucial for enhancing model precision and corroborating predictions with real-world situations. This research employs subset simulation to establish a rigorous methodology for calculating stall and LOC-I likelihood during a critical flight phase, thereby addressing a gap in aviation safety research and aligning with current initiatives to enhance predictive safety measures. It contributes to an expanding corpus of research centered on proactive risk assessment and reduction, rather than exclusively on post-incident analysis.

## Key Issues

The key issues brought up for this study, given the project's background, are as follows:

1. How can a total energy-based model accurately represent the dynamics of an aircraft during the landing approach, and which flight parameters influence its energy state?
2. What threshold circumstances delineate a loss of control or aerodynamic stall event during the approach phase, and how can these infrequent occurrences be accurately simulated utilizing stochastic techniques such as subset simulation?
3. Which flight factors most significantly influence the probability of loss of control, and how may their relative effects be systematically evaluated and prioritized?

## Objectives

The objectives of this study, based on the key issues, are as follows:

1. Develop a flight dynamics model based on total energy that elucidates the correlation between essential flight parameters and the aircraft's mechanical energy state during the landing approach phase, serving as the basis for future risk assessment.
2. Choose suitable thresholds for LOC-I and aerodynamic stall; and establish a subset simulation framework to assess the likelihood of accessing the specified failure zone amid operational and environmental uncertainty.
3. Evaluate and rank the elements contributing to the incident by analyzing their relative impact on failure likelihood, therefore determining the most crucial parameters influencing approach stability.

## Scope

This research is confined to these limitations:

1. The study explicitly examines the danger of aerodynamic stall and loss of control during the landing approach phase, where both events are very critical. Other flight phases, including take-off and cruise, are not extensively examined.
2. The research predominantly uses only a stochastic process technique known as subset simulation to estimate risk and therefore prioritizes probabilistic methods over deterministic ones.
3. The model lacks a full flight dynamics modeling, as it solely accounts for steady-state motion during landing, neglecting dynamic maneuvers or transient behaviors, hence rendering it inadequate for examining quick control inputs and pilot-induced oscillations for example.

## Methodology

This research assesses the risk of LOC-I resulting from aerodynamic stall during a Boeing 747 landing approach, employing stochastic processes, particularly subset simulation with Markov Chain Monte Carlo (MCMC) sampling. Flight data from QAR systems is pre-processed by detecting and correcting outliers, and a flight dynamics model is constructed to mimic the aircraft's performance under similar conditions during approach. The model assists in identifying crucial flight circumstances, such as a high angle of attack or insufficient airspeed, that may result in a stall or LOC-I. Figure 1.3 provides a comprehensive summary of the research methodology for this project.

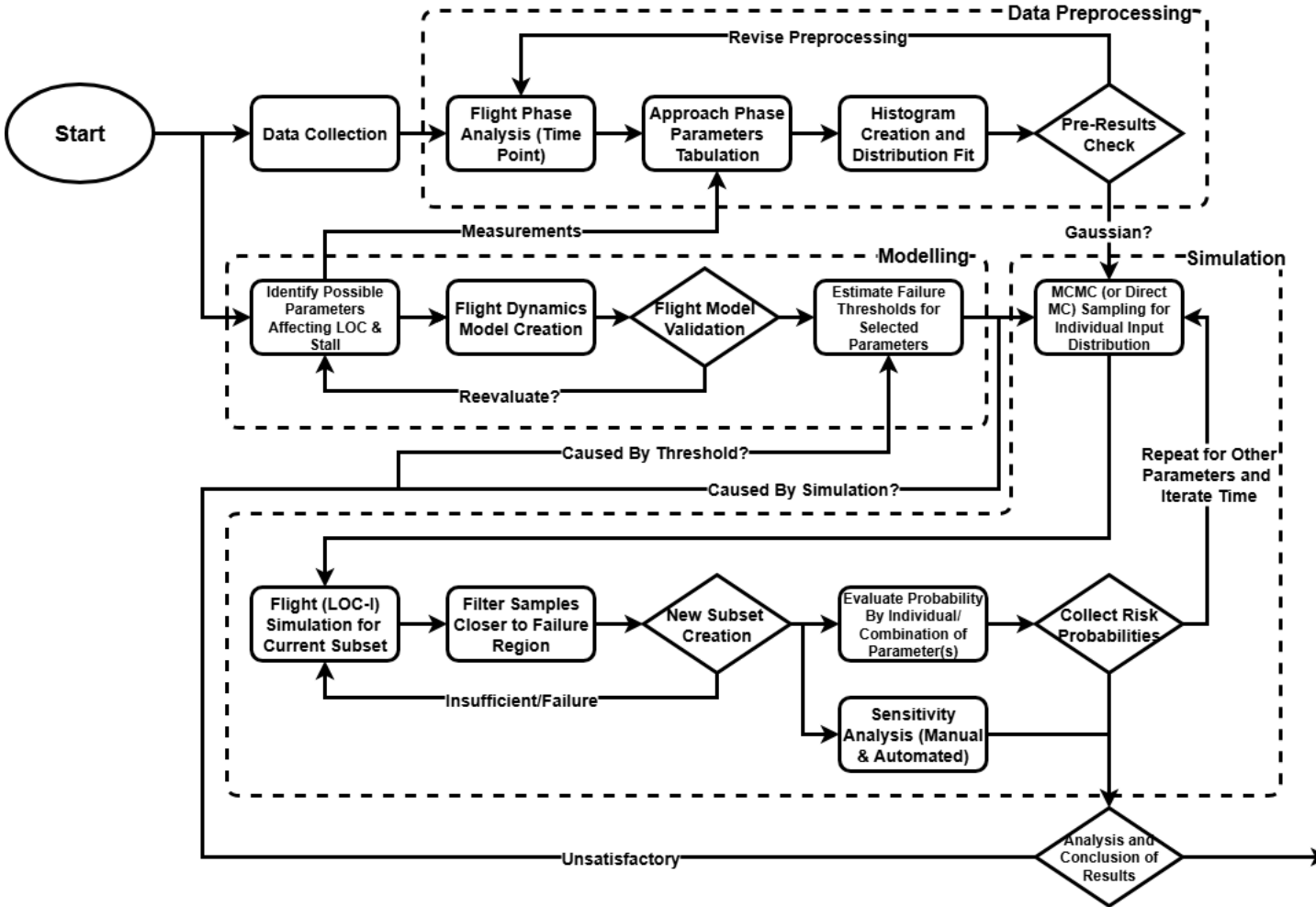


Figure 1.3 Research Flowchart

## Structure Overview

This paper comprises seven principal chapters, each contributing to a thorough examination of the probabilistic modeling of LOC-I and aerodynamic stall during the landing approach of a commercial transport aircraft. The following is a concise summary of each chapter:

**Chapter 1** delineates the research's background, purpose, and principal issues concerning the measurement of aviation risk, while also outlining the objectives, scope, methodology, and overall structure of the paper.

**Chapter 2** examines aerodynamic stall and its influence on LOC-I incidents, instrument approach protocols for transport aircraft, and critical mathematical methodologies including probability theory, stochastic processes, Markov chains, MCMC techniques, and subset simulation approaches. It evaluates multiple research works on aviation risk assessment and suggests a framework to bridge the existing research gap.

**Chapter 3** presents the flight data utilized in this analysis along with the preprocessing procedures. The work centers on producing several probability distributions for a critical flight parameter associated with stall and LOC-I during the approach. These initial findings offer insights into the parameter's fluctuation and establish a foundation for future risk estimation through stochastic approaches.

**Chapter 4** breaks down a modeling and simulation methodology for assessing the likelihood of LOC-I during approach. The process commences with a model that incorporates flight factors into a comprehensive energy rate equation, which is then assessed against a mechanical total energy formulation. Both models are simulated utilizing flight data, and consistency verifications are conducted. Defined criteria for specific LOC-I are established, and subset simulation is utilized to calculate the probability of the failure domain.

**Chapter 5** establishes the comprehensive and augmented results derived from the subset simulation, emphasizing the diverse probability estimations of LOC-I incidents during the landing approach. It examines critical flying characteristics and assesses how their fluctuations affect the overall risk profile. This chapter also examines the importance of certain threshold criteria and emphasizes significant themes identified across various flying circumstances.

**Chapter 6** closes this document by encapsulating the principal findings of the modeling and analysis stages. The text evaluates the efficacy of the implemented stochastic framework in measuring rare event probabilities and examines the implications of the results for aviation safety. Recommendations for enhancing safety conditions are presented, along with proposals for future research.

## Chapter 2

### Basic Theory and Literature Study

#### 2.1 Theoretical Basis

This section examines aerodynamic stall and LOC-I in aviation safety, with an additional delve into probability theory and instrument approach techniques. Fundamental procedures such as stochastic processes, Markov Chain Monte Carlo methods, and subset simulation are presented, for an in-depth comprehension of rare event probabilities.

##### 2.1.1 Aerodynamic Stall and Loss of Control (LOC)

Aerodynamic stall occurs when an airfoil experiences flow separation at high angles of attack, causing a significant reduction in lift and increased drag [6]. At low to moderate angles, the lift coefficient ( $c_l$ ) increases linearly with the angle of attack ( $\alpha$ ), indicating a smooth, attached flow. As  $\alpha$  increases, the flow detaches from the upper surface, causing stagnant air and reversed flow. The maximum lift coefficient ( $c_{l,max}$ ) is crucial for determining an aircraft's stalling speed, with higher values indicating increased stalling speeds. This is clearly illustrated in Figure 2.1, which depicts the evolution or onset of aerodynamic stall.

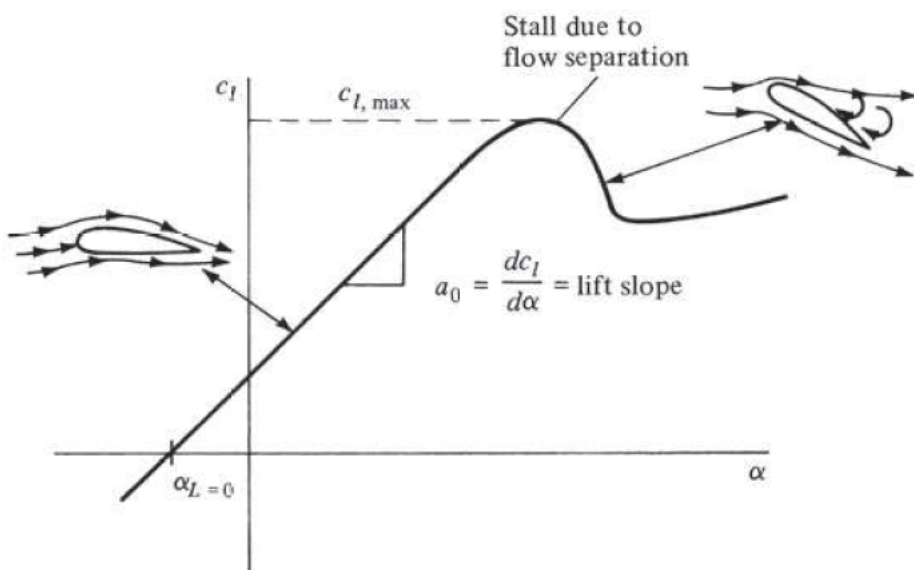


Figure 2.1  $C_l$ - $\alpha$  Curve for Cambered Airfoil (Anderson, 2024)

In-flight loss of control (LOC-I) in aircraft is a significant contributor to fatal accidents globally, arising from multiple dangers and precursors. These accidents are intricate and necessitate various intervention tactics, rendering any one approach ineffective. It is closely linked to aerodynamic stalls, as an individual factor in vehicle upsets [7], which can trigger during key flight phases like take-off, landing, or vigorous maneuvers.

This phenomenon occurs when the pilot loses control of the <sup>(26)</sup> aircraft's attitude, leading to <sup>(26)</sup> uncontrollable descent or spin [7]. Factors contributing to LOC-I include pilot error, environmental factors like turbulence or wind shear, and technical malfunctions like faulty sensors or systems causing erroneous control inputs. Therefore, LOC-I continues to be a central concern in worldwide aviation safety initiatives, as mitigating such incidents requires a comprehensive approach involving sophisticated modeling, pilot education, and data-informed risk evaluation.

### 2.1.2 Instrument Approach Procedure for Transport Aircraft

An instrument approach procedure (IAP) [8] comprises a series of predefined maneuvers employed to guide an aircraft under IFR from the initial approach segment to landing or a designated visual landing location. The ICAO defines it as a sequence of maneuvers reliant on flying instruments, ensuring specified obstacle protection from the initial approach fix (IAF) to the landing runway. Figure 2.2 illustrates how the FAA categorizes this specific period of flight according to the beacons encountered and the altitude of the approaching aircraft.

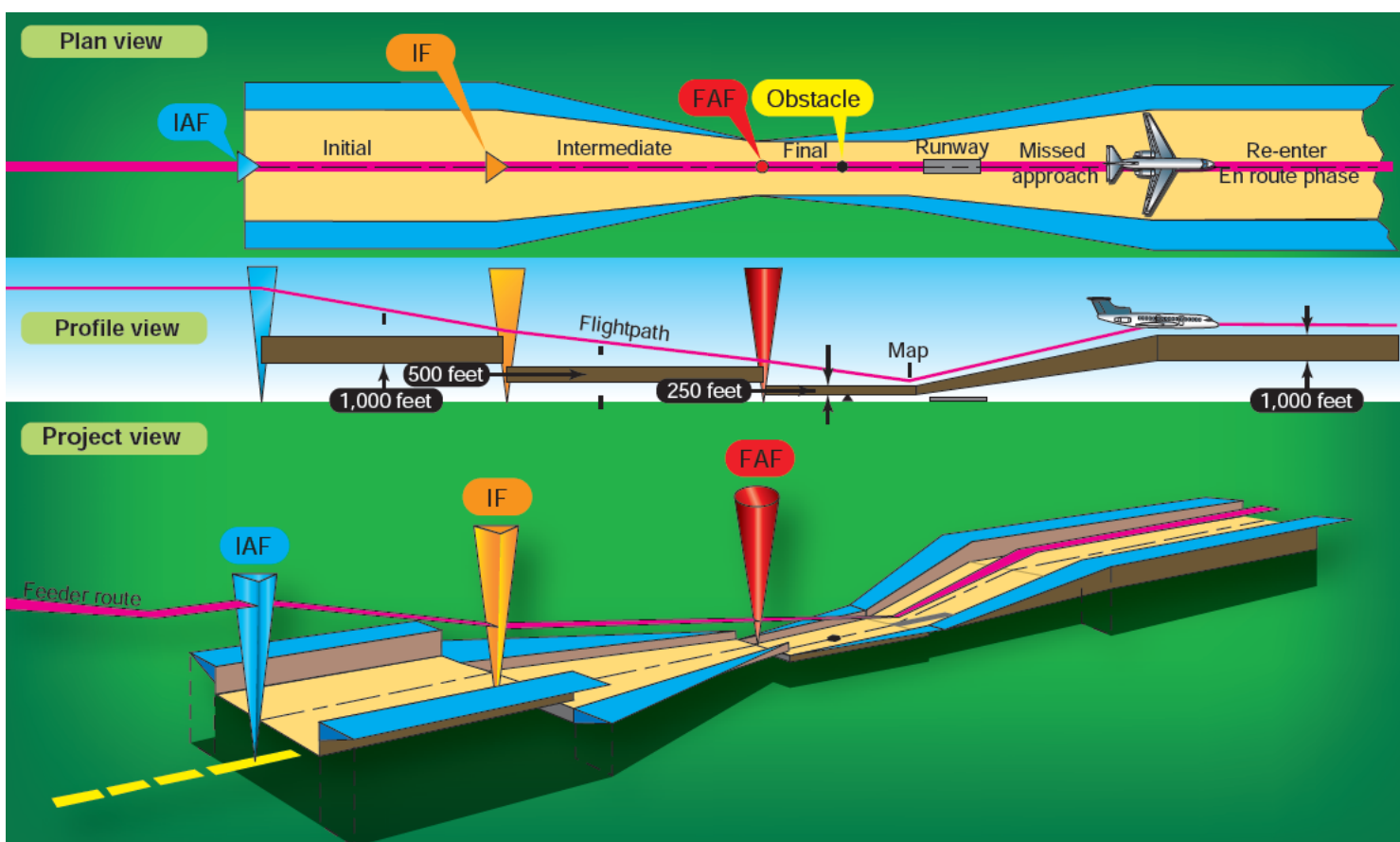


Figure 2.2 Approach Segments and Obstacle Clearance (FAA)

An IAP comprises of five segments [8]:

- Feeder routes that guide aircraft from en route to the IAF.
- The initial approach segment aligns aircraft with intermediate (IF) or final approach segments (FAF).<sup>(27)</sup>
- The <sup>(17)</sup> intermediate approach segment<sup>(17)</sup> aligns aircraft for the <sup>(17)</sup> final descent to the <sup>(17)</sup> runway.
- The <sup>(19)</sup> final approach segment begins at <sup>(19)</sup> the <sup>(19)</sup> glideslope-intercept altitude<sup>(19)</sup> plane intersection.
- The missed approach segment starts at the <sup>(9)</sup> Minimum Approach Point (MAP) and ends at a <sup>(9)</sup> designated <sup>(9)</sup> hold point.

When <sup>(15)</sup> utilizing radar control, air traffic control (ATC) may <sup>(15)</sup> substitute part or all <sup>(15)</sup> of these phases <sup>(15)</sup> with radar <sup>(15)</sup> vectors, offering navigational <sup>(15)</sup> assistance to aircraft <sup>(15)</sup> through specified headings derived from radar data. It enables them to manage airspace with greater flexibility by guiding aircraft along optimized routes that may substantially diverge from established procedures, especially during high traffic density or when addressing dynamic operational requirements such as weather deviations or sequencing limitations. In some cases, radar vectors may replace entire segments of standard terminal arrival routes (STARs) or standard instrument departures (SIDs), allowing controllers to shorten track miles or establish more efficient sequencing for arrivals.

The Instrument Landing System (ILS) [8] is a precise approach method capable of facilitating 29 arrivals per hour on a runway. It offers lateral and vertical guidance to aircraft during the final approach phase, facilitating safe landings in low-visibility conditions, including fog, heavy rain, or nighttime operations. The systems can then be enhanced with parallel, simultaneous parallel, accurate runway monitoring, and/or converging approaches, all aimed at optimizing runway utilization and sustaining high traffic flow while assuring safety. These enhancements facilitate synchronized landings on closely situated runways or within intricate airport configurations, reducing delays and improving airspace efficiency. The approaches are categorized into three classifications (CAT I, CAT II, and CAT III), each requiring additional certification for both the aircraft and the flying crew. Additional ground-based NAVAIDs that can assist the ILS comprise a localizer, localizer/DME, localizer back course, and a localizer-type directional aid (LDA) [8]. When an ILS is utilized, a back course may be accessible alongside the localizer.

With regards to the flight data (as seen in Chapter 3), the ILS/LOC approach for Runway 30R at Minneapolis–Saint Paul International Airport (ICAO: KMSP) exemplifies the instrument approach methods previously addressed. The accompanying Figure 2.3 illustrates the glide slope and descent profile, depicting the anticipated trajectory and altitude adjustments an aircraft should adhere to during the approach. During an ILS approach, the glide slope and localizer signals direct the airplane along an exact descent trajectory, facilitating a controlled and steady approach under low-visibility situations.

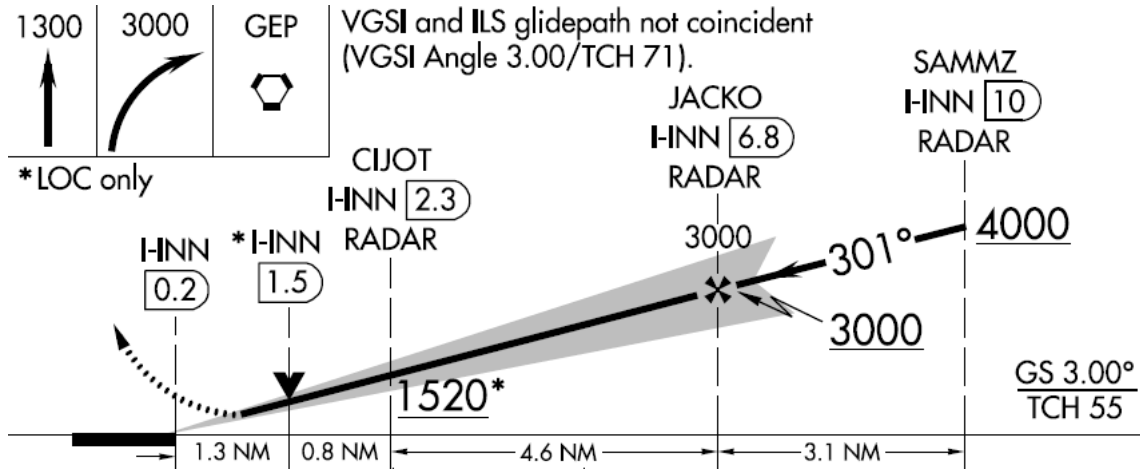


Figure 2.3 KMSP Runway 30R ILS/LOC Approach Guide (FAA)

### 2.1.3 Probability Theory for Continuous Random Variables

Conducting experiments tends to frequently emphasize the aggregate of outcomes rather than the specific outcome itself. These quantities of interest, referred to as random variables, are defined within the sample space. The value of a random variable is dictated by the outcome of the experiment, allowing us to assign probabilities to potential values.

For a pair of random variables  $X$  and  $Y$  [9], the joint cumulative probability distribution function  $F_{XY}$  of  $X$  and  $Y$  is given by

(2.1)

The distributions of  $X$  or  $Y$  can be derived from the joint distribution as follows:

(2.2)

(2.3)

$X$  and  $Y$  are considered jointly continuous if there exists a function  $p(x, y)$ , called the joint probability density function which is defined for all real  $x$  and  $y$ , such that for all sets  $A$  and  $B$  of real numbers as,

(2.4)

Consequently, the probability density of  $X$  or  $Y$  may be derived from the function  $p(x, y)$ , yielding the following result.

(2.5)

(2.6)

The expected value (or mean  $\mu$ ) of  $g$ , if it is a function of  $X$  and  $Y$  as continuous random variables, is provided by

(2.7)

Covariance between two random variables  $X$  and  $Y$ , where  $\sigma$  is the standard deviation, is then defined as

(2.8)

It is important to note that if the random variables  $X$  and  $Y$  are considered independent, the preceding statements are defined as follows

(2.9)

(2.10)

(2.11)

The conditional distribution function  $F_{X|Y}(a|b)$  of event  $X$  given event  $Y = y$ , if  $Pr(Y = y) > 0$ , is defined by

(2.12)

Thus, when  $y = \infty$ , it yields the law of total probability, wherein

(2.13)

The expectation of conditional probability for  $g(X)$  given  $Y = y$  can then be articulated as

(2.14)

For a joint normal distribution of  $X$  and  $Y$ , the Pearson correlation coefficient  $\rho$ ,  $F_{XY}(a,b)$ , and covariance are computed as follows:

(2.15)

(2.16)

(2.17)

Likewise, the conditional distribution of  $X$  given  $Y = y$  yields another joint normal distribution expressed as

(2.18)

(2.19)

(2.20)

Failure is characterized by the surpassing of a response quantity  $Y$  beyond a threshold  $y$ .  $P(F)$  can then be interpreted as the value of the "complementary cumulative distribution function" (CCDF) of  $Y$  at  $y$ . This distribution is also referred to as the tail distribution and is described as

(2.21)

Conversely, for a specified probability level  $p$ , the "upper quantile" is defined as the value  $y_p$  such that  $P(Y > y_p) = p$ . [10] In Direct Monte Carlo, this can be estimated by  $Y_{[(1-p)N]}$ , under the assumption that  $pN$  is an integer. The order statistics  $\{Y_{[k]} : k = 1, \dots, N\}$  serve as an estimator for  $y_{pk}$  for a fixed value of  $p_k$ .

(2.22)

Plotting the pairs  $(Y_{[k]}, p_k)$  provides an estimate of the CCDF and it is a right-continuous function and should be represented in a "staircase" format as illustrated in Figure 2.4. This stepwise depiction precisely illustrates the discrete character of the empirical distribution obtained from the sample. Nonetheless, when the sample size  $N$  is substantial, the intervals become sufficiently narrow enough that the discrete transitions are visually insignificant, allowing a piecewise line linking the data points to function as an effective approximation.

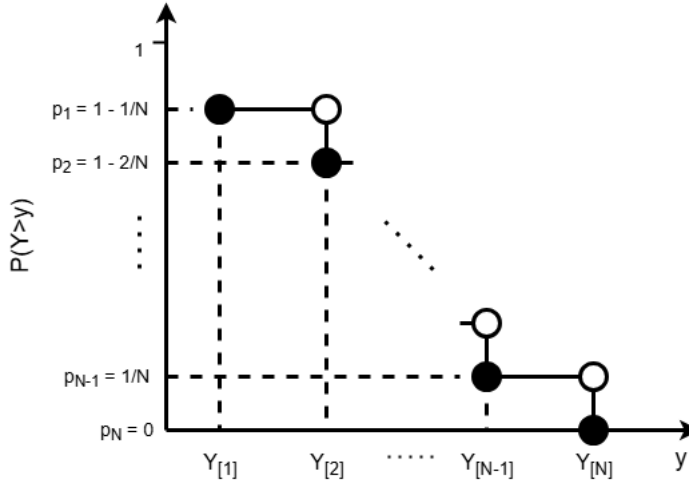


Figure 2.4 CCDF Plot Construction

#### 2.1.4 Stochastic Processes and Markov Chains

A stochastic process [9]  $\{X(t), t \in t\}$  is a set of random variables, with  $X(t)$  denoting the state of the process at time  $t$ . The index set of the process is  $T$ , which may be either a countable set or an interval on the real line. A discrete-time process is indexed by nonnegative integers  $\{X_n, n = 0, 1, \dots\}$ , whereas a continuous-time process is indexed by nonnegative real numbers  $\{X_t, t \geq 0\}$ . The state space,  $S$ , of a stochastic process comprises the complete set of potential values that the random variables may take on.

Therefore, a stochastic process [11] is distinguished by its relationships among random variables, specified by the joint distribution function of every finite family of variables. A well-defined stochastic process is considered complete once its state space, index parameter, and family of joint distributions are prescribed. Several inequalities are pivotal in the analytical examination of stochastic processes, notably the Chebyshev inequality and the Schwarz inequality.

A Markov process [11] is then a system in which the likelihood of a specific future behavior is independent of prior information regarding the system's current state. Nonetheless, if the present condition is inaccurate, the likelihood of subsequent action may be modified. Whenever  $t_1 < t_2 < \dots < t_n < t$ , a process is said to be Markov if

(2.23)

A Markov chain [11] is thus a Markov process characterized by a finite or countably infinite state space. It is characterized by a countable or finite set  $T = \{0, 1, 2, \dots\}$ , where the value of  $X_n$  is the result of the  $n$ th trial. The state space is often denoted by nonnegative integers, and  $X_n$  is regarded as being in state  $i$  if  $X_n = i$ . The probability of  $X_{n+1}$  being in state  $j$ , given  $X_n$  being in state  $i$ , is represented by

(2.24)

The transition probabilities [11] presented above depend on the initial and final states, the duration of the transition, and the time variable  $n$ . A stationary transition probability, independent of time variables, is represented as  $P_{ij}$ , indicating the probability of a state change from  $i$  to  $j$  in a single trial. It is common to organize these as a matrix, specifically an infinite square array (Markov transition matrix) as

(2.25)

The  $(i+1)$ -th row of  $P$  denotes the probability distribution of  $X_{n+1}$  values given  $X_n = i$ , constituting a finite square matrix whose order corresponds to the number of states and  $P_{ij}$  satisfies the conditions as

(2.26)

#### 2.1.4 Markov Chain Monte Carlo (MCMC)

For a vector of model parameters [12],  $\theta$ , where  $\theta = [\theta_1, \theta_2, \dots]$ ,  $P(\theta)$  represents its distribution before the observation of specific random variable values within the model. Let  $D$  represent the data to be observed, and  $P(D|\theta)$  signify the probability of observing the data and

(2.27)

The posterior distribution, representing the conditional probability of  $\theta$  given the observed data, is derived using Bayes' theorem as

(2.28)

Additionally, the posterior marginal expectation  $\mu_h$  can be estimated using unbiased for a known function  $h(\theta)$  by simulating identically distributed variables  $\theta$ , from  $P(\theta|D)$ , where

(2.29)

(2.30)

Therefore, given that the random variables  $\theta$ , are likely dependent, the variance of this estimator is defined as

(2.31)

An example, called the Metropolis-Hastings algorithm [12], is a prominent simulation technique utilizing MCMC, which enhances computational efficiency by producing a series of random samples converging towards the expectation, also known as a Markov chain. This sequence is generated by suggesting new samples derived from prior samples and subsequently accepting or rejecting them according to their probability distribution at that point. Its acceptance criterion  $\alpha$  is determined by a probability ratio, facilitating more frequent exploration of areas with higher probability density but permitting infrequent transitions into lower-probability regions to prevent local convergence.

This algorithm defines the prior distribution with  $f(x)$ , where  $x' = [x_1, x_2, \dots]$ , a function proportional to the target probability density function  $P(x)$ . Subsequently, the sequence of random vectors is produced from a homogeneous discrete-time Markov chain, characterized by its transition kernel between states and its density function as

(2.32)

(2.33)

If the Markov chain is selected to be ergodic [12], it possesses a unique stationary probability density  $\pi$  for  $P(x)$ . Consequently, after an appropriate burn-in period ( $m$  stages, for instance, of the chain), the random vectors  $X_t$  exhibit a marginal distribution  $P$  that is nearly  $\pi$ . The expectation and its estimator can then be delineated as

(2.34)

(2.35)

When  $X_t = x$ , the subsequent state,  $X_{t+1}$ , may either transition to  $y$  with probability  $a(x,y)$  or persist as  $x$  with probability  $1 - a(x,y)$ . In this context,  $y$  represents a candidate point derived from a proposed density function  $q(y|x)$ . Consequently,  $a(x,y)$ , often referred to as the acceptance probability, is equivalent to

(2.36)

(2.37)

The original Metropolis algorithm [12] assumes symmetry in  $q$ , such that  $q(x|y) = q(y|x)$ , which simplifies the acceptance probability to the minimum of either 1 or the ratio of prior distributions. This chain is time-reversible in equilibrium, indicating that  $f$  constitutes a stationary distribution of the Markov chain, signifying that

(2.38)

To determine  $\mu_h$ , the Markov chain is reproduced  $K$  times, with widely varied initial values. With  $X_{ti}$  representing the  $i$ -th equilibrium observation (after burn-in) for the  $i$ -th replication, the unbiased estimator and its standard error are equal to

(2.39)

(2.40)

Evaluating the moment a realization has burned in is difficult, particularly in high-dimensional state systems. Potential approaches involve graphing the sequence components or functions of  $X_t$  and assessing the number of equilibrium observations in each realization. Visual examination of trace plots can also indicate if the chain has stabilized, while statistical diagnostics like the Gelman-Rubin statistic or autocorrelation analysis can be utilized for a more objective assessment of convergence.

## 2.1.6 Subset Simulation

Subset Simulation [10] employs conditional probability, wherein the likelihood of a rare event is determined by the probability of its occurrence given a more frequent event, multiplied by the probability of that more frequent event. For a failure threshold  $b$  and intermediates  $m$ ,

(2.41)

Initially, the algorithm first selects the "level probability"  $p_0 \in (0, 1)$  and the "number of samples per level"  $N$  where then,

(number of chains) (2.42)

(number of samples per chain) (2.43)

(2.44)

The procedure then commences with Direct Monte Carlo, wherein samples are created directly by the parameter PDF, devoid of any conditioning. This phase aims to deliver dependable information at the probability level ranging from 1 to  $p_0$ , instead of the target level  $p_0^m$ . By functioning inside this high-probability domain, the method guarantees a sufficiently substantial quantity of useful samples, which would otherwise be infrequent and computationally costly to acquire by conventional Monte Carlo methods. Thus, the CCDF curve within the range from probability 1 to  $p_0$  can be precisely depicted and utilized to establish an intermediate performance criterion.

The threshold level  $b_i$  is established from the samples produced at  $(i-1)$ . The samples of  $X$ , conditioned on  $F_i = \{Y > b_i\}$ , are dispersed according to the parameter PDF. These samples serve as "seeds" for creating samples conditioned on  $F_i$  through MCMC, enabling the procedure to effectively investigate the tail region linked to the uncommon event. Significantly, as each Markov chain commences from a sample that inherently meets the criterion  $Y > b_i$ , the resultant chains are stationary from the outset. This attribute effectively obviates the necessity for a burn-in time, therefore circumventing the uncertainty and data loss linked to the rejection of first, non-converged samples.

The conventional approach [10] for subset simulation seeks uniform conditional probabilities and consistent sample size for each simulation level to achieve a balance of simplicity, robustness, and performance. Nonetheless, varying probabilities and samples may be utilized at distinct levels, primarily contingent upon the connection among MCMC samples, which is not predetermined. Also, the selection of intermediate threshold levels  $m$  influences the variance of conditional probability estimators [10]. An astute decision must balance minimal conditional failure probability with a substantial number of levels to achieve the goal failure event.

## 2.2 Literature Review

This literature review section examines statistical methodologies for assessing transportation hazards in aviation, namely Monte Carlo, MCMC, and subset simulation, with an emphasis on their efficacy in modeling and forecasting risks associated with aircraft operations.

### 2.3.1 Monte Carlo Methods in Risk Assessment

Here manifests the application of Monte Carlo methods in risk assessment, with an emphasis on their use in aviation. Monte Carlo simulations are employed to simulate and assess uncertain systems, collision hazards, and anomalous crash statistics. The use of these techniques in marine shipping is also highlighted in this section, illustrating their wider applicability for risk assessment in other modes of transportation.

1. A paper [13] from the University of Southampton recommends measuring collision risks in uncrewed aircraft systems to enhance safety and efficiency in the utilization of shared airspace. It utilizes network traffic statistics to evaluate hazards faced by General Aviation aircraft in uncontrolled airspace. The Monte Carlo method probabilistically samples traffic positions, resulting in a convergent probability while maintaining computational efficiency.
2. A study [14] from the Nanjing University of Aeronautics and Astronautics presents a risk assessment methodology for aero-engine operational phases based on Monte Carlo simulation. The methodology employs historical failure data from 1,600 aero-engines to assess risk utilizing the Weibull distribution. It delineates three failure modes and hazard levels, proposing solutions to rectify the issues.
3. A research project [15] from California State University, Stanislaus aims to predict crash frequency over five years using data from the Aviation Safety Net Database. The Monte Carlo approach simulates uncertain outcomes using random sampling and the cumulative distribution function. Results show the Boeing 737-MAX's casualty figures having a significant deviation beyond the expected upper threshold, requiring further investigation.
4. A study [16] from the Gdynia Maritime University employs a Monte Carlo simulation model for the analysis of marine transport risks, emphasizing shipping accidents and their environmental repercussions. It utilizes historical data from 1,630 maritime casualty reports and creates a C# software for simulation tasks. Results indicate a reduction in relative errors and enhanced robustness over 25 years of incidents.

### 2.3.2 MCMC Methods in Risk Assessment

Next, the application of Markov Chain Monte Carlo (MCMC) techniques in risk assessment is examined. Research indicates that MCMC approaches in aviation enhance model dependencies and state transitions, which are essential in dynamic systems such as aviation operations. Furthermore, another marine shipping case study illustrates the method's adaptability and efficacy in other transportation industries.

1. An article [17] from the University of Cambridge presents a Markov chain Monte Carlo framework for conflict resolution in air traffic management systems. It employs an air traffic simulator to replicate aircraft behavior, utilizing both realistic and stochastic models to account for wind disturbances. The methodology accurately predicts aircraft trajectories and mitigates clashes, although necessitates substantial processing power.
2. A study [18] from NASA's Langley Research Center employs ultrasonic inspection methods and finite element simulations to enhance the non-destructive evaluation of lightweight composite materials. It analyzes undamaged laminate plates utilizing laser Doppler vibrometer data and software to model wave propagation and delamination damage. A damage model is developed with a reversible jump MCMC methodology. This technique precisely measures delamination damage severity.
3. A study [19] from Shanghai Maritime University investigates the application of quantitative modeling and dynamic simulations to enhance the comprehension of maritime traffic risks and safety within the expanding water transportation sector. It examines 881 accidents from 2000 to 2006 utilizing a database and a stochastic generating methodology. The Markov Chain-Monte Carlo algorithm facilitates random sampling processes, ensuring data reliability with a Monte Carlo error of around 5%.

### 2.3.3 Subset Simulation in Risk Assessment

Hither examines the application of subset simulation in the assessment of rare events in aircraft operation. Subset simulation is a sophisticated method that effectively assesses the likelihood of unusual events, essential for aviation safety assessment. Most research employ this approach by deconstructing intricate dangers into manageable components, thus improving computing efficiency while maintaining accuracy.

1. A study [20] from the University of Massachusetts Lowell introduces a probabilistic methodology for the real-time risk evaluation of fatigue-critical aircraft components. It amalgamates health status data with physics-informed damage models, employing structural health monitoring devices and a Paris Law-derived crack growth model. Through enhanced Bayesian filtering, the findings revealed intermediate thresholds, demonstrating the efficacy of employing MCMC in conjunction with subset simulation.
2. A paper [21] from the University of Liverpool presents an effective approach for assessing the Probability of Conflict for Unmanned Aerial Systems in densely populated airspace, enhancing the efficacy of automated Sense-and-Avoid systems. The subset simulation method, concentrating on head-on and overtaking scenarios, surpasses direct Monte Carlo in estimating conflict probabilities; however, additional research is required for parameter optimization.
3. A study [22] from Technische Universität München investigates aerial refueling safety in civil aircraft, presenting a subset simulation method for effective safety evaluation. It assesses conventional position error estimating techniques and the algorithm of the simulation in moderate turbulence. The employed method demonstrated reliability, computational efficiency, and the capacity to appropriately evaluate aircraft excitation and reaction while mitigating uncertainties in aircraft dynamics.

## 2.3 Research Gap and Framework

Recent aviation risk assessment studies have predominantly concentrated on assessing hazards associated with mid-air collisions, composite material failures, and component failures. Nonetheless, there exists a deficiency in addressing aerodynamic stall and LOC-I during crucial flight phases, such as landing approaches, attributable to the intricate interplay of ambient factors, pilot maneuvers, and aircraft performance. The insufficient focus on these phenomena in predictive risk constitutes a significant research gap, especially in the development of probabilistic approaches that can accommodate the time-dependent, multi-variable characteristics of these crucial flight occurrences.

This thesis uses subset simulation to LOC-I risks during instrument approaches. It uses real-world flight data to model aircraft dynamics during descent and its associated risks, utilizing comprehensive flying parameters to establish a credible basis for simulation. The study examines stochastic processes and risk quantification, utilizing methods such as MCMC sampling and Subset Simulation to investigate the distribution tails where significant failures arise. This paper also seeks to avert LOC-I accidents and enhance aviation safety with quantitative tools to more effectively predict and manage these risks in operational settings.

## Chapter 3

### Data Gathering and Preprocessing

#### 3.1 Preprocessing Framework

This section delineates the preprocessing framework used to ready real-world flight data for risk assessment via subset simulation. This framework was developed to systematically extract, cleanse, and organize the complex and dense parameters recorded during aircraft approaches into a format appropriate for probabilistic analysis, specifically for distribution fitting to facilitate the subsequent simulation of input parameters.

##### 3.1.1 Raw Data Overview

This study analyzes a collection of 4,220 flight data sourced from the Quick Access Recorders (QARs) of Boeing 747 aircraft that arrived at Minneapolis-St. Paul International Airport (KMSP) and landed on runway 30R in January 2001. According to the runway map in Figure 3.1, Runway 30R is situated to the north of the airport and heads northeast, measuring approximately 2500 meters in length and 45.72 meters in width. During the data collection period, no substantial alterations in runway designation have been documented since (by magnetic drift for example), according to available FAA records of the airport in the past.

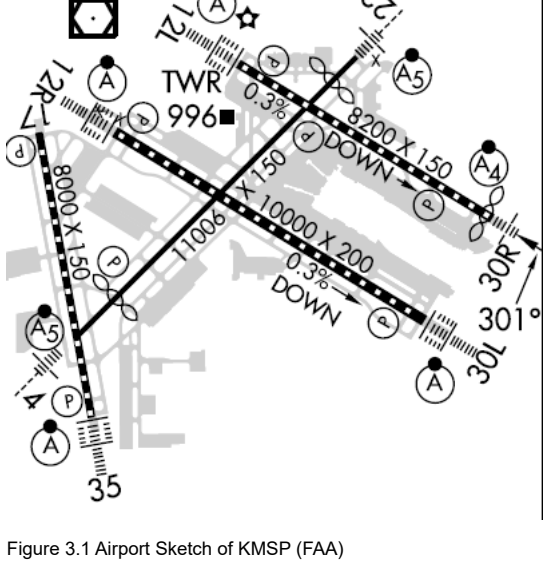


Figure 3.1 Airport Sketch of KMSP (FAA)

Each dataset comprises around 180 parameters documented during the flight, encompassing several facets of aircraft performance, environmental circumstances, and control inputs. The parameters encompass altitude, airspeed, angle of attack, engine thrust, control surface positions, and vertical acceleration, among others. The data is sourced from an online database, occupying 27.6 GB (compressed), with each flight represented as a .csv file containing between 50,000 and 150,000 rows and 180 columns, depending on the duration of the flight. From Figure 3.2, most flights originated from the central and eastern United States, with numerous departures from major metropolitan areas including Chicago, Atlanta, Dallas, and Washington, D.C. Significantly, there are several sources from the western and southern regions, along with a handful from Canada.

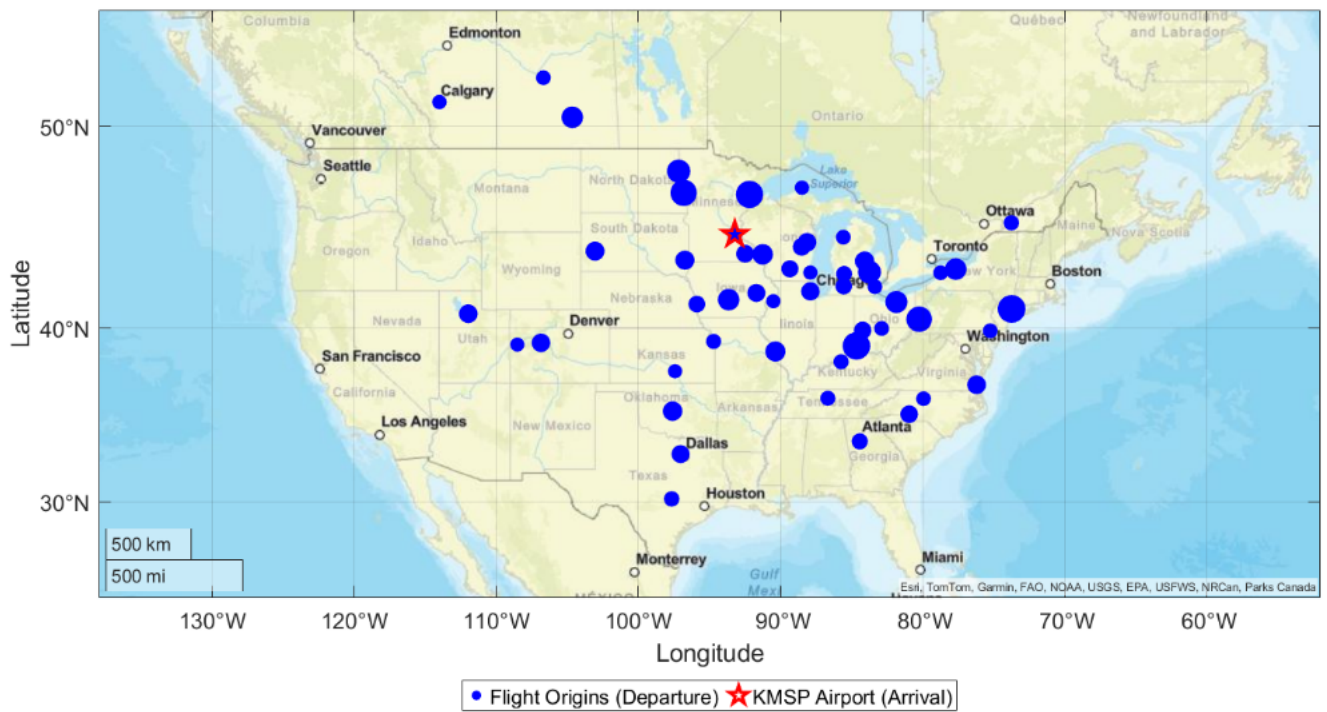


Figure 3.2 Origins of All Dataset Flights to KMSP

The data encompasses a variety of operational situations, including standard approaches and landings under differing weather and traffic conditions. Each trip's dataset includes high-resolution time-series recordings, sampled at regular intervals (for example 4, 8, or 16 Hz depending on the measuring equipment), providing a comprehensive depiction of dynamic changes during important flight stages and such a case (altitude) is shown on Figure 3.3.

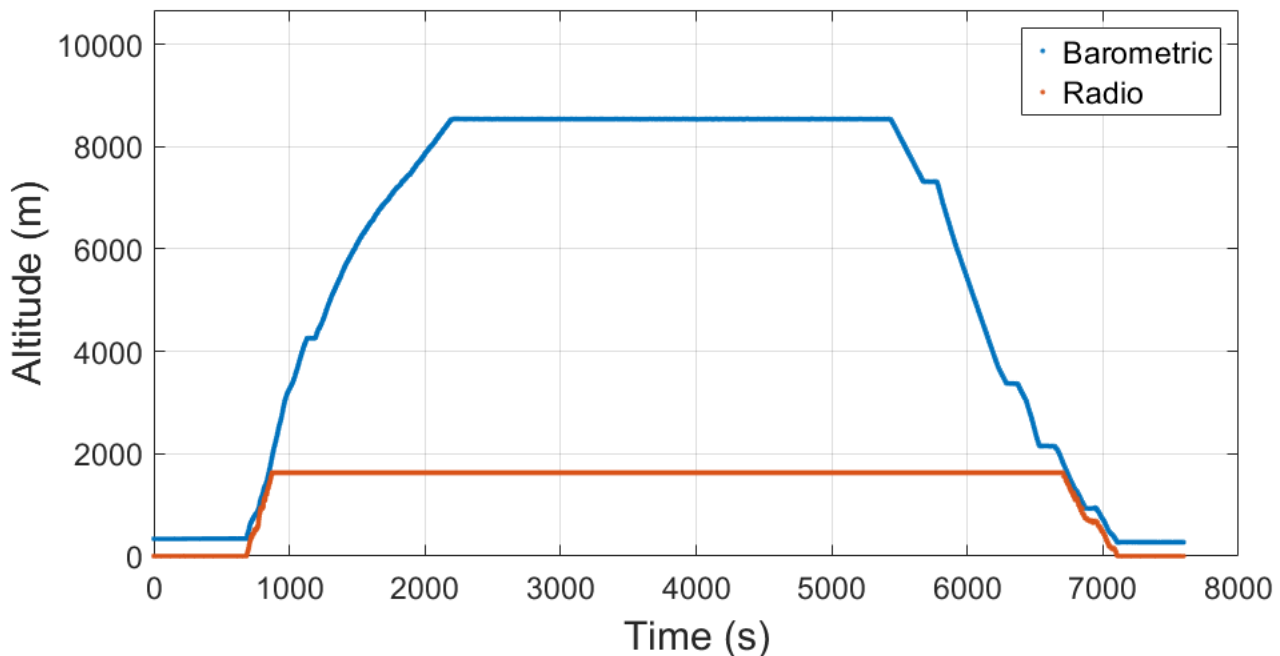


Figure 3.3 Typical Flight Profile from Flight Data

The raw data necessitated extensive preparation because of the intrinsic difficulties associated with real-world data. Challenges encompass absent values in specific parameters, measurement inaccuracies, and intermittent inconsistencies in temporal alignment among parameters. The difficulties within the data were either circumvented by omitting the problematic parameters or amended to guarantee the reliability of the following studies. Figure 3.4 illustrates an instance of this issue regarding N1 Command Thrust, resulting in the exclusion of this parameter from the research procedure.

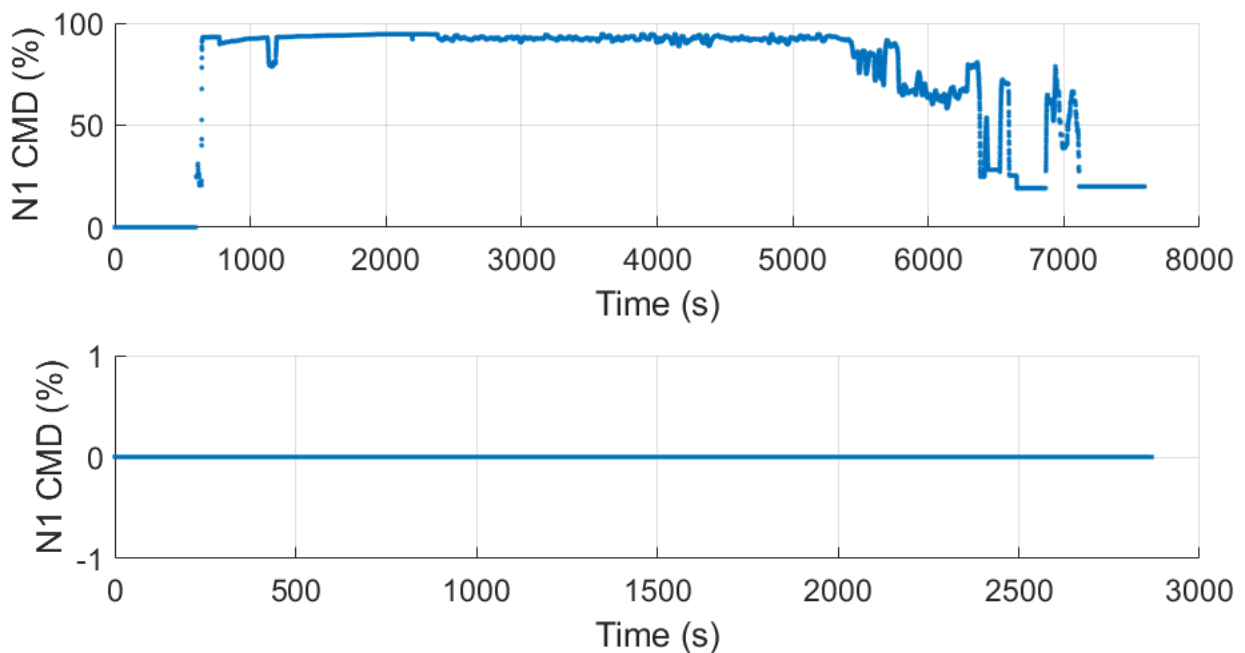


Figure 3.4 Data Plot Comparison (Typical vs. Problematic)

### 3.1.2 Preprocessing Steps

The raw flight data was systematically pre-processed to rectify discrepancies and ready for analysis. This phase was essential to guarantee the reliability of each candidate parameter for subsequent histogram plot development and distribution fitting. The preprocessing procedure comprised the subsequent essential steps:

#### 1. Identification of Candidate Parameters

Utilizing intuition and domain expertise, a collection of candidate characteristics (e.g., ground speed, pitch, roll) are selected to examine their significance concerning aerodynamic stall and LOC-I during the landing approach phase.

#### 1. Establishing Flight Phase Categories

Throughout a given flight, 8 essential flight phases, whose start are denoted as time points (TP1 to TP8), classify the distinct stages of flight from departure take-off to taxiing on arrival.

#### 1. Establishment of Criteria for Time Point Identification

Criteria for each time point (e.g., flap locations, altitude variations) were formulated, with particular emphasis on TP5 and TP6, which delineate the commencement of the final approach phase at two distinct heights.

#### 1. Execution and Verification of Algorithm

A MATLAB code was created to ascertain these time points across the entire flight. The algorithm was evaluated for resilience, guaranteeing uniform performance across flights with differing profiles and durations. Validation entailed constructing histograms of the time intervals between TP5, TP6, and TP7 (touchdown) to verify the consistency and range of the outcomes.

#### 1. Parameter Extraction at Approach Time Points

The algorithm extracted values of the candidate parameters for each flight at TP5 and TP6. These points were selected as they signify the commencement of the final approach phase, as it is the focus of this research.

#### 1. Data Compilation and Histogram Analysis

The extracted parameter values were organized into a table, while the eight selected time points for each flight were recorded as indices in a separate table. Histograms were subsequently created for each potential parameter and outliers were eliminated. Then, probability density function (PDF) curves were fitted to examine distributions that represent the initial distributions for future sampling.

### 3.1.3 MATLAB Algorithm

The preprocessing program uses MATLAB to optimize the extraction and organization of flight data from various datasets by recognizing critical flight phases and collecting pertinent parameter values, hence assuring consistency and scalability across numerous flight datasets through automation. The algorithm analyzes compressed data files (zipped .csv files) containing flight recorder information, pinpointing specific time points based on criteria such as flap positions and altitude thresholds, and extracting parameter values for subsequent analysis, ensuring robustness and accuracy despite variations in flight profiles and durations.

The complete code is provided in the Appendix (GitHub), with the workflow outlined as follows:

#### 1. Configuration and Initialization

The script initiates by clearing the workspace, establishing paths, and generating requisite folders. It initializes vacant arrays to retain extracted time points and histogram data.

#### 1. Parallel Computation

The script used a ‘parfor’ loop to concurrently process each aircraft. This guarantees the effective management of possibly thousands of files.

#### 1. Decompression and Verification of Flight Data

For each .zip file, it extracts the flight data into a temporary directory and thereafter verifies the existence of the anticipated .csv file; if absent, it omits processing for that specific file.

#### 1. Data Extraction and Analysis

The code identifies specific columns in each CSV file according to their parameter names (see Appendix). It initially computes crucial time points according to the conditions established for each phase. It then gathers essential parameter data at the designated time points to construct histograms later.

#### 1. Cleanup and Storage

Upon completion of file processing, the temporary directory is removed. Both categories of findings are kept in arrays, transformed into tables, and exported as .xlsx files.

Overall, the code was executed in the directory housing all 4220 compressed flight data, utilizing 4 of the 8 available 2.5 GHz cores of an Intel i5-10<sup>th</sup> generation CPU, resulting in a processing time of 14,278 seconds. Subsequently, an additional effort was undertaken to reduce the dataset size by exclusively utilizing the approach phase data through trimming (see to Section 4.2).

## 3.2 Categorization of Flight Phases (Time Points Identification)

The identification of time points (TPs) was predicated on defined criteria derived from the behavior of chosen aircraft variables that display consistent patterns during descent and landing. The selected parameters, including pitch angle thresholds, vertical speed, and radio altitude, align with specific changes in the aircraft's flight profile, such as flare onset and touchdown. The formal definitions of the eight selected TPs that span from the commencement of takeoff to the conclusion of landing, are delineated in Table 3.1, offering a systematic reference for the identification and use of each marker throughout the study.

Table 3.1 Definition of Time Points

### Time Point Definition

<b>TP1</b>	Start of Take-Off/End of Departure Taxi
<b>TP2</b>	Start of Climb/End of Take-Off
<b>TP3</b>	Start of Cruise/End of Climb
<b>TP4</b>	Start of Descent/End of Cruise
<b>TP5</b>	Start of Final Approach/End of Descent
<b>TP6</b>	Alternate Start of Final Approach/End of Descent
<b>TP7</b>	Start of Landing (Touchdown)/End of Final Approach
<b>TP8</b>	Start of Arrival Taxi/End of Landing

### 3.2.1 Criteria for Each Time Point

TP1, denoting the commencement of the take-off run, was determined by the location of the trailing edge flap. The condition was satisfied when the flap position initially surpassed 5° of its maximum deployment during the first half of the flight data. Figure 3.5 illustrates the standard trajectory and configuration of the flap position (in degrees) for most of the data.

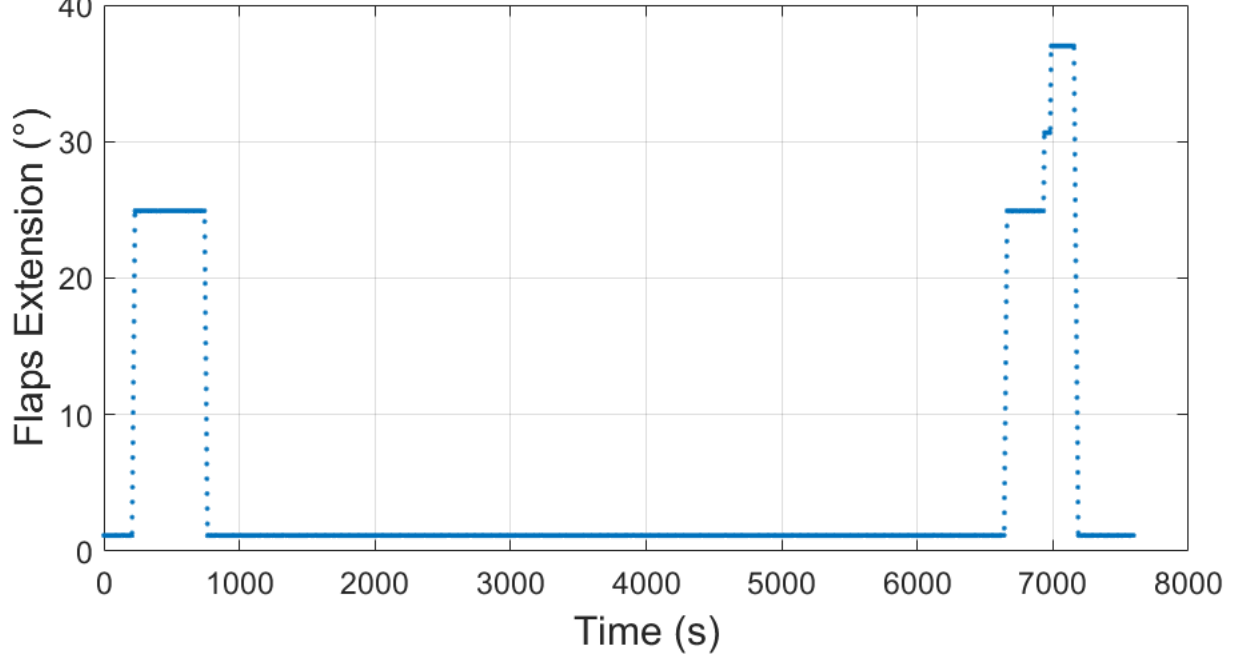


Figure 3.5 Typical Profile of Trailing Flap Position

After TP1, TP2, denoting the conclusion of the take-off roll and the commencement of the climb phase, was identified as the moment when the trailing edge flap position also fell below 5° during the first half of the flight data after TP1. TP3, denoting the apex of climb or the shift to the initial cruise, was determined by the flight phase parameter in the Aircraft Condition Monitoring System (ACMS) upon the value's change to 5 at some point after TP2. Correspondingly, TP4, signifying the commencement of descent, was situated in the latter half portion of the dataset when the flight phase shifted to 6 after TP3. Figure 3.6 illustrates the progression of the Flight ACMS value from 1 to 7 for the majority of the dataset.

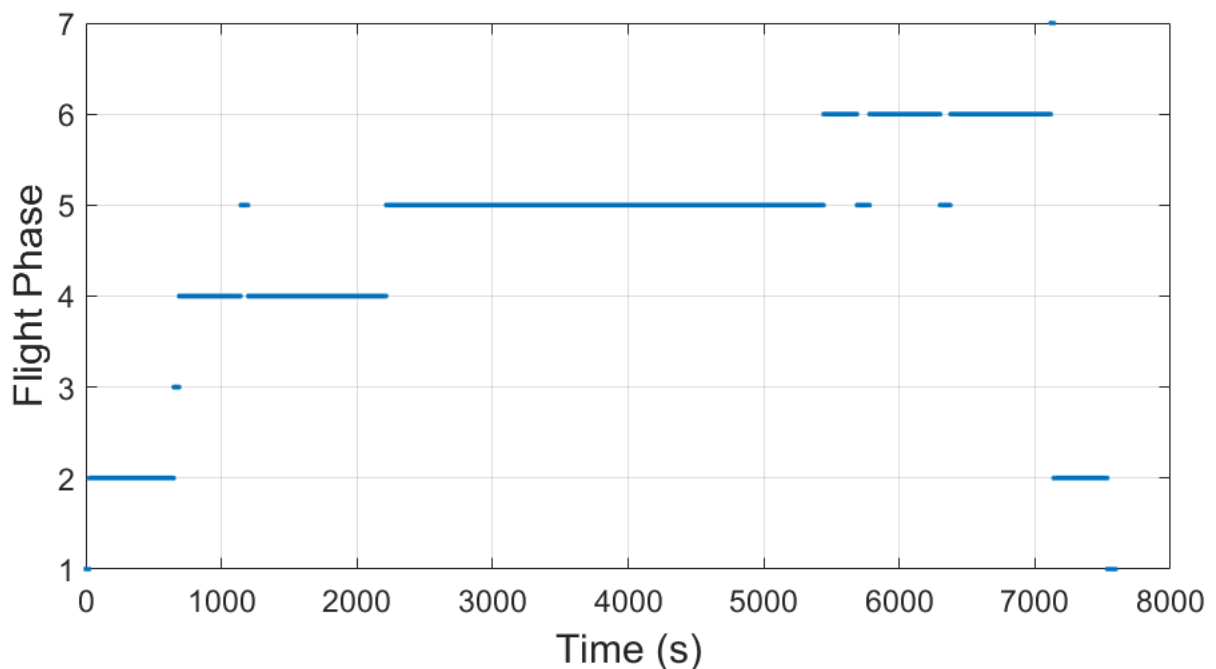


Figure 3.6 Typical Profile of Flight ACMS

Now while this parameter appears capable of addressing all necessary time points, its use diminishes when the aircraft is nearer to the ground, as the flight phases here are more critical and of brief duration; thus, alternative parameters are required for these essential phases. An external reference from the FAA's ILS/LOC approach guide, seen in Figure 3.7, exemplifies the proper delineation of the final approach phase, initiated by the landing minimums indicated for Runway 30R (in feet).

CATEGORY	A	B	C	D	E
S-ILS 30R		1072/40	250 (300- $\frac{3}{4}$ )		
S-LOC 30R	1320/40	498 (500- $\frac{3}{4}$ )		1320/60	498 (500- $\frac{1}{4}$ )
C CIRCLING	1360-1	518 (600-1)	1460- $\frac{1}{4}$	1660- $\frac{2}{4}$	1800-3
		618 (700- $\frac{1}{4}$ )	818 (900- $\frac{2}{4}$ )	958 (1000-3)	

Figure 3.7 Landing Minimums for ILS/LOC-I Approach onto KMSP Runway 30R (FAA)

TP5, denoting the commencement of the final approach, was determined using radio altitude and ground speed, the latter being shown its typical profile on Figure 3.8. This time point was designated when the altitude fell below 500 feet (151.79 m), contingent upon the ground speed measurement being valid and concurrently sampled with the altimeter reading (non-NaN). TP6, the alternative time point for the final approach, was likewise determined by the height and ground speed also, but with the threshold established at an altitude beneath 250 feet (76.2 m).

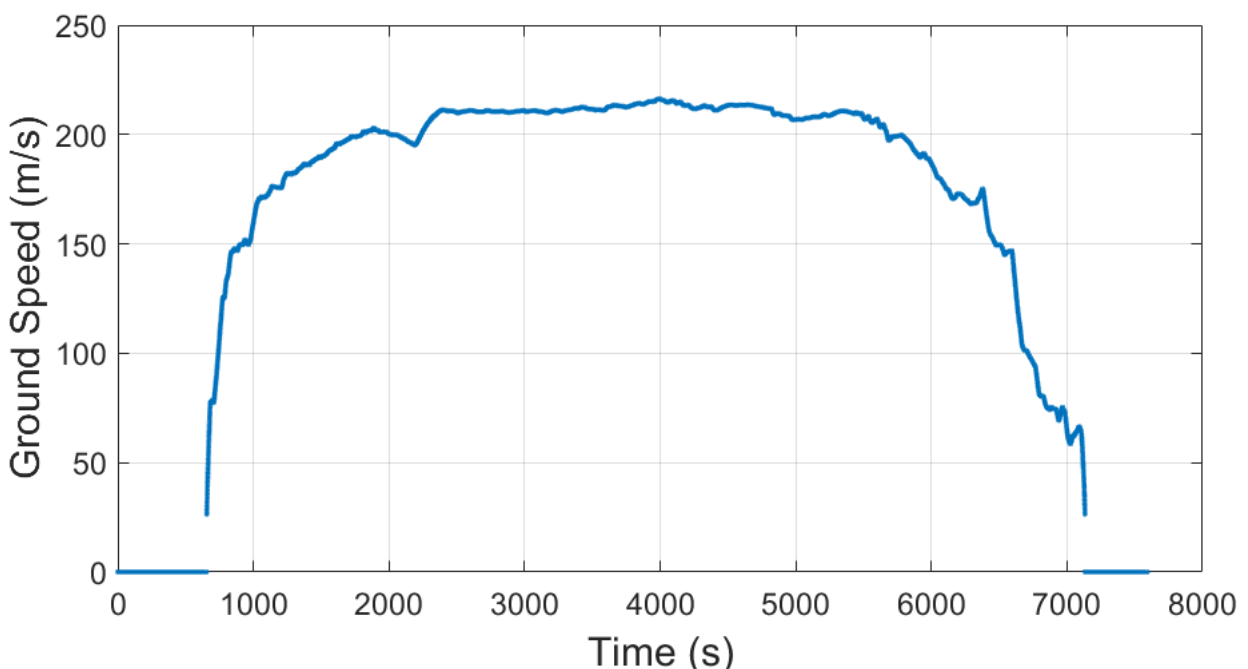


Figure 3.8 Typical Profile of Ground Speed

The reasoning for this alternate time point is to address the issue of instruments used during the final approach. As explained in Section 2, although the primary equipment for instrument precision landings was ILS at the time, localizer systems are also available as backup should the former fail at the time of landing. Therefore, TP5 is meant to reflect the decision point where the pilot has to continue the landing procedure if the aircraft is currently tuned to the localizer frequency.

In contrast, TP6 reflects the normal procedures for landing where the aircraft is tuned to the ILS frequency instead during the approach. In addition to having arbitrary information on the instrument used for landing, the two time points serve as a comparison for the accuracy and precision of the measurement histograms plotted later since these are likely to be brief in time between them (less than 1 minute). Nonetheless, these two time points, TP5 and TP6, will be either discarded in use (the latter) or modified (the former) to better align with the approach window and simulation conditions.

TP7, indicating touchdown and the commencement of landing, depended on the weight-on-wheels sensor. This time point was recognized as the initial occurrence post-TP6 where the sensor signaled ground contact, with the parameter's value established at 0 as shown on Figure 3.9. Ultimately, TP8, signifying the commencement of taxiing and the conclusion of landing, was established by monitoring the trailing edge flap position falling below 5° after TP7.

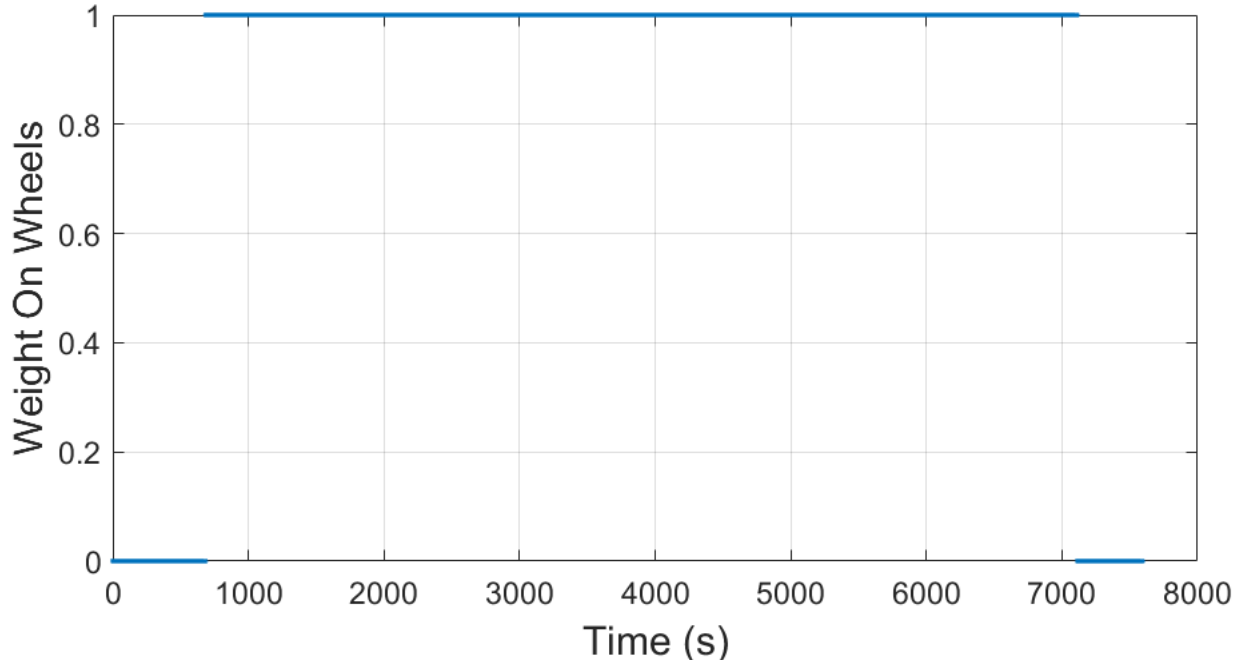


Figure 3.9 Typical Profile of Weight on Wheels

Therefore, the five parameters (flap position, ACMS flight phase, radio altitude, ground speed, and weight-on-wheels) constituted the basis for the time point identification technique. These five were chosen for their direct link with critical operational events, especially during the approach and landing sequence. Their discrete or threshold-based modifications provide distinct markers for phase transitions, rendering them optimal for reliably segmenting the descent profile throughout numerous flights. Additional metrics, such as pitch angle, angle of attack, and wind components, were captured and preserved in the dataset; however, they were employed exclusively for measurements at specific time intervals and did not directly affect the classification or timing of phase transitions.

### 3.2.2 Time Points Results

Figure 3.10 illustrates that the bulk of recorded flights had lengths ranging from around 30 to 120 minutes, with a significant concentration around 45 to 50 minutes, where over 600 flights are aggregated. This indicates that a significant segment of the dataset consists of relatively short- to medium-haul trips (see Figure 3.2 for reference). Outside this range, the frequency progressively diminishes; however, a considerable number of flights surpass 100 minutes, with some exceeding 200 minutes, signifying the presence of long-haul operations as well.

Figure 3.10 Range and Distribution of Flight Time

The classification of flight phases into specific time points was implemented across all accessible datasets. This section presents this process for flights of varying duration to illustrate the algorithm's efficacy and the variability among distinct flight profiles. Each example demonstrates how the specified time points segment the flight profile into various phases: take-off, climb, cruise, descent, approach, landing, and taxi.

First, Figure 3.11 illustrates the algorithm's performance for long-haul trips that are over 8000 seconds (or 133 minutes) long.

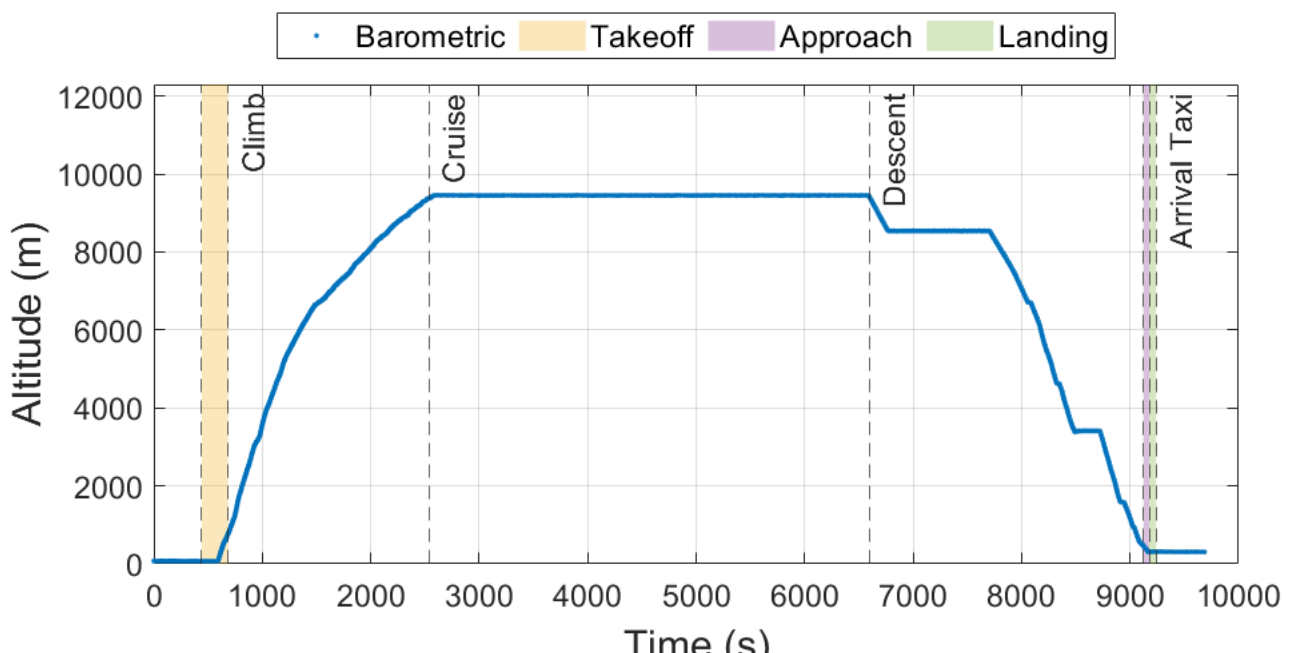


Figure 3.11 Flight Phase Identification of Long Flight

Subsequently, Figure 3.12 illustrates the algorithm's performance for medium-haul flights, defined as those lasting between 4000 and 6000 seconds (or between 67 and 100 minutes).

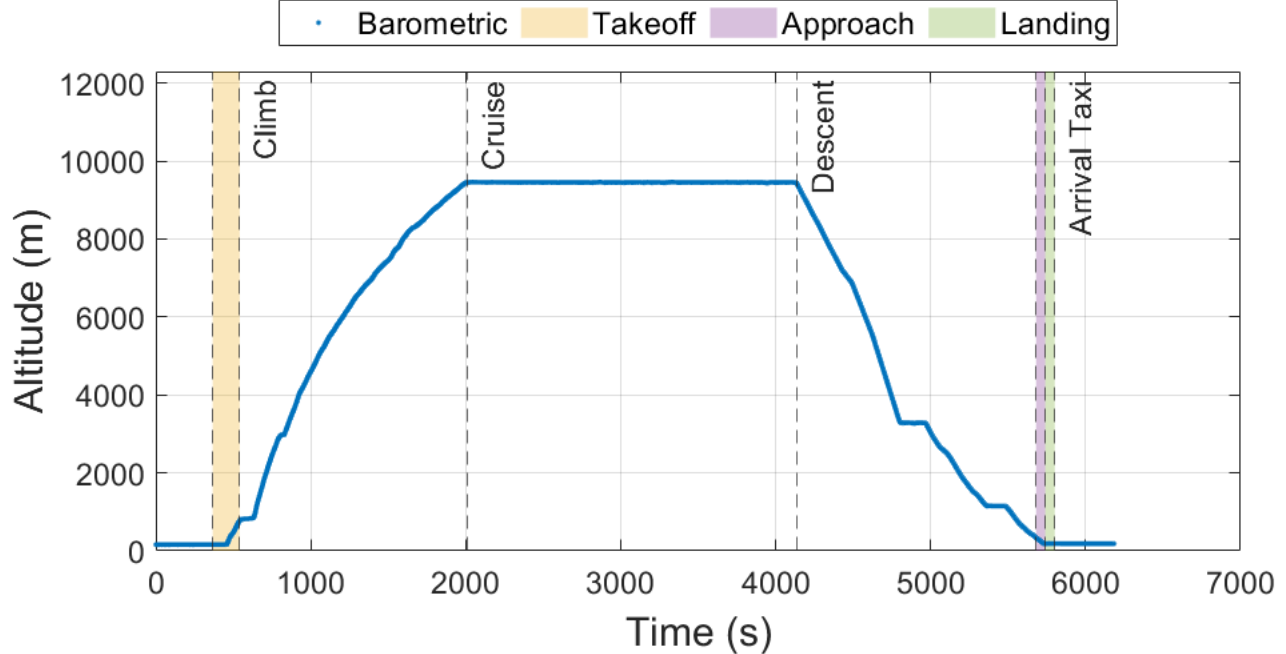


Figure 3.12 Flight Phase Identification of Intermediate Flight

Then, Figure 3.13 illustrates the algorithm's performance for short-haul flights (less than 4000 seconds or 67 minutes).

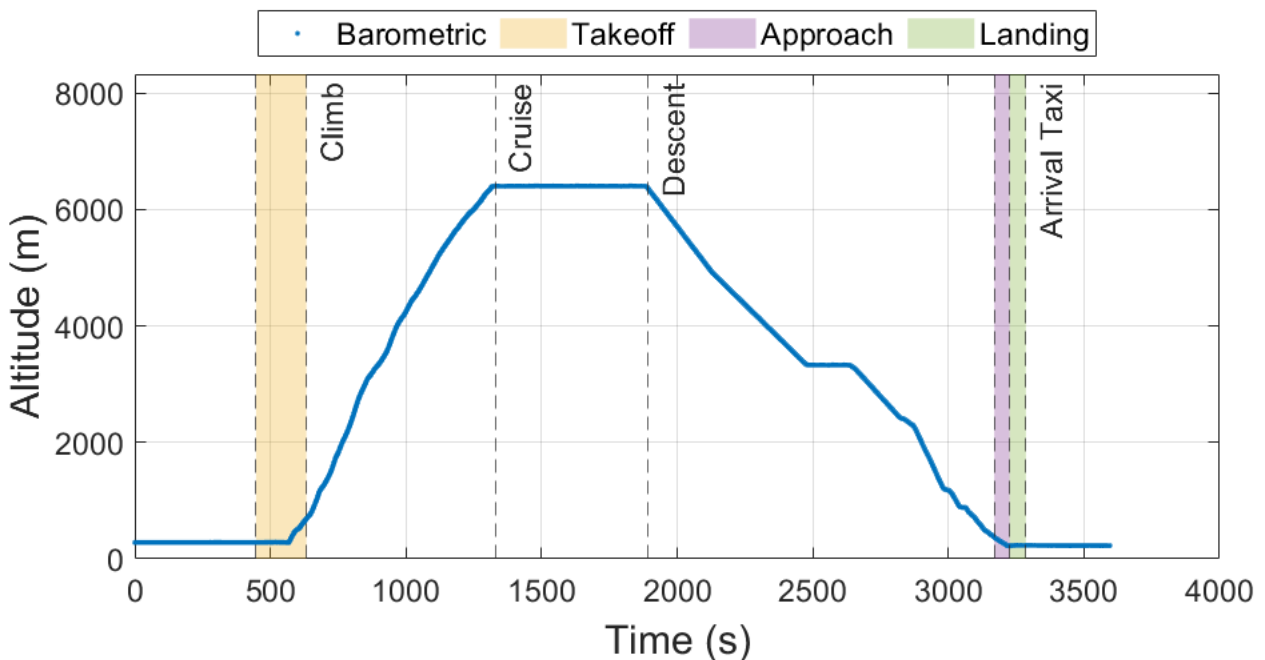


Figure 3.13 Flight Phase Identification of Short Flight

In all cases from Figures 3.11 to 3.13, the criteria for all time points proved exceptionally trustworthy while ensuring proper segmentation of the key flight phases. The time points are indicated by dashed lines, with colored zones between them denoting the flight phase of the region. The graphical representations of these flight profiles also serve as visual confirmation and validation of the method for time point detection and its ability to generalize across various datasets.

### 3.2.3 Validation of Approach Time Points

The validation of TP5 and TP6 was crucial due to their significant role in delineating the commencement of the final approach phase, ensuring uniformity across all datasets. The validation technique entailed comparing the intervals between TP5 and TP7 and between TP6 and TP7 for all flights. The time intervals were then calculated and subsequently shown in histograms in Figure 3.14 to assess their distribution and shape.

Figure 3.14 Range and Distribution of Durations Between TP5 (left) or TP6 (right) With TP7

The bell-shaped characteristics of the histograms highlight the validity of the algorithm's results in identifying these approach time points, guaranteeing that both consistently delineate the designated transition zones into the final approach phase. The bell shape will be further substantiated by examining the distribution of data parameters (refer to Appendix C), where a greater concentration of data is aligned with the mean trendline, diminishing into sparse lines as it approaches the 3 standard deviation boundaries. This consistency substantiates their application for additional analysis, encompassing parameter extraction and distribution fitting, which will be addressed in later sections.

### 3.3 Parameter Measurements at Approach

This section examines the eight designated flight parameters recorded at TP5 and TP6, which represent pivotal moments during the final approach phase. The characteristics, selected for their significance to aircraft performance and stability, were retrieved from all datasets to examine their behavior at these two-time points. These are also characterized as terms commencing with **M** followed by an integer, as delineated in Table 3.2.

Table 3.2 Definition of Measurements

Measurement Parameter	Unit
M1	Ground Speed m/s
M2	Pitch Angle Degrees ( $^{\circ}$ )
M3	Roll Angle Degrees ( $^{\circ}$ )
M4	Vertical Speed m/s
M5	Crosswind Speed m/s
M6	Head/Tailwind Speed m/s
M7	Angle of Attack Degrees ( $^{\circ}$ )
M8	Drift Angle Degrees ( $^{\circ}$ )

#### 3.3.1 Candidate Parameters for Measurement

Eight characteristics were selected for TP5 and TP6, concentrating on aircraft performance, stability, and control during the final approach phase, informed by flight dynamics literature and logical reasoning, to analyze approach consistency. Ground speed was initially incorporated as it immediately reflects the aircraft's velocity to the ground. This parameter is crucial for assessing the stability of the approach, since an erroneous ground speed may result in deviations from the glide path or unsafe touchdown velocities.

The pitch angle, expressed in radians but translated to degrees, quantifies the aircraft's nose orientation. A steady pitch angle is essential for upholding the designated glide slope and ensuring a controlled descent. The evolution of this parameter during a specific flight is illustrated in Figure 3.15 for a standard configuration.

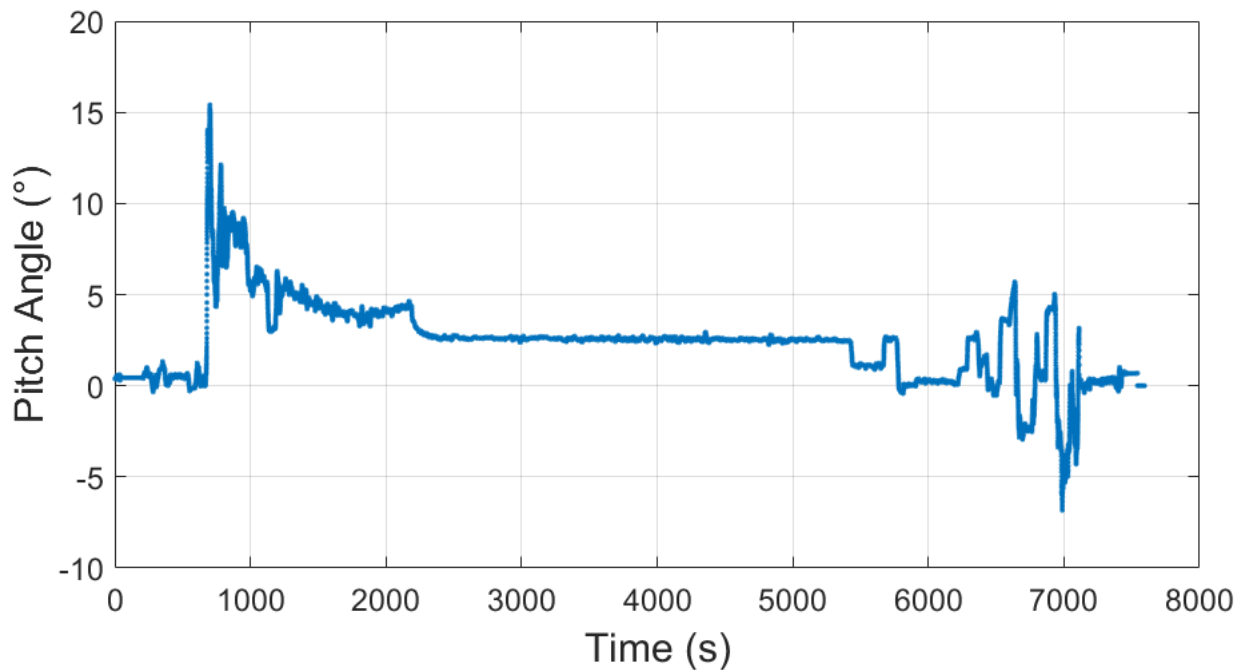


Figure 3.15 Typical Profile of Pitch Angle

The roll angle denotes the aircraft's inclination with the horizon. Roll control is essential for lateral stability, especially during windy approaches or crosswind adjustments. It also offers insight into the aircraft's adherence to the designated approach path. Figure 3.16 shows the evolution of this parameter for a typical form throughout a specific flight.

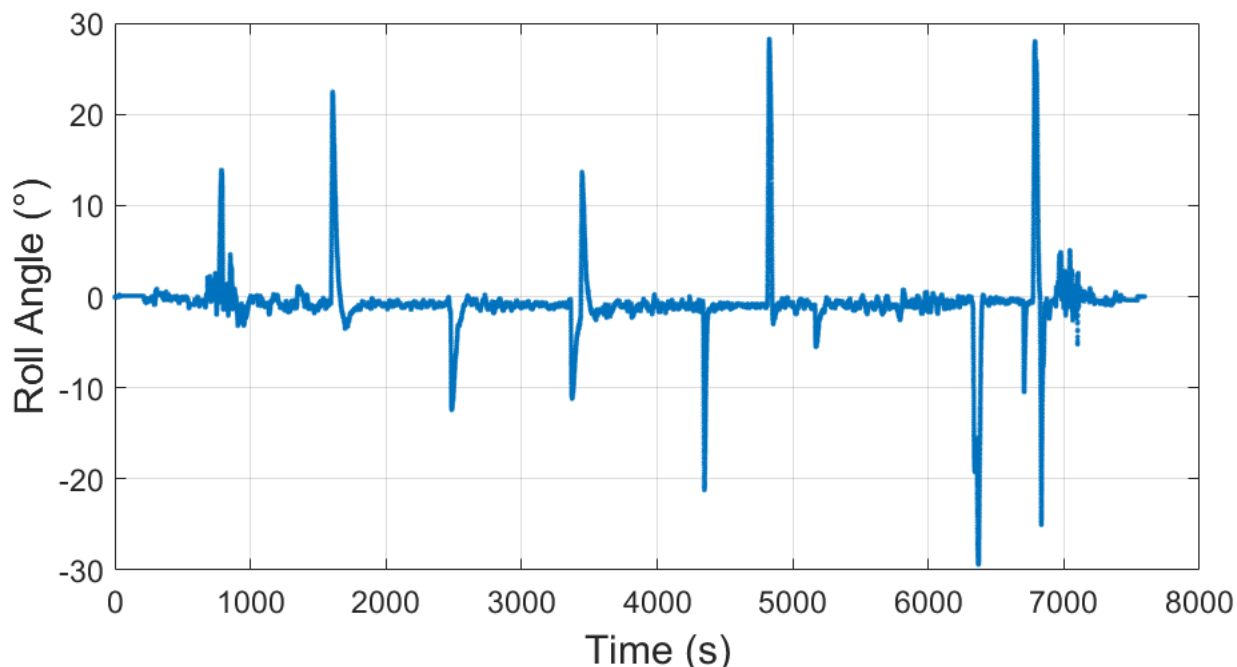


Figure 3.16 Typical Profile of Roll Angle

Inertial vertical speed was chosen for its significance in measuring the rate of descent, a crucial element in evaluating approach stability. Both excessive and insufficient vertical speed may signify an unstable approach, which could result in missed approaches or hazardous landings. Figure 3.17 shows the evolution of this parameter for a specific flight for a typical shape.

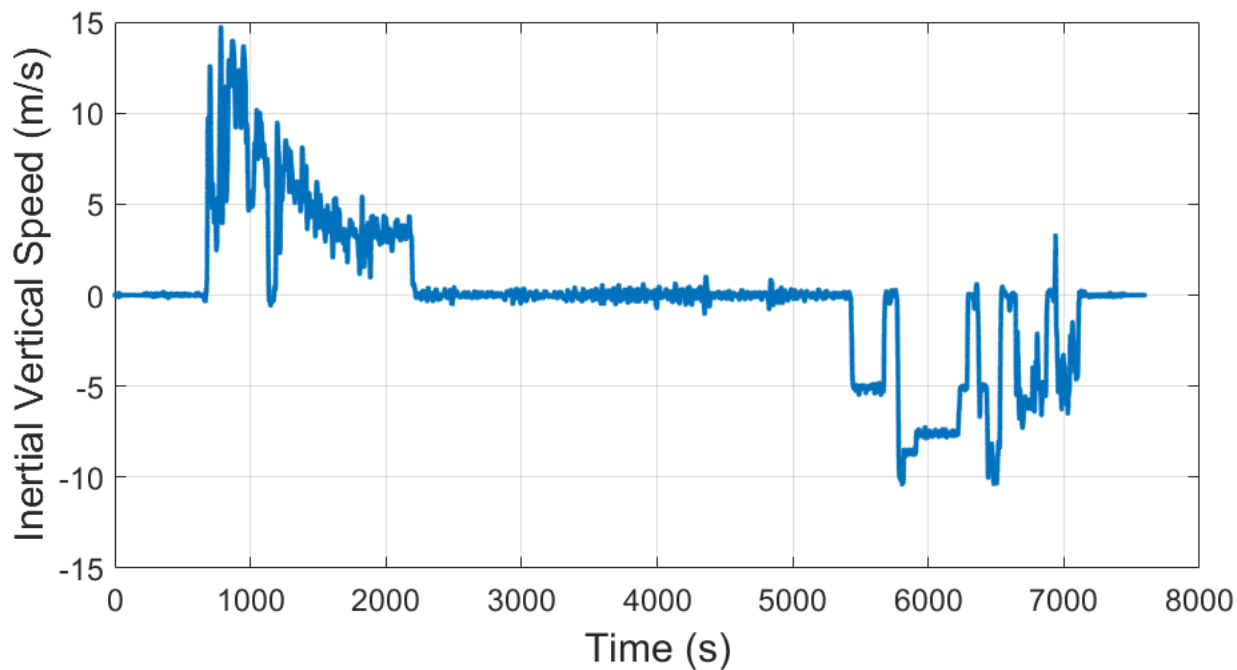


Figure 3.17 Typical Profile of Vertical Speed

Two wind-related parameters, the crosswind component and the headwind/tailwind component, were incorporated based on logical reasoning regarding the impact of wind on approach behavior. The crosswind component is calculated using wind speed, wind direction, and heading to measure the lateral wind forces exerted on the aircraft. This metric is especially valuable for evaluating the influence of crosswinds on trajectory alignment. A positive value signifies a crosswind originating from the left side of the aircraft, whereas a negative value suggests a crosswind from the right.

The variation in wind direction throughout a specific flight is illustrated in Figure 3.18 for a standard configuration.

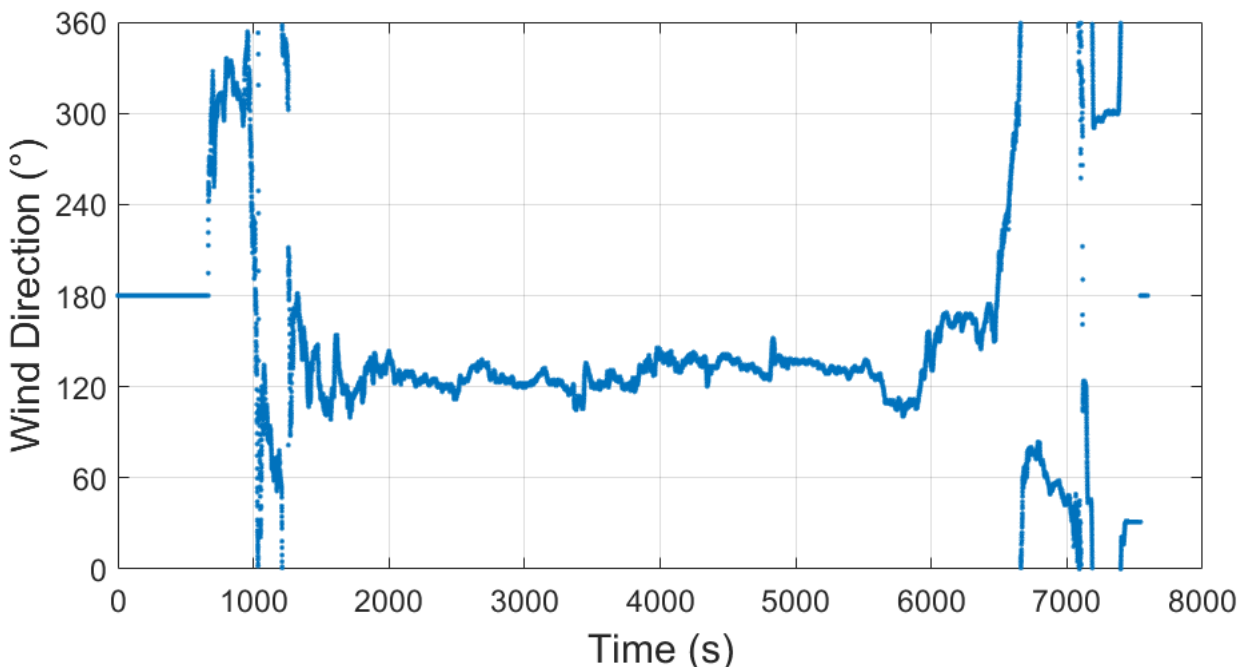


Figure 3.18 Typical Profile of Wind Direction

Subsequently, the evolution of magnetic heading during a specific flight is illustrated in Figure 3.19 for a standard configuration.

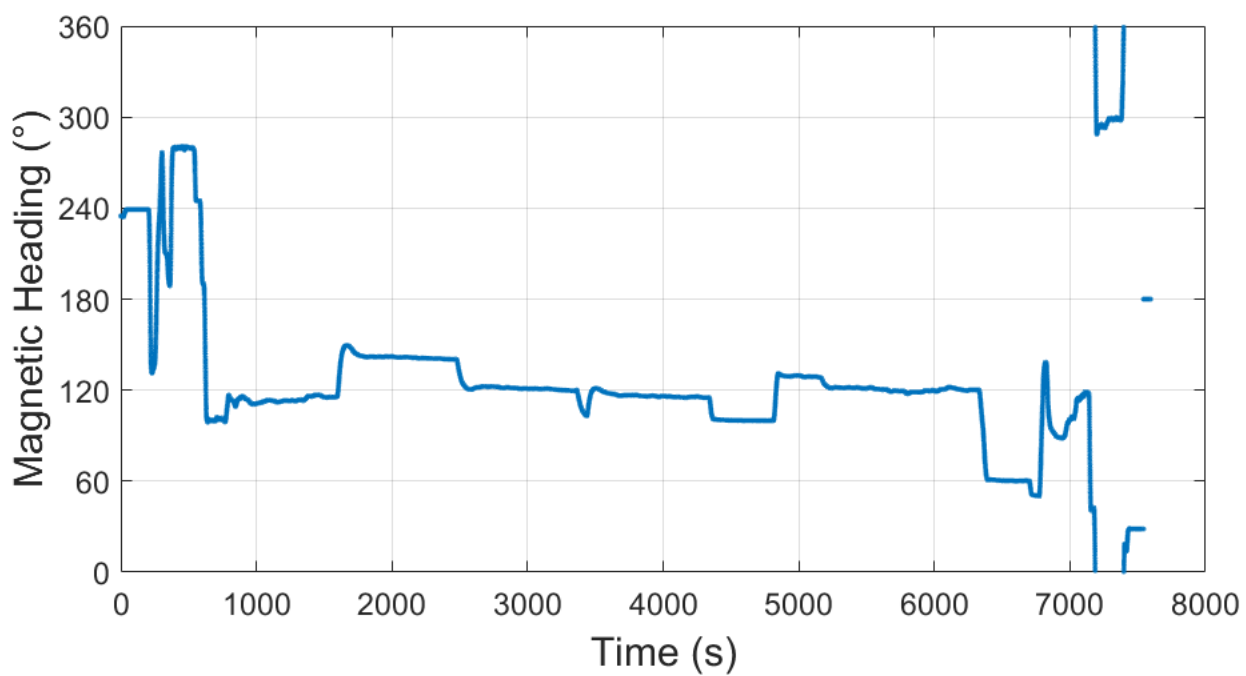


Figure 3.19 Typical Profile of Magnetic Heading

The variation in wind speed throughout a specific flight is illustrated in Figure 3.20 for a standard configuration.

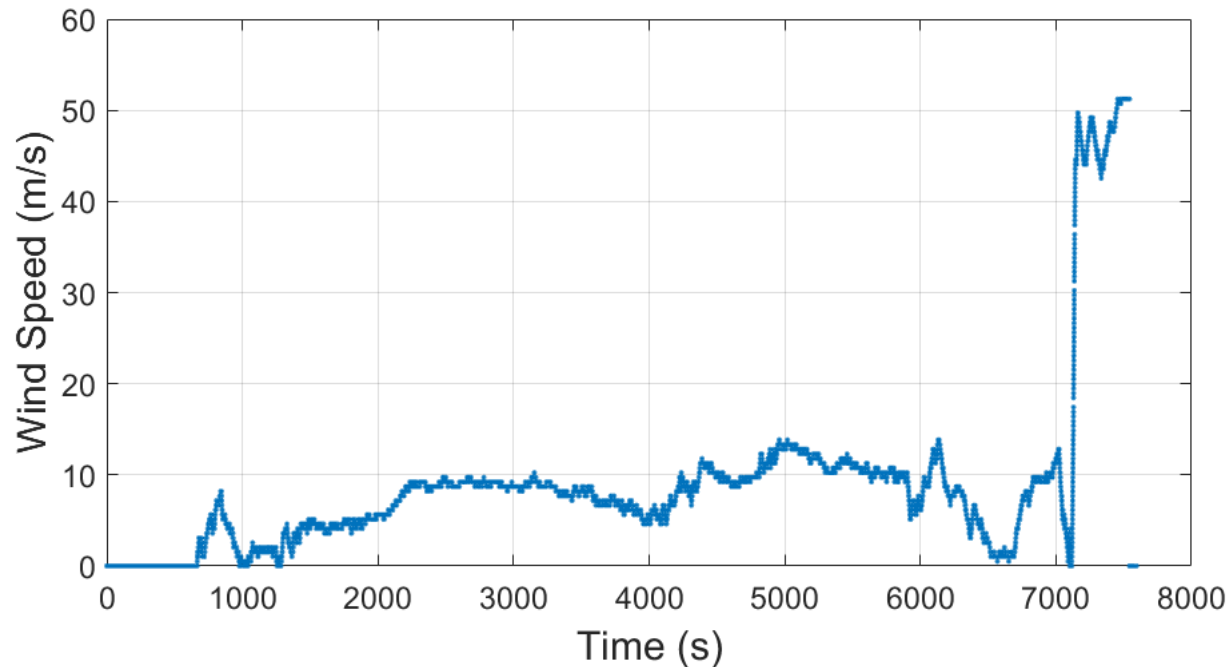


Figure 3.20 Typical Profile of Wind Speed

The headwind or tailwind component, obtained from identical parameters, measures the longitudinal wind forces. This is crucial for understanding the influence of wind conditions on velocity and helps to compute airspeed more accurately than the pitot tube sensor. A positive value signifies a headwind<sup>④</sup>, while a negative value denotes<sup>④</sup> a tailwind. The evolution of crosswind during a specific flight is illustrated in Figure 3.21 for a standard configuration.

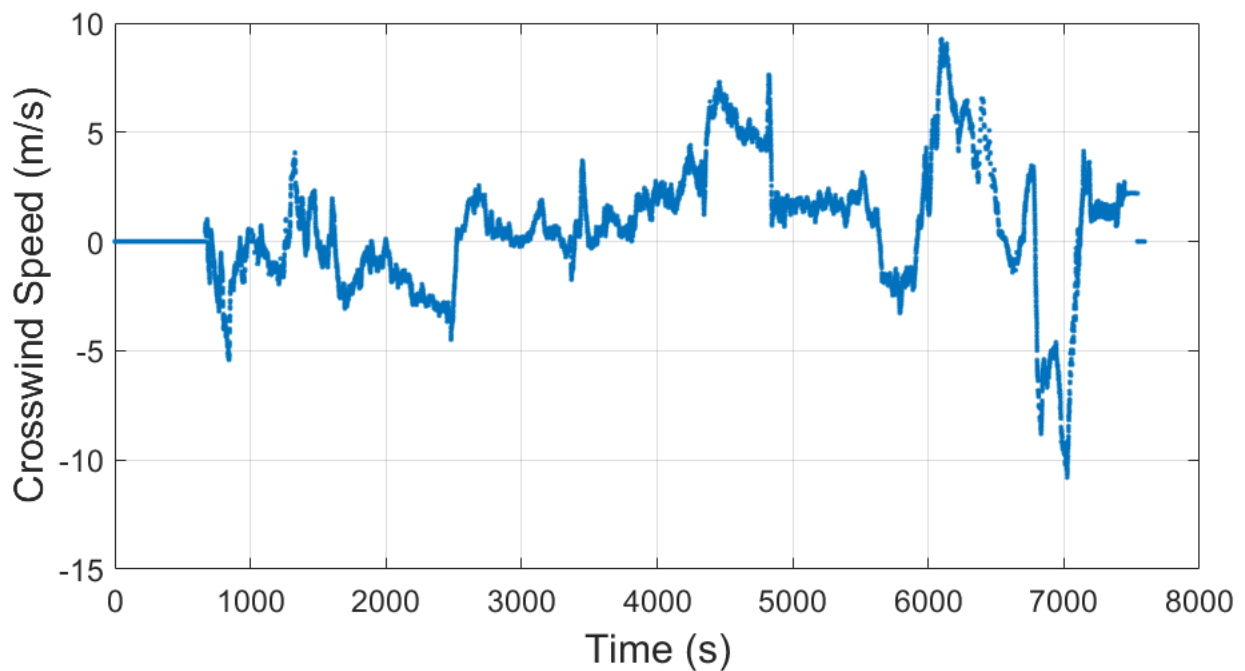


Figure 3.21 Extrapolated Profile of Crosswind

In contrast, the evolution of headwind or tailwind during a specific flight is illustrated in Figure 3.22 for a standard configuration.

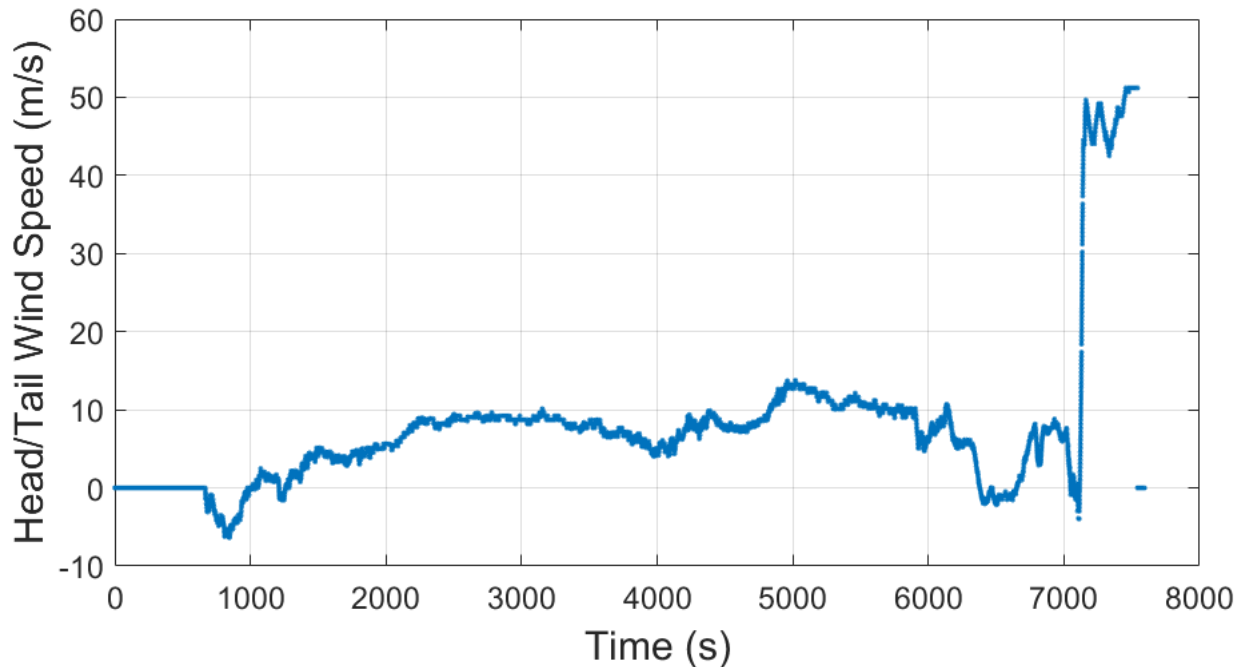


Figure 3.22 Extrapolated Profile of Head/Tailwind

The angle of attack (AoA) is a critical parameter in aerodynamics literature, serving as a crucial indicator of lift and potential stall circumstances. The inclusion guarantees that the analysis encompasses essential data regarding the aircraft's aerodynamic performance in the final phases of flight. The evolution of this parameter throughout a specific flight is seen in Figure 3.23 for a standard configuration.

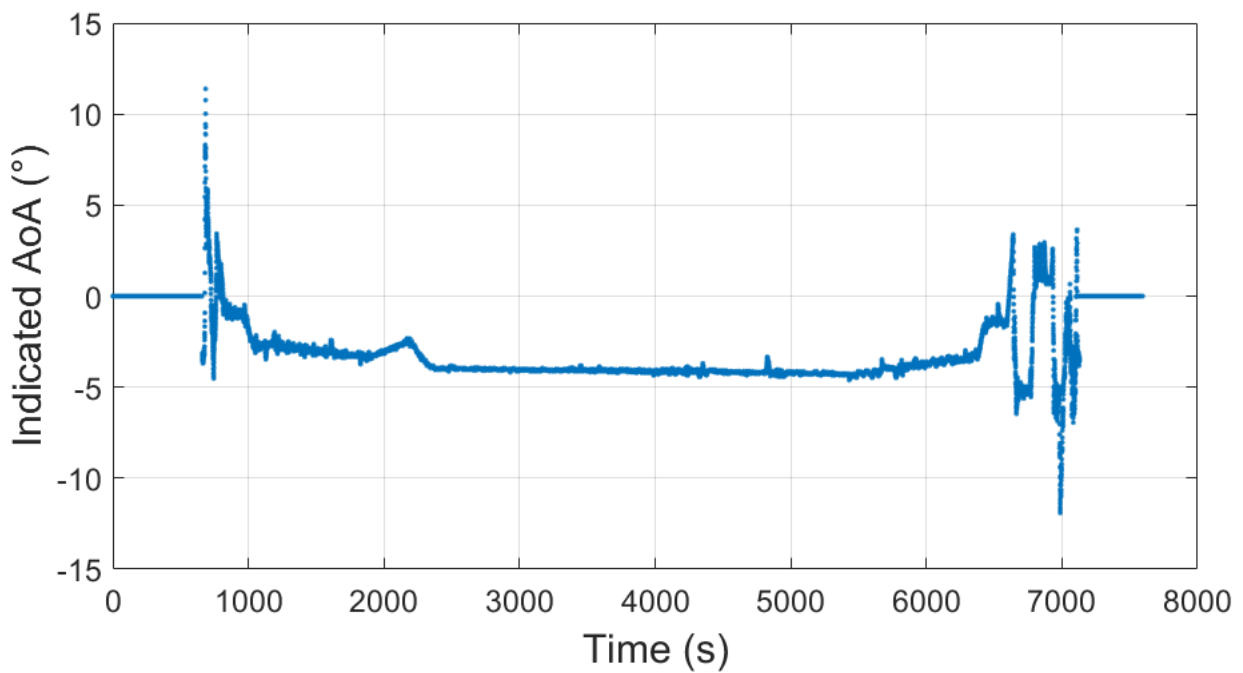


Figure 3.23 Typical Profile of Angle of Attack

Finally, the drift angle denotes the angular disparity between the aircraft's ground track and its heading. This characteristic provides insight into the aircraft's efficacy in counteracting crosswinds to preserve alignment with the runway centerline, essential for a safe and controlled landing. The evolution of this parameter throughout a specific flight is seen in Figure 3.24 for a standard configuration.

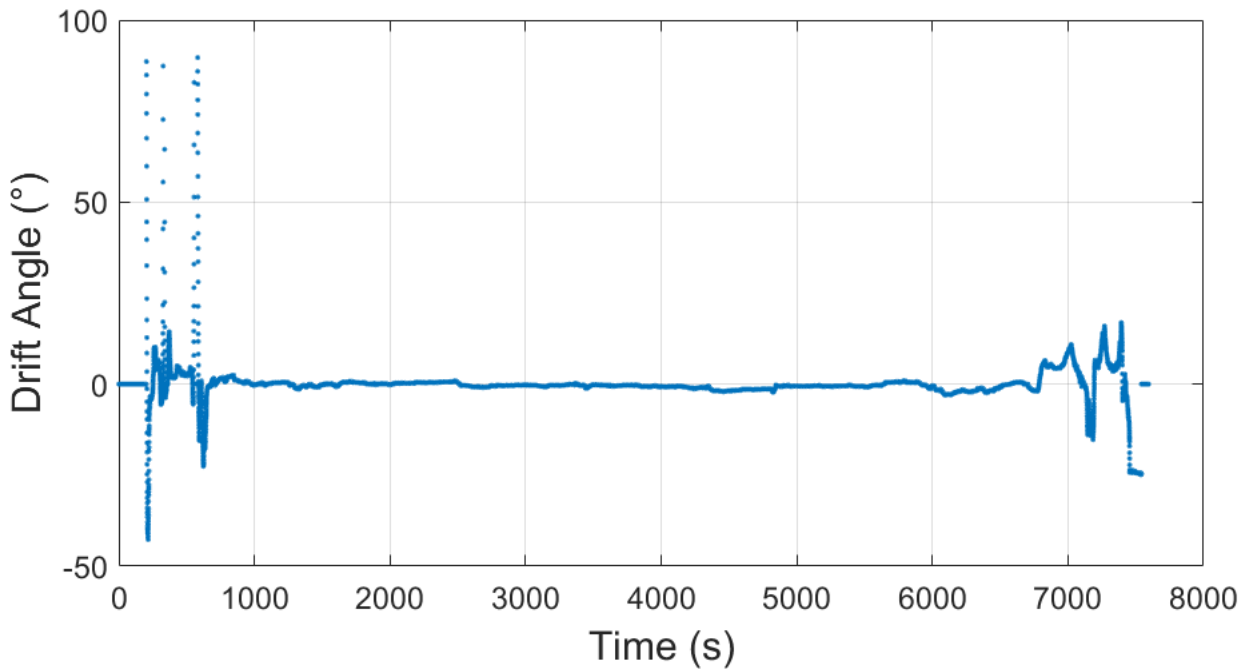


Figure 3.24 Typical Profile of Drift Angle

### 3.3.2 Measurement Results and Analysis at TP5

The examination of TP5 measurements entailed fitting histograms of each parameter to three potential distributions: normal, logistic, and generalized extreme value (GEV). The optimal fit for each parameter was ascertained by evaluating log-likelihood values as seen in Table 3.3, with the maximum value signifying the most suitable distribution in Table 3.4.

Table 3.3 TP5 Log Likelihood Values for Each Distribution Fit

Measurement	Normal	Logistic	GEV
M1	-12 233	-12 284.2	-12 230.3
M2	-7 682.04	-7 703.52	-7 728.2
M3	-6 759.88	-6 708.91	-6 836.21
M4	-5 209.56	-5 197.82	-5 282.37
M5	-11 656.7	-11 679.4	-11 645.1
M6	-11 212.3	-11 207.2	-11 175.5
M7	-9 774.21	-9 794.75	-9 874.72
M8	-11 533.6	-11 583.2	-11 521.8

Although certain parameters adhered to anticipated patterns, others diverged from a normal distribution, potentially due to the sample size of 4,220 flights being insufficient to fully comply with the law of large numbers or the altitude criterion of 500 feet above ground being excessively high, allowing for considerable skew or variation to persist.

Table 3.4 Best Distribution Fits for TP5 Measurements

### Measurement Best Fit Distribution Parameters

M1	GEV	$\mu = 58.637$
----	-----	----------------

		$\sigma = 4.455$
		$\xi = -0.217$
M2	Normal	$\mu = -2.714$
		$\sigma = 1.535$
M3	Logistic	$\mu = -0.076$
		$s = 0.679$
M4	Logistic	$\mu = -3.434$
		$s = 0.476$
		$\mu = -1.458$
M5	GEV	$\sigma = 3.833$
		$\xi = -0.201$
		$\mu = 2.634$
M6	GEV	$\sigma = 3.357$
		$\xi = -0.163$
		$\mu = -5.173$
M7	Normal	$\sigma = 2.538$
		$\mu = -1.269$
M8	GEV	$\sigma = 3.753$
		$\xi = -0.220$

From Table 3.4, the Generalized Extreme Value (GEV) distribution exhibited the optimal fit for five parameters (M1, M5, M6, M8), signifying the existence of heavy-tailed or skewed characteristics in these variables. The remaining parameters were optimally characterized by Normal or Logistic distributions, indicating more symmetric properties.

From Figures 3.25 and 3.26, ground speed (M1), crosswind (M5), head/tail wind (M6), and drift angle (M8) were optimally characterized by the GEV distribution, indicating the impact of fluctuating environmental factors and sporadic extremes. The substantial tails identified by the GEV fit indicate that these parameters exhibit greater fluctuation during the approach.

Figure 3.25 GEV Fits onto M1 and M5 (TP5)

Figure 3.26 GEV Fits onto M6 and M8 (TP5)

Conversely, for Figure 3.27, pitch angle (M2) and angle of attack (M7) exhibited a normal distribution, indicative of robust aerodynamic control and fluid pilot inputs at low altitudes.

Figure 3.27 Normal Fits onto M2 and M7 (TP5)

And for Figure 3.28, the roll angle (M3) and vertical speed (M4) demonstrated a logistic distribution, reflecting the symmetric albeit slightly heavier-tailed characteristics of their distributions, consistent with moderate deviations during stable descent and lateral control.

Figure 3.28 Logistic Fits onto M3 and M4 (TP5)

### 3.3.3 Measurement Results and Analysis at TP6

The examination of TP6 readings adhered to a comparable methodology; however, the patterns seen at a reduced altitude during the final approach phase reveal significant alterations in parameter behavior relative to TP5, indicating enhanced stability as the aircraft approaches the runway. Similarly with Section 3.3.2, Table 3.5 presents the log likelihood values for each parameter fit, while Table 3.6 encapsulates the optimal fit by selecting the maximum value.

Table 3.5 TP6 Log Likelihood Values for Each Distribution Fit

<b>Measurement Normal Logistic GEV</b>	
<b>M1</b>	-11 708.8 -11 758.3 -11 725.8
<b>M2</b>	-6 817.35 -6 835.61 -6 882.20
<b>M3</b>	-6 872.78 -6 861.64 -6 928.57
<b>M4</b>	-3 621.52 -3 610.88 -3 681.61
<b>M5</b>	-10 819.1 -10 842.8 -10 837.7
<b>M6</b>	-10 872.3 -10 892.6 -10 726.1
<b>M7</b>	-9 548.30 -9 543.30 -9 611.66
<b>M8</b>	-10 739.6 -10 791.4 -10 754.8

Table 3.6 Best Distribution Fits for TP6 Measurements

**Measurement Best Fit Distribution Parameters**

		$\mu = 59.985$
<b>M1</b>	Normal	$\sigma = 3.974$
		$\mu = -2.219$
<b>M2</b>	Normal	$\sigma = 1.234$
		$\mu = -0.066$
<b>M3</b>	Logistic	$s = 0.702$
		$\mu = -3.298$
<b>M4</b>	Logistic	$s = 0.323$
		$\mu = -0.037$
<b>M5</b>	Normal	$\sigma = 1.234$
		$\mu = 1.849$
<b>M6</b>	GEV	$\sigma = 2.835$
		$\xi = -0.010$
		$\mu = -4.561$
<b>M7</b>	Logistic	$s = 1.333$
		$\mu = 0.045$
<b>M8</b>	Normal	$\sigma = 3.152$

From Figures 3.29 and 3.30, ground speed (M1), pitch angle (M2), crosswind (M5), and drift angle (M8) were optimally characterized by the normal distribution, signifying steady and predictable values at this stage of the approach. This corresponds with expectations since pilots strive for uniformity in airspeed and trajectory management during the final moments preceding landing.

Figure 3.29 Normal Fits onto M1 and M2 (TP6)

Figure 3.30 Normal Fits onto M5 and M8 (TP6)

Likewise, in Figure 3.31, roll angle (M3) and vertical speed (M4) exhibited a logistic distribution, reflecting symmetric deviations around the mean with marginally thicker tails, indicative of small adjustments during descent.

Figure 3.31 Logistic Fits onto M3 and M4 (TP6)

For Figure 3.32, the head/tail wind (M6) exhibited a GEV distribution, indicating the preference for headwind conditions, even at reduced altitudes. The angle of attack (M7) was more accurately characterized by a logistic distribution at TP6 as seen on Figure 3.32, indicating increased variability as the aircraft modifies its glide path.

Figure 3.32 (left) GEV Fit onto M6 and (right) Logistic Fit onto M7 (TP6)

The study reveals significant differences in the distribution patterns of key flight parameters between TP5 and TP6, with TP5 showing greater variability in parameters like ground speed, crosswind, and head/tail wind, suggesting environmental factors and pilot adjustments play a more significant role. By TP6, parameters like ground speed, pitch angle, and drift angle shift toward normal distributions, indicating stable flight conditions.

## Chapter 4

### Modelling and Simulation

#### 4.1 Modelling

This section presents the development of a physics-based model designed to estimate the overall mechanical energy of the aircraft during the final approach phase. The approach focuses on estimating energy evolution through a steady-state representation of aerodynamic forces and aircraft motion, rather than employing a comprehensive six-degree-of-freedom flight dynamics model. The model integrates kinetic and potential energy obtained from QAR measurements to assess the aircraft's immediate energy status. This is pivotal in assessing the probability of stall or LOC-I scenarios under diverse flying conditions, serving as the basis for the subsequent subset simulation and risk quantification processes detailed in later sections.

##### 4.1.1 Model Formulation

A physics-based total energy model is designed to assess the aircraft's energy dynamics during approach and landing. This model estimates the evolution of mechanical energy by employing flight dynamics concepts and fundamental representations of aerodynamic forces. This energy-focused model provides a pragmatic abstraction for intricate aircraft dynamics and facilitates direct comparison with empirical energy profiles derived from flight data.

The starting point of the formulation is the concept of total mechanical energy, which combines kinetic and potential energy. Based on recorded flight parameters, this is computed as:

(4.1)

In this context,  $m$  represents the overall mass of the airplane (kg),  $V$  denotes the airspeed (m/s),  $g$  signifies the gravitational acceleration ( $9.81 \text{ m/s}^2$ ), and  $h$  indicates the radio altitude (m). This energy signifies the aircraft's immediate mechanical condition derived from sensor data. The model then calculates the rate of energy change over time and integrates it to provide a corresponding energy curve. This rate is determined by the dot product of the net force vector and the velocity vector as:

(4.2)

To get the modeled total energy trajectory across time, the scalar energy rate is subjected to numerical integration (from  $a$  to  $b$  via the trapezoidal rule) to produce a continuous approximation of  $E_{\text{model}}(t)$  by:

(4.3)

(4.4)

To tackle Equation 4.2, first, the force vector in the body axes encompass aerodynamic forces, gravitational components, and engine thrust [23] which results

(4.5)

Where  $S$  is the reference area ( $\text{m}^2$ ), and the dynamic pressure is calculated as:

(4.6)

Next, the aircraft's mass comprises its empty weight, current payload weight (including crew, passengers, and baggage, estimated at 50-70% of the permissible maximum), and current fuel weight. The first two are maintained constant based on Boeing's specifications [24], while the latter is derived by aggregating the fuel quantity  $Q$  in each tank of the aircraft as per the flight data. Therefore,

(4.7)

The dynamic pressure  $\bar{q}$  and the air density  $\rho$  fluctuate with altitude, with the latter being approximated by the barometric (ISA) formula [25] as:

(4.8)

To ascertain the aerodynamic forces in the body-axis frame, the lift and drag coefficients are converted utilizing the angle of attack  $\alpha$  with the following transformation:

(4.9)

The lateral force coefficient and the estimated sideslip angle, which the latter is not present in the flight data, are calculated as follows:

(4.10)

(4.11)

The aerodynamic coefficients are linearly parameterized according to flight conditions and control inputs. For Equations 4.10, 4.13, and 4.14, static derivatives are derived from US DATCOM and are considered adjustable parameters in the model. Regarding both the lift and drag coefficients:

(4.12)

(4.13)

Since only  $N_1$  is available in the flight data, the thrust force  $T$  is represented as a function of the engine fan speed to the power of an exponential factor (around 1.4 – 2.2) and maximum thrust [26] [24].

(4.14)

The velocity vector  $v$  is a decomposition of the aircraft's speed  $V$  along the three directional axes, where:

(4.15)

Ultimately, by amalgamating all formulas from 4.5 to 4.16, the energy rate utilized in the model is a function of these inputs:

(4.16)

Overall, this function in Equation 4.16 represents the relationship between energy change and quantifiable flight dynamics factors as well as internal state variables. It constitutes the foundation of the simulation model employed to rebuild energy evolution from fundamental principles and will serve as the primary parameters of interest (see Section 4.2.4, 4.2.5, and 5.2) throughout the simulation and subsequent analysis.

##### 4.1.2 Model Simulation

This section now tries to model total energy dynamics during aircraft approaches by simulating real-world energy behavior based on the previous section. This is later compared with actual flight data, which was then retrieved and resampled at 1 Hz to minimize file sizes and the computing duration for simulation. It is the hope that this model sought to reproduce and predict energy dynamics within a certain time interval preceding TP7.

Via the model simulation process, the flight dataset gives out two files: one with recorded flight data and the other with model-generated outcomes. Each row denoted an individual flight, whereas each column indicated a particular time step, except for the initial column, which contained flight identification. The range of the analysis was

restricted to the altitude range of 1000 feet AGL to 0 feet AGL, concentrating on the final phase of approach. An analysis of a histogram on Figure 4.1 depicts flight durations revealed a maximum recorded value of roughly 150 seconds, chosen to encompass the complete relevant length of the approach.

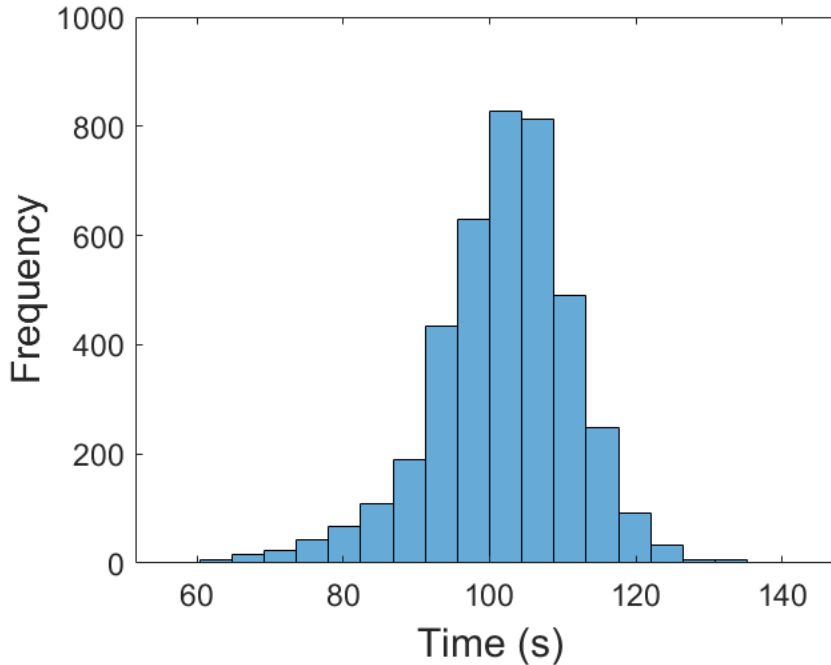


Figure 4.1 Range of Durations for Final Approach

Data integrity was maintained by removing outliers, namely flights with total energy values at the 120<sup>th</sup> second (before touchdown) that were outside a reasonable range, thereby preventing distorted or non-physical results from affecting the statistical analysis of energy patterns. The datasets were then smoothed of noise (with a moving average filter) and transposed to align with the same time intervals, utilizing a time vector ranging from 0 to 150 seconds. Statistical descriptors, such as mean total energy and upper and lower bounds, were computed for each time step, facilitating the comparison of central tendency and dispersion between actual and model datasets as seen in Figure 4.2.

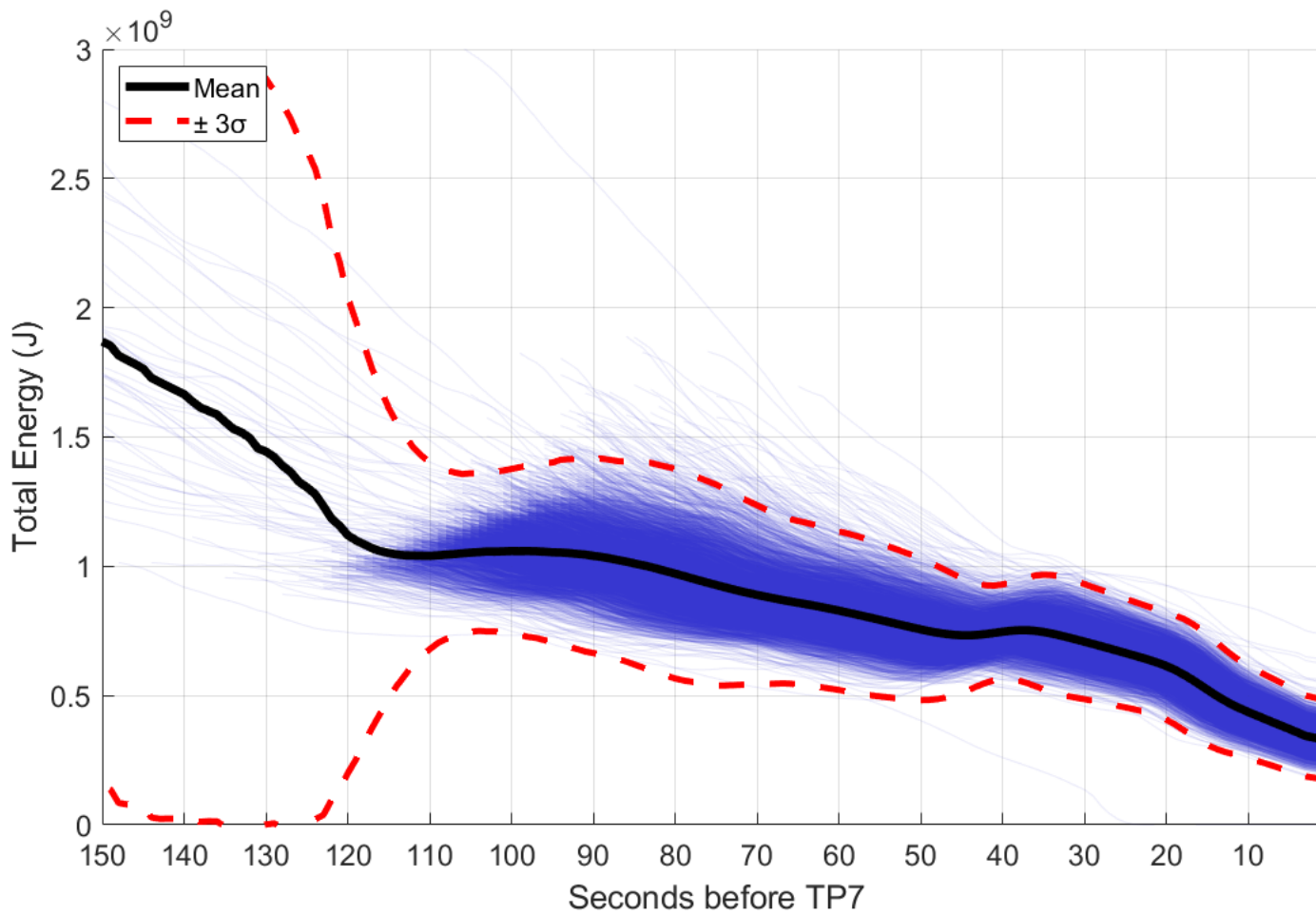


Figure 4.2 Total Energy Progression Based on Flight Data

Figure 4.4, with an overall view between the two, emphasized the temporal progression of mean total energy and the corresponding variability for both datasets. Ideally, the model's mean energy curve would align within the variability range ( $\pm 3$  standard deviations) of the real data, signifying that the model accurately reflects both the average trend and the inherent variability observed across several flights. This alignment suggests that the model represents both the average behavior of descent and the distributional characteristics and random fluctuations seen in operational situations, which is better seen in Figure 4.4. A stronger correlation between the modeled curve and the actual variability band would've enhanced the validity of the assumptions inherent in the model and its application in probabilistic risk assessment.

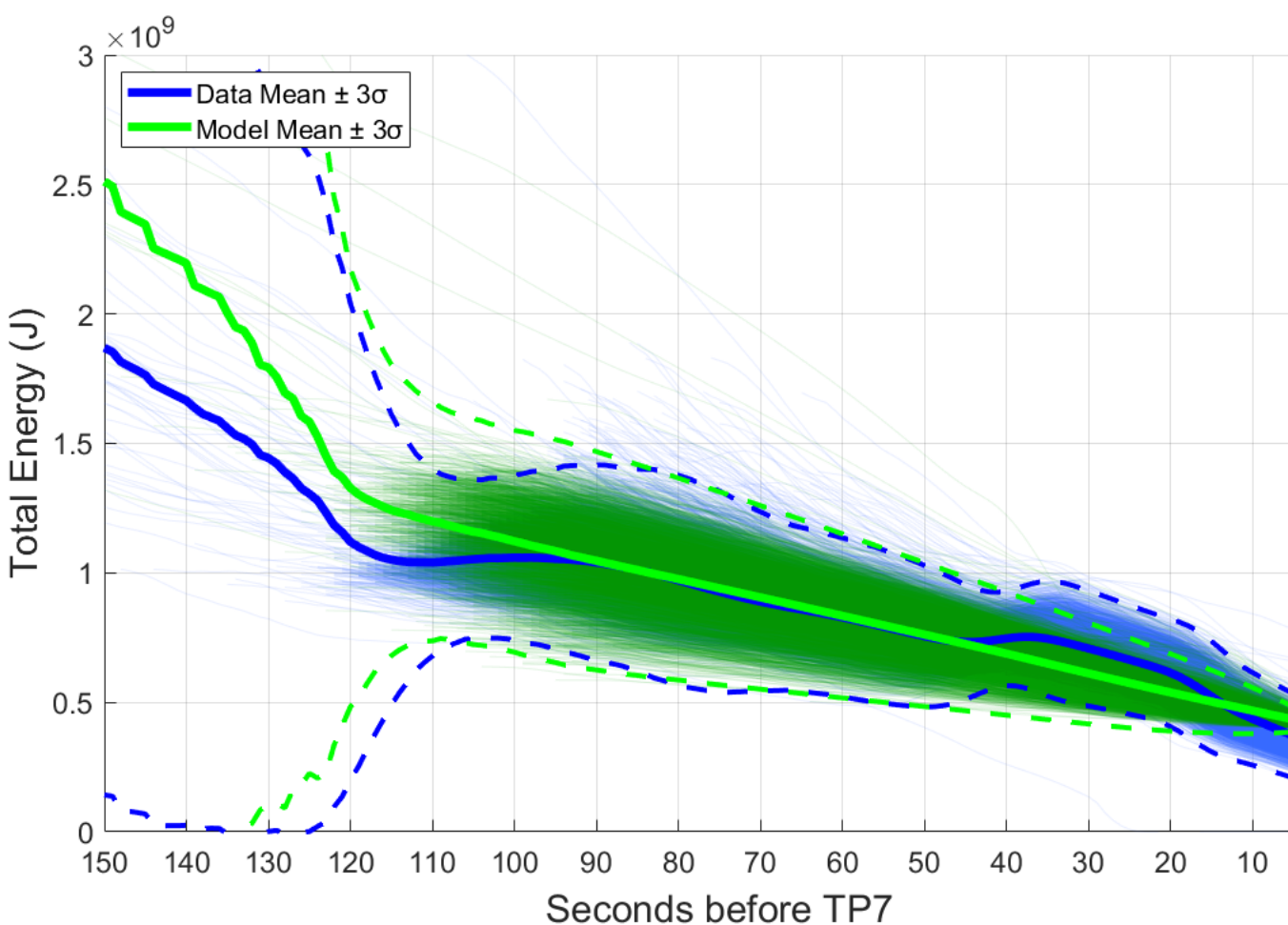


Figure 4.3 Comparison of Model-Based and Data-Based Total Energy

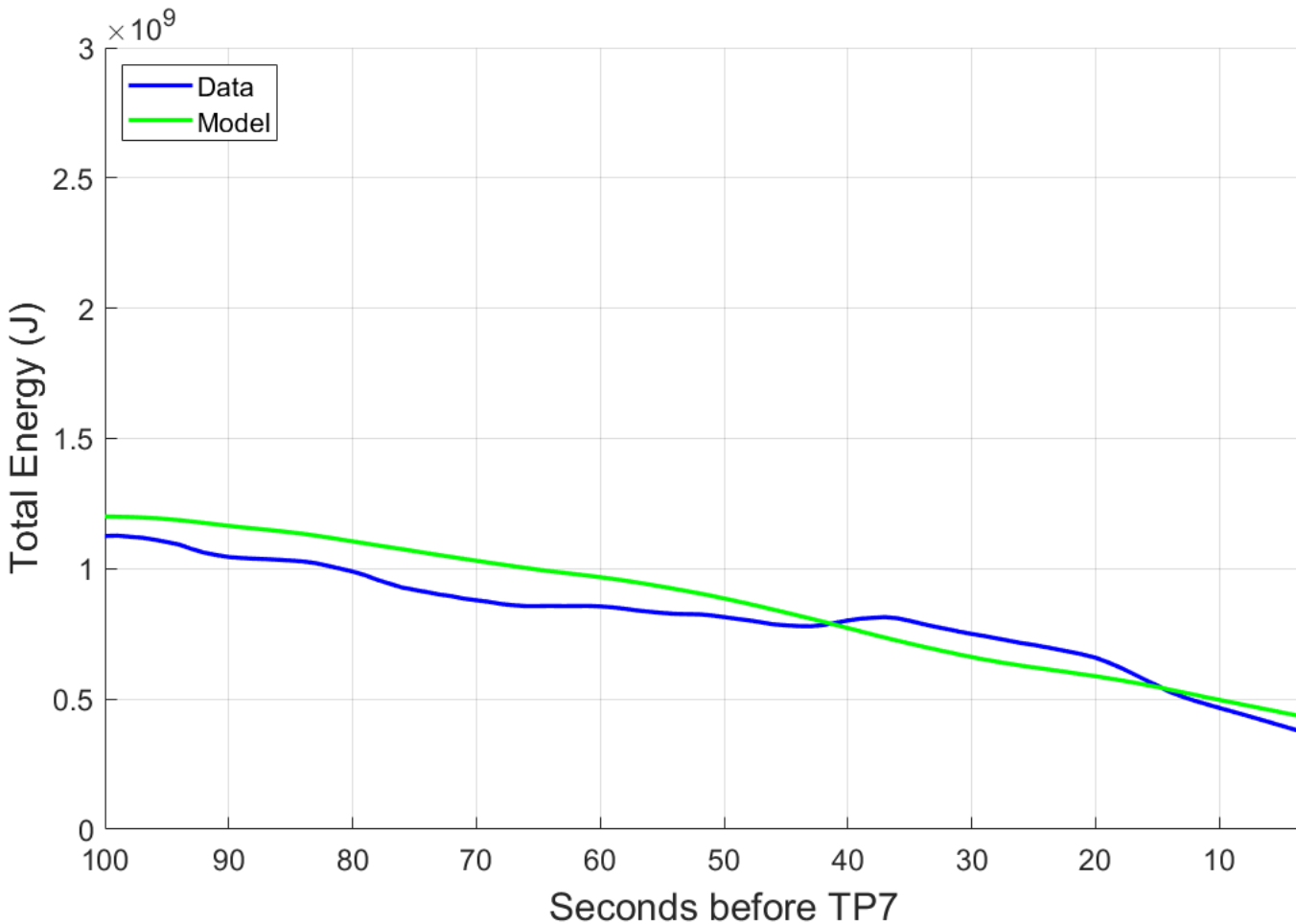


Figure 4.4 Total Energy Comparison for a Singular Flight

Nonetheless, some discrepancies were observed toward the conclusion of the time frame, when the model frequently miscalculated total energy in comparison to the actual flight data. The mismatch seems to stem more from the data than from restrictions in the model itself. The radio altimeter readings during certain flights exhibited an unforeseen increase towards the conclusion of the approach segment (around 40 seconds before touchdown). To start investigating, Figure 4.5 presents an aerial perspective of the approximate flight trajectories of every aircraft landing on KMSP Runway 30R.



Figure 4.5 Final Approach Trajectories onto K MSP Runway 30R

Based on the mapped trajectories provided by Figure 4.3, the noted rise in data-derived energy between 40 and 20 seconds before touchdown can now be ascribed to fluctuations in radio altitude measurements. The anomaly is likely attributable to the aircraft traversing a terrain depression of the Minnesota River and Fort Snelling State Park, situated near the approach end of the runway at K MSP. The measurement of radio height is relative to the terrain directly underneath the airplane; so, this terrain dip briefly elevates the recorded altitude, resulting in a transient increase in calculated potential energy. Consequently, the energy augmentation in this interval does not signify an authentic aircraft maneuver or thrust variation but instead indicates a terrain-induced distortion in the sensor input.

#### 4.1.3 Model Validation

The model's capacity to reproduce the energy dynamics of actual flight data was evaluated by comparing the cumulative total energy across time. Validation emphasized the integral of the total energy curve across the approach time, reflecting the cumulative energy behavior during the descent, rather than merely pointwise comparisons. This method considers both the extent and duration of deviations across time, providing a more thorough metric. The regions were subsequently pooled across all flights and represented as histograms on Figures 4.6 and 4.7 to facilitate visual comparison of the distributions. A significant overlap between the histograms would suggest that the model accurately reflects the normal energy evolution patterns seen in actual flights, but systematic deviations or changes in form may reveal potential biases or oversimplifications in the modeling assumption.

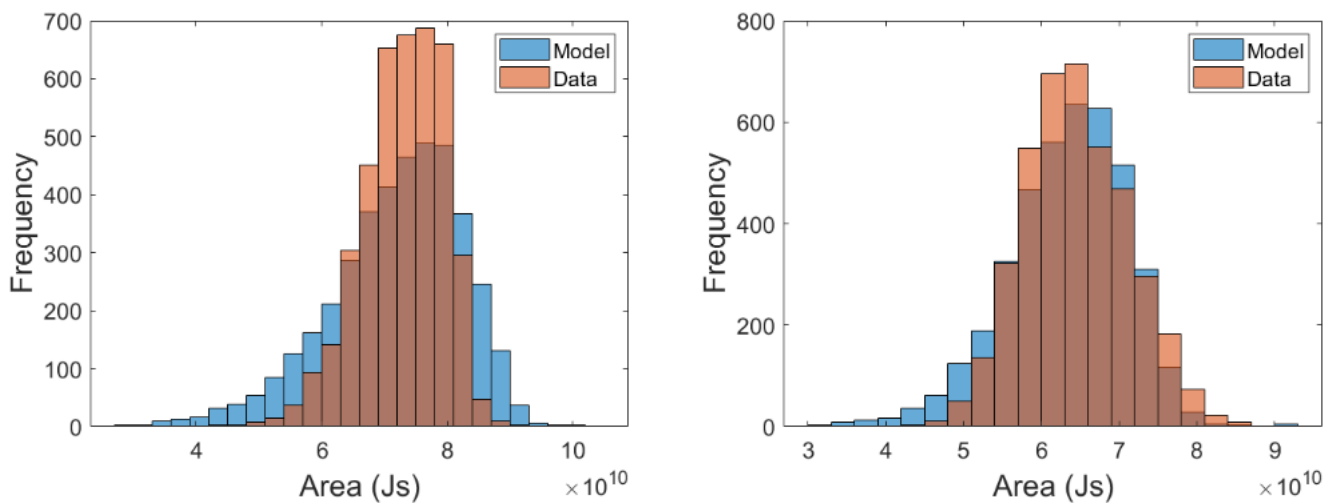


Figure 4.6 Cumulative Energy Comparison for Integration Upper Limit of (left) 90 s and (right) 100 s

The displayed histograms correspond to various integration upper limits from TP7. Although the means of the distributions remain reasonably similar, the variance increasingly diverges as the integration limit rises. This pattern indicates that the model's accuracy remains consistent throughout most of the approach, but the final dynamics near touchdown are more susceptible to fluctuation and modeling error. A possible explanation for this mismatch is the divergence of energy values further away from touchdown. The origin of this increase in variance remains ambiguous, whether it is due to sensor constraints in some of the measurements of parameters or simply to the numerical integration process. Therefore, discrepancies in the > 100 s range underscore the validation metric's susceptibility to end-phase dynamics. A 95-second integration limit was then selected as the optimal compromise, facilitating enough meaningful data while minimizing excessive variance divergence as seen in Figure 4.7. This guarantees a more comprehensive dataset for subsequent phases and preserves a satisfactory alignment between the model and data, particularly for subset simulation.

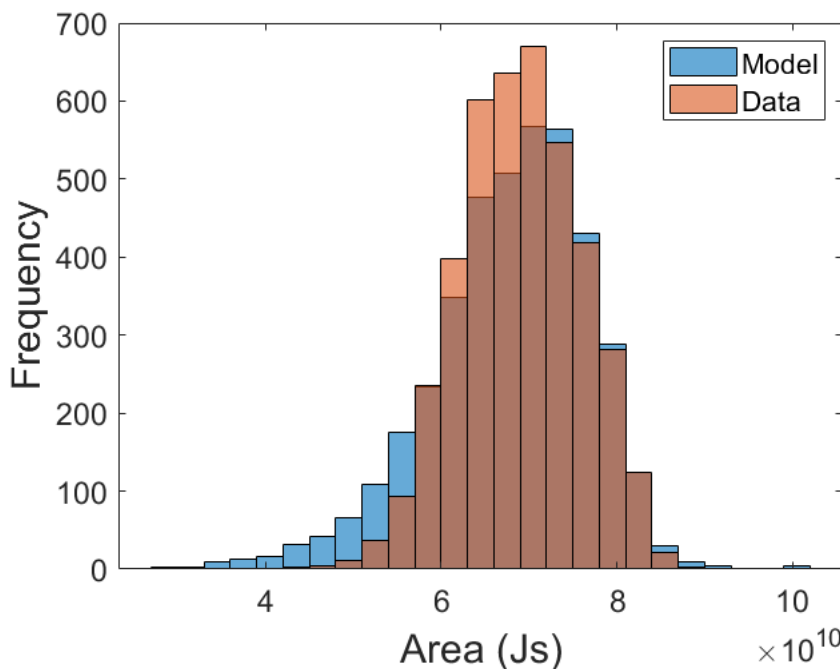


Figure 4.7 Cumulative Total Energy Comparison for 95 s Upper Integration Limit

Figure 4.7 is supplemented by Tables 4.1 and 4.2, which present statistical values of the histogram data and potential distribution fits, analogous to the methodology in Chapter 3. The Normal distribution is identified as the most appropriate representation for the model-based energy area histogram. Furthermore, for Table 4.1, the close alignment of the means indicates that the model effectively estimates the overall energy expended during the approach phase. The standard deviation of the model-based energy distribution is significantly bigger than that of the actual data, indicating a wider dispersion and increased variability in the simulated outcomes. The relative standard deviation difference of 31.94% indicates that, although the model accurately reflects the central tendency, it may generate greater dispersion than what is shown in actual operations. The heightened variability may arise from simplifications in the modeling assumptions or susceptibility to parameter variations, necessitating further refinement if accurate distributional alignment is essential for further risk simulations.

Table 4.1 Energy Area Distribution Comparison

Type	Mean	Standard Deviation
Data		
Model		
Difference		

Table 4.2 Energy Area Distribution Fits

PDF Fit Distribution Parameters Log Likelihood		
	$\mu = 6.91 \times 10^{10}$	
Normal		-98 250
	$\sigma = 6.83 \times 10^9$	
	$\lambda = 7.57 \times 10^{10}$	
Burr	$c = 13.736$	-98 289.4
	$k = 2.645$	
	$\mu = 6.91 \times 10^{10}$	
Logistic		-98 330.1
	$s = 3.76 \times 10^9$	

#### 4.1.4 Residual Analysis

The model's adequacy and the foundational assumptions of the regression framework were evaluated by a comprehensive residual analysis, a conventional method for assessing the validity of linear modeling techniques. This research utilized three diagnostic plots to evaluate essential statistical assumptions: homoscedasticity (constant variance of residuals), independence (absence of autocorrelation), and normality (Gaussian distribution of residuals). Collectively, these diagnostic instruments offered an extensive assessment of the model's statistical reliability and identified any structural anomalies that could undermine its appropriateness for probabilistic simulation.

These diagnostic tools are a critical precondition before utilizing the model for probabilistic simulation. Observable breaches of the fundamental assumptions may signify structural inadequacies in the regression model and jeopardize the validity of the simulation results. Consequently, doing this residual analysis is not merely a statistical formality but an essential validation step to guarantee that the model's behavior under uncertainty stays credible and interpretable during the risk estimation process.

In Figure 4.8, the average of the residuals over time does not consistently align with zero. This is especially evident in the initial 40–50 seconds of the examined period, where a noticeable deviation from the zero line remains. It indicates the existence of a systematic modeling bias, or a deterministic element not accounted for by the existing framework.

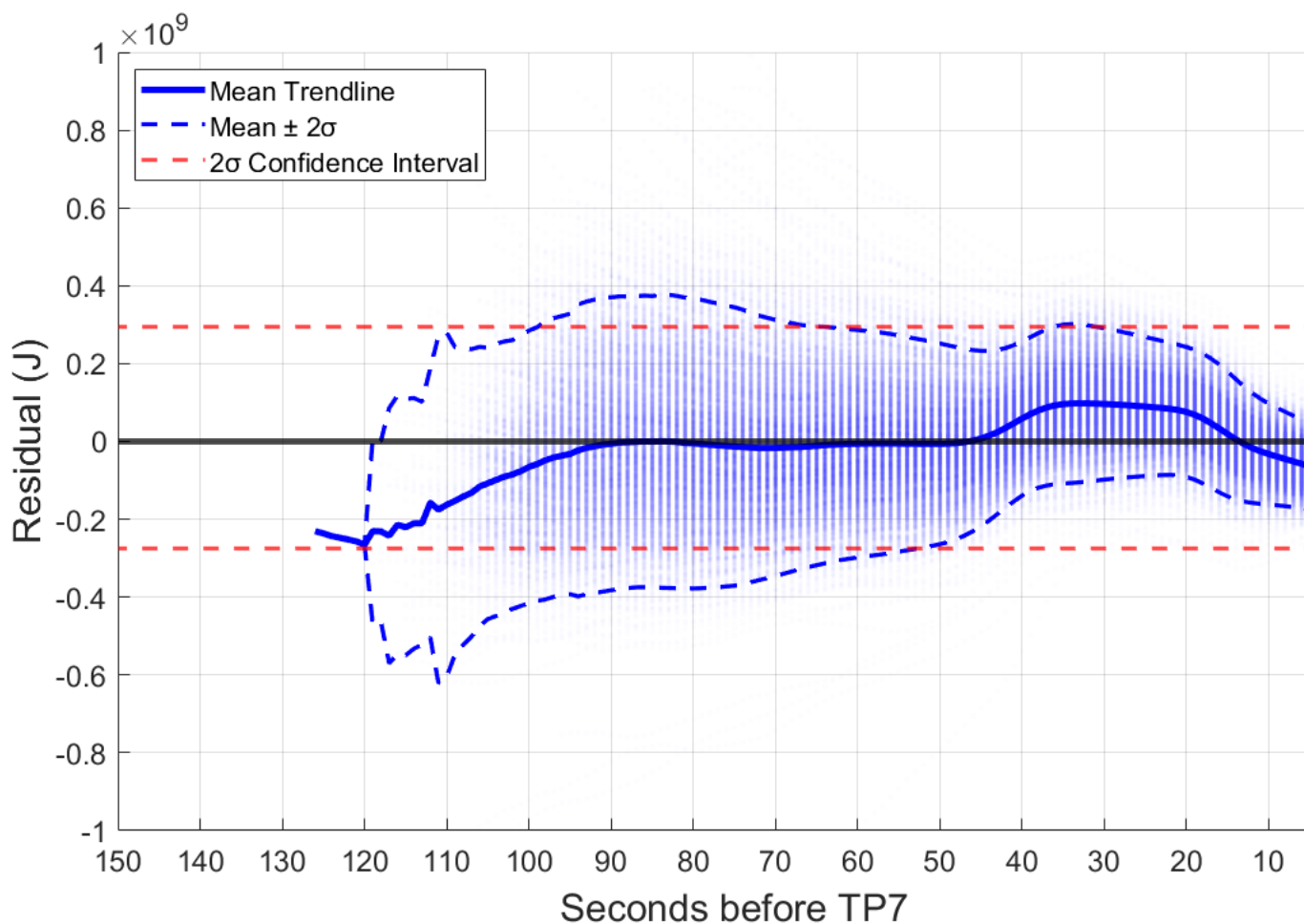


Figure 4.8 Residuals vs Time Plot

The residuals of the regression model, when plotted against the projected output as seen in Figure 4.9, reveal two primary shortcomings: nonlinearity and heteroscedasticity. A curved-shaped trend emerges, suggesting that the model inadequately captures all nonlinear relationships between total energy and the chosen variables. This indicates that the model's functional form is either misspecified or simplistic to accurately depict the underlying dynamics of energy loss during approach. Residual dispersion is not uniform throughout the output range either. At lower energy levels (nearer to touchdown), the variance in the residuals is comparatively minimal; nevertheless, when the predicted energy escalates at the beginning of approach, the dispersion of the residuals becomes significantly more pronounced. This behavior indicates heteroscedasticity, wherein the error variance depends on the output level.

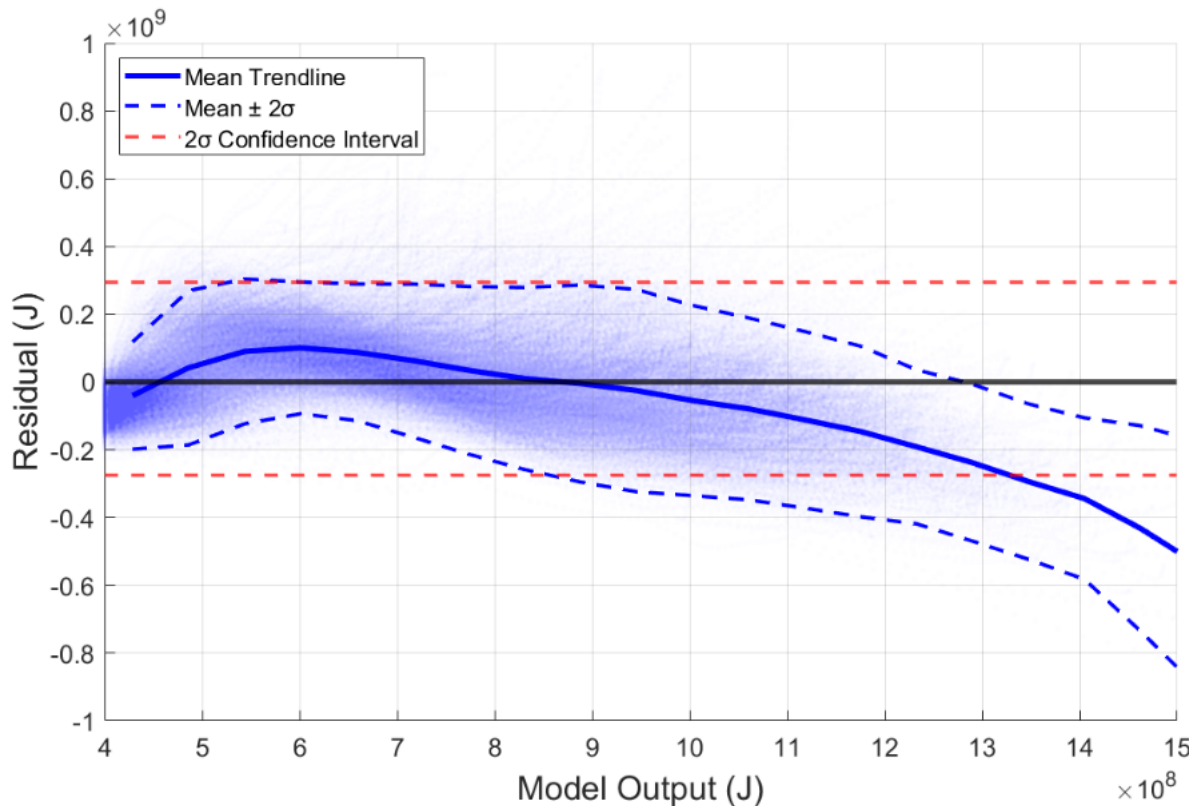


Figure 4.9 Residuals vs Model Output Plot

Via MATLAB's qqplot function, in Figure 4.10, each point signifies a residual, located based on its quantile in the sample distribution and the associated quantile of a standard normal distribution. The diagonal reference line denotes the position of points if the residuals follow a perfectly normal distribution. In this case, residuals in the figure are predominantly aligned in the central region, indicating a near-normal distribution around the mean. Significant discrepancies arise in the tails, especially with the most severe residuals at both extremes. This signifies heavier tails than the normal distribution and implies that the model sporadically generates substantial errors that are inadequately accounted for.

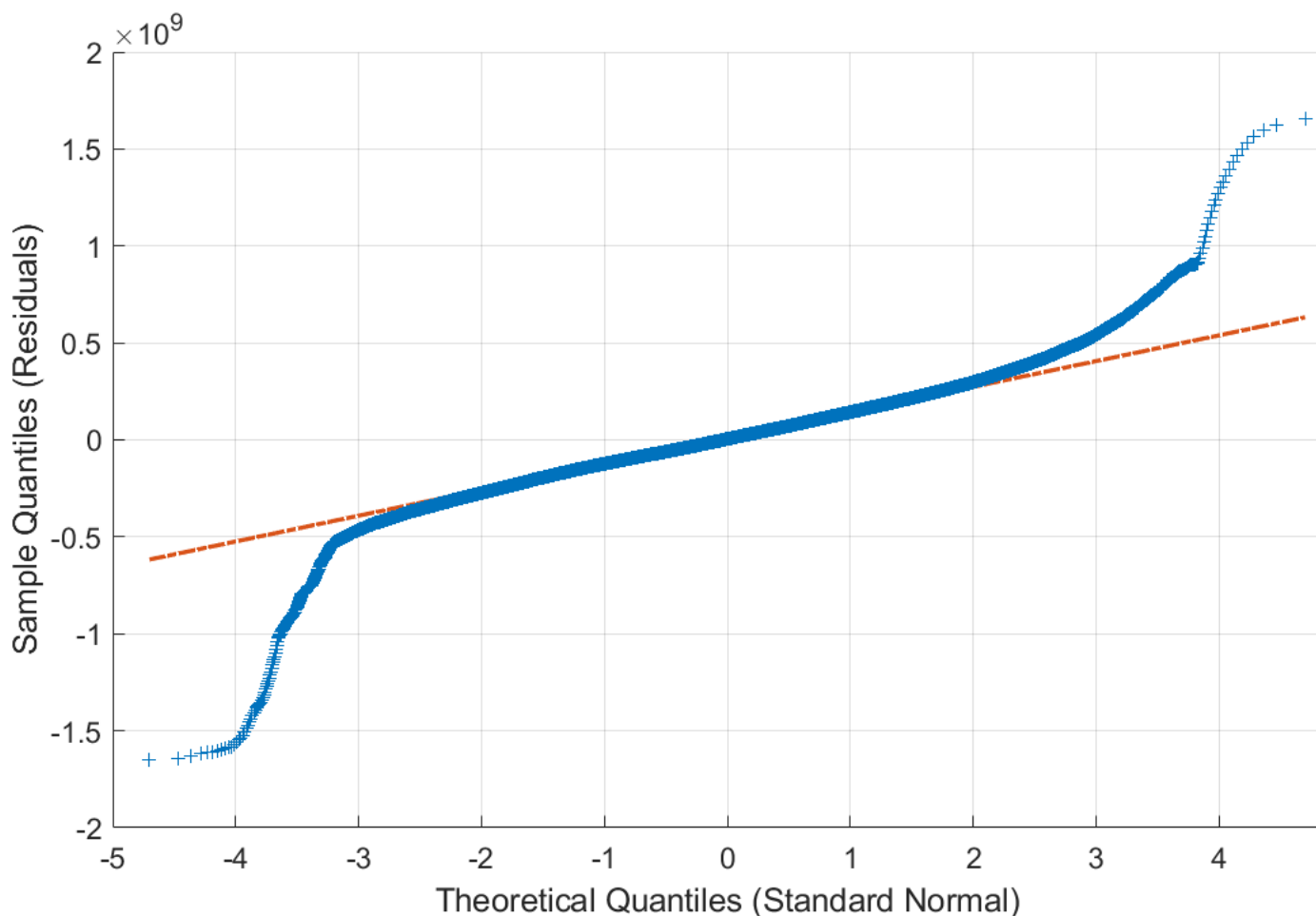


Figure 4.10 Cumulative Residuals (or Q-Q) Plot

Consequently, these findings indicate that the model might be enhanced by incorporating more explanatory variables or time-dependent elements, so enabling it to more precisely reflect the temporal patterns and variability intrinsic to approach dynamics. The existing steady-state formulation, although proficient in estimating average behavior, may neglect subtle changes that transpire throughout time. Integrating these elements may improve the model's sensitivity to sudden impacts and operational subtleties. Alternatively, shifting to a nonlinear regression framework or employing a hybrid methodology that integrates data-driven learning with physics-based constraints could enhance the model's capacity to accurately depict intricate interactions among flight parameters, thereby yielding more realistic energy forecasts.

## 4.2 Implementation

This section outlines the implementation procedure employed to execute the subset simulation framework for evaluating the probability of aerodynamic stall and loss of control in the approach phase. Subsequent to the formulation of the energy-based flight model, the simulation workflow was constructed to amalgamate real-world parameter distributions with time-stepped risk assessment during the approach phase. This part delineates the utilization of threshold energy levels to establish failure situations and the application of ranking algorithms to discern influential parameters at each time interval.

### 4.2.1 Incident Threshold Assessment

To quantitatively establish a failure threshold for LOC-I during aircraft approach, a series of flight dynamic and aerodynamic criteria was formulated based on authoritative sources, including the B747 Operations Manual at the time [27] and the quantitative framework devised by Wilborn and Foster [28]. These references highlight the significance of specific envelope excursions in forecasting LOC-I incidents and indicate that surpassing three or more essential flight dynamic parameters is a robust predictor of control loss.

Based on this guidance and reinforced by observational trends in the flight data, four specific parameters were selected as key contributors to LOC-I risk: bank angle, crosswind component (or sideslip angle if derived), angle of attack, and airspeed (or headwind component). As such, the thresholds used for these parameters were:

(4.18)

The constraints for bank and crosswind align with established literature as mentioned above. The angle of attack criterion was derived from published ranges (often 14°–16° for stall onset), whereas the speed barrier was determined by the smallest recorded value during stable flying conditions within the dataset used for this research. Modification was done on the developed model to transform these LOC-I criteria into a practical energy-based criterion. The model's input parameters ( $\alpha$ ,  $\varphi$ ,  $v$ , and  $V$ ) were methodically modified while other parameters remained the same within the dataset to ensure that the output energy trajectories throughout the approach phase could predict the expected LOC-I threshold. This was achieved by implementing controlled offsets to each parameter (for their mean trendlines), ensuring the resultant model would now depict a flight maneuvering near the LOC-I boundary on approach as shown in Figure 4.11.

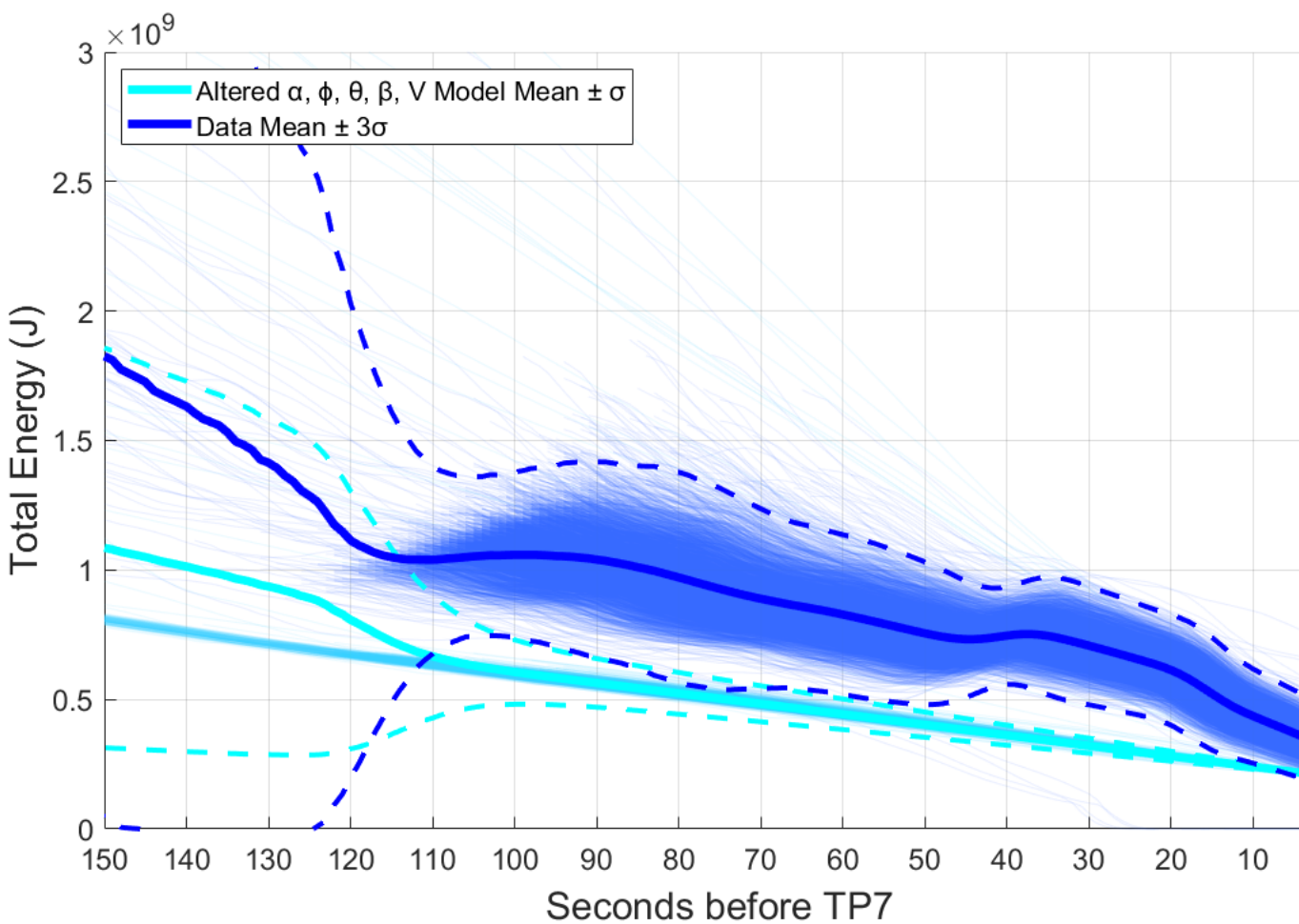


Figure 4.11 Comparison of Data and Altered Model-Based Total Energy

The outcome of this parameter modification is illustrated in Figure 4.11, where the lighter blue lines depict individual model simulations under the revised settings, and the cyan line indicates the mean  $\pm 1$  standard deviation of the adjusted model output. When compared to the actual data distribution (mean  $\pm 3\sigma$  in dark blue), it is evident that the modified scenario yields a markedly reduced energy profile, aligning with expectations during compromised flight conditions. This also yielded the lower bound (mean minus  $1\sigma$ ), which was utilized as the dynamic LOC-I energy threshold across time, depicted after linear regression in Figure 4.12.

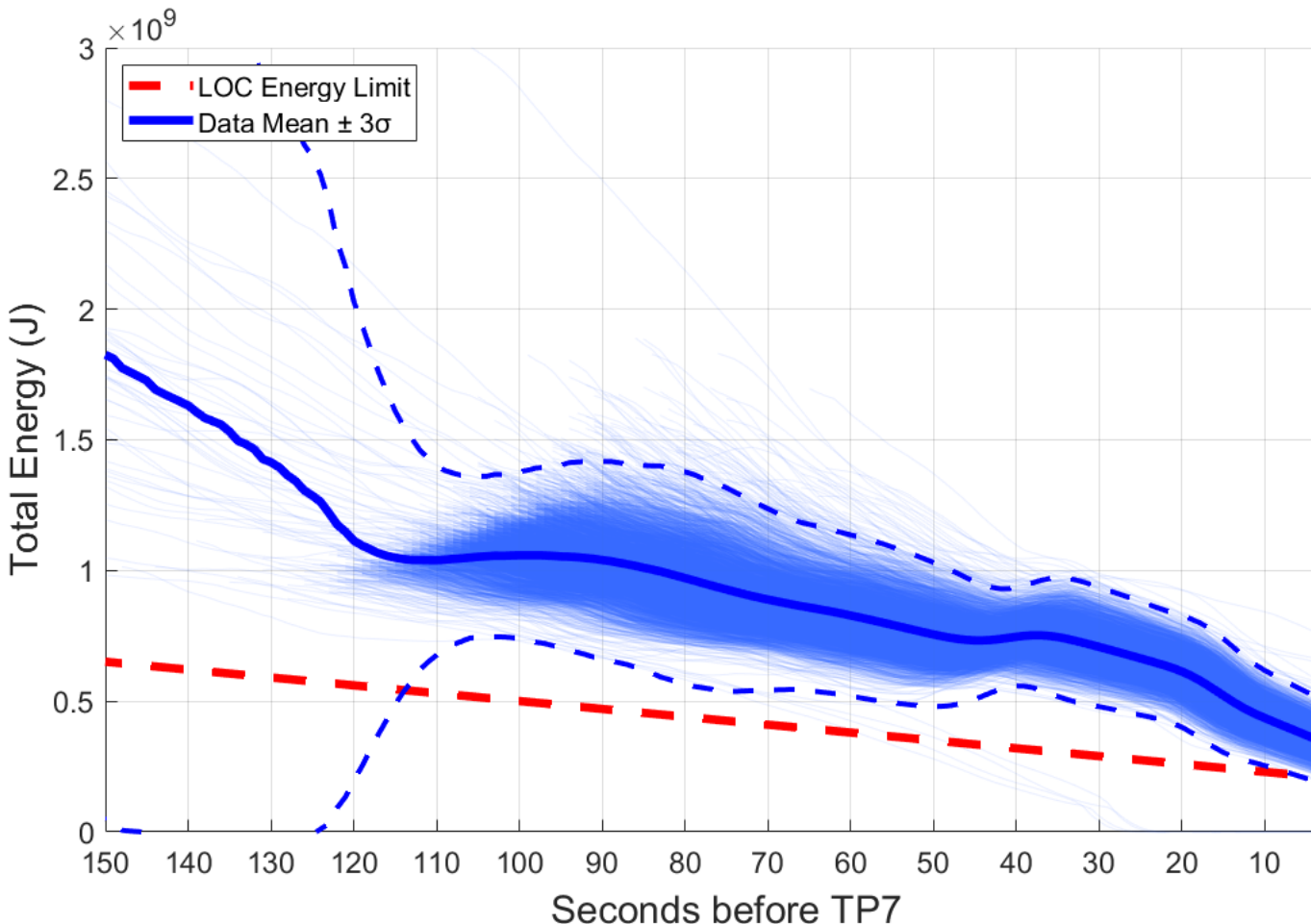


Figure 4.12 Comparison of Data-Based Total Energy and Proposed LOC-I Threshold

To establish a singular scalar failure threshold for subsequent simulation, this time-dependent energy limit was integrated over the 95-second validation interval previously utilized. The resultant area of approximately  $3.22 \times 10^9$  Js denotes the minimal cumulative energy threshold deemed essential for sustaining safe and manageable approach behavior. In this case, any flight that falls below this threshold is presumed to have entered a critical regime associated with LOC-I danger. Figure 4.13 depicts this cutoff as a red dashed vertical line overlaid on the histogram of integrated energy derived from real flight data.

It is important to recognize that a LOC-I may still transpire even when an aircraft's total energy remains below this threshold for a brief duration. Consequently, an alternate method to assess the overall risk of LOC-I involves analyzing the event not as a whole flight phase (final approach), but rather by defining its occurrence on a per-second basis, thereby closely resembling real-time analysis. The expectation is that this dilemma of accuracy will be addressed by monitoring the alteration in probability as the flight approaches touchdown. Nevertheless, to ensure a more definitive, singular value of risk about this event, it was decided to also proceed with the cumulative LOC-I threshold to quantify the overall value.

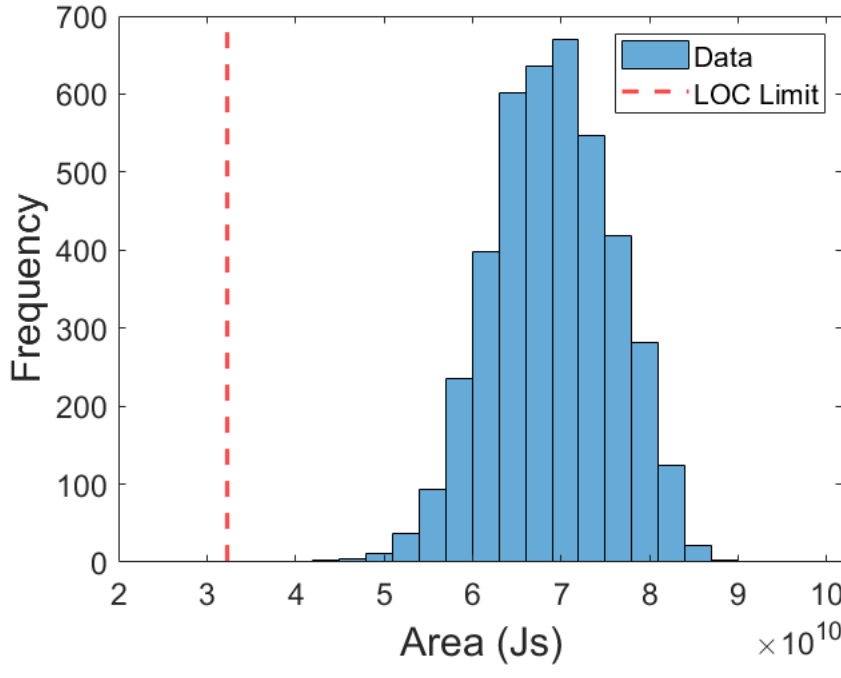


Figure 4.13 Total Energy Areas with LOC-I Threshold Depiction

#### 4.2.2 Subset Simulation Process

To assess the likelihood of a LOC-I incident during aircraft approach, a rare-event reliability method called Subset Simulation was utilized. The execution was conducted utilizing the Subset Simulation Toolbox [29] created by the Institute of Flight System Dynamics at the Technical University of Munich (TUM), which employs a MCMC method for conditional sampling. The simulation was set up using a univariate normal sample distribution derived from the statistical properties of the total energy area, represented as a normal distribution (refer to Table 4.2). The failure threshold was established using the previously determined LOC-I energy boundary (refer to Figure 4.12). Samples that fell below this threshold were deemed failures. The evaluation function (*ModelHandle*) calculates the margin of failure by deducting the threshold from each sample, whereby negative outputs indicate failure.  $5 \times 10^5$  samples were utilized, and eight MCMC subsets with a proposal distribution of (0, 0.5).

Figure 4.14 depicts the output distribution of energy area estimates across all eight subset levels produced during the subset simulation process. Each colored histogram illustrates the frequency of output samples inside a designated subset stage, commencing with Subset 1 (unconditional samples) and advancing through progressively rarer-event zones. As the simulation progresses, the output values shift to the left, signifying regions of decreased energy in subsequent conditional phases, which pertain to rare, high-risk cases, while maintaining statistical diversity within each subset level. At the last subset levels (7 and 8), the outputs converge towards zero, signifying that the simulation has attained the extreme lowest limit of the energy spectrum. This figure illustrates how the algorithm increasingly focuses sampling on the lower tail of the distribution, which corresponds to infrequent, high-risk conditions, while preserving statistical variety within each subset level.

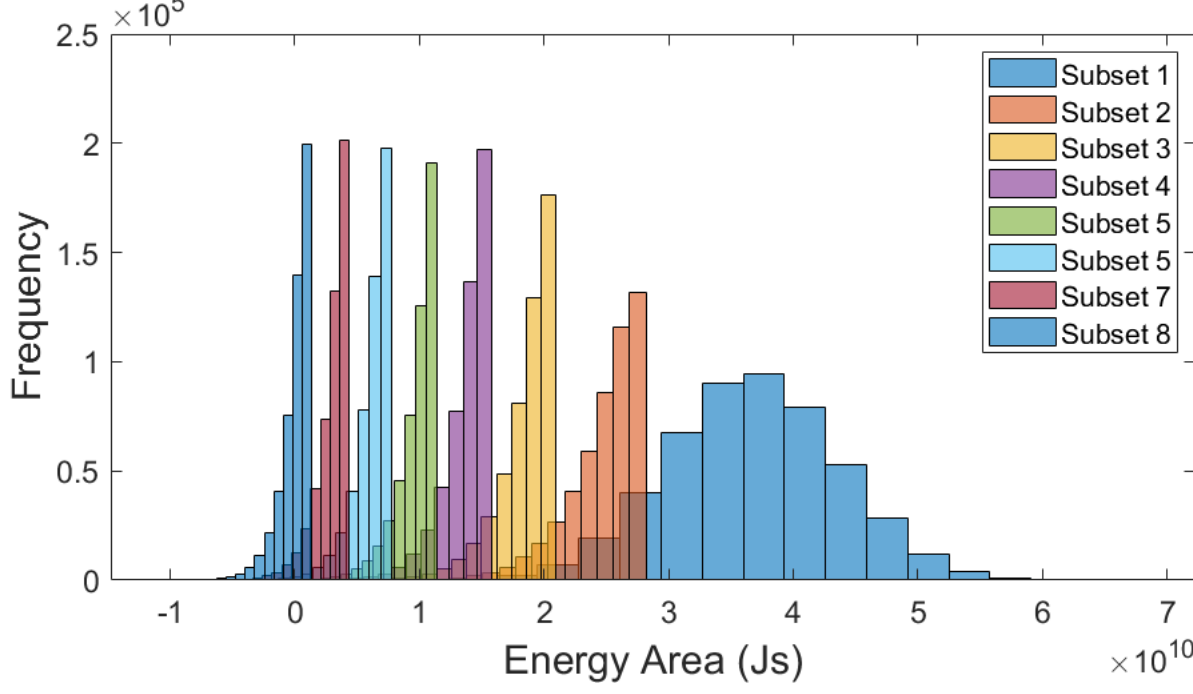


Figure 4.14 Outputs of Each Sampling Per Subset

Meanwhile, Figure 4.15 illustrates the CCDF of the total energy area, displayed across logarithmic probability intervals. This graphic facilitates direct observation of rare-event behavior in the lower tail and functions as a crucial instrument for finding energy thresholds linked to extremely low-probability outcomes. The smooth curve validates the stability and granularity of the subset simulation, thereby capturing the tail distribution with significantly better efficiency than conventional Monte Carlo sampling. In contrast to the aforementioned method that typically necessitates excessively large sample sizes to address tail events, subset simulation effectively focuses sampling efforts on the most pertinent areas, thereby achieving a more precise and computationally economical representation of the rare-event distribution.

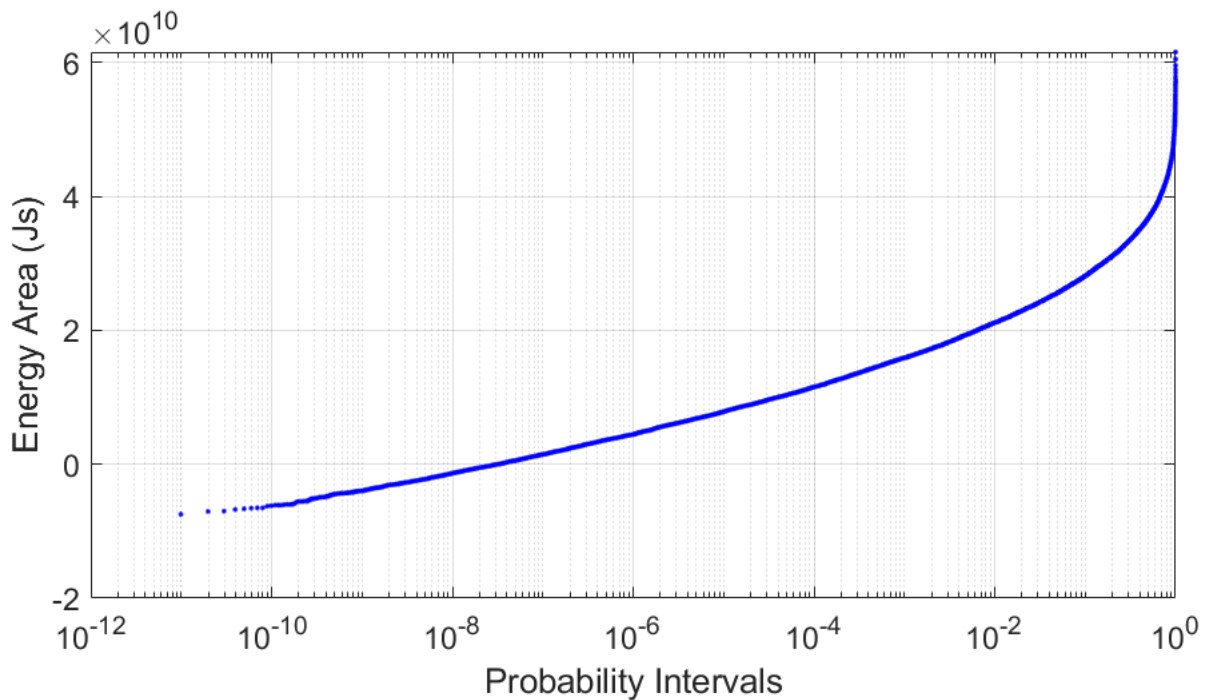


Figure 4.15 CCDF Plot for Output Energy Area

Additionally, Figure 4.16 illustrates the quantity of accepted and rejected samples at each phase of the subset simulation process. In the initial subset (Subset 1), all samples are unconditionally accepted as they are sourced directly from the original distribution. As the simulation advances to conditional subsets (Subsets 2 through 8), the quantity of approved samples steadily diminishes, whilst the quantity of rejected samples escalates. This illustrates the growing challenge of meeting the conditional criterion  $Y > b_i$  (see section 2.1.5) as the algorithm concentrates on the lower-probability tails of the distribution. The significant increase in rejections from Subset 3 onwards signifies that additional samples are necessary to ensure statistical coverage in rare-event locations.

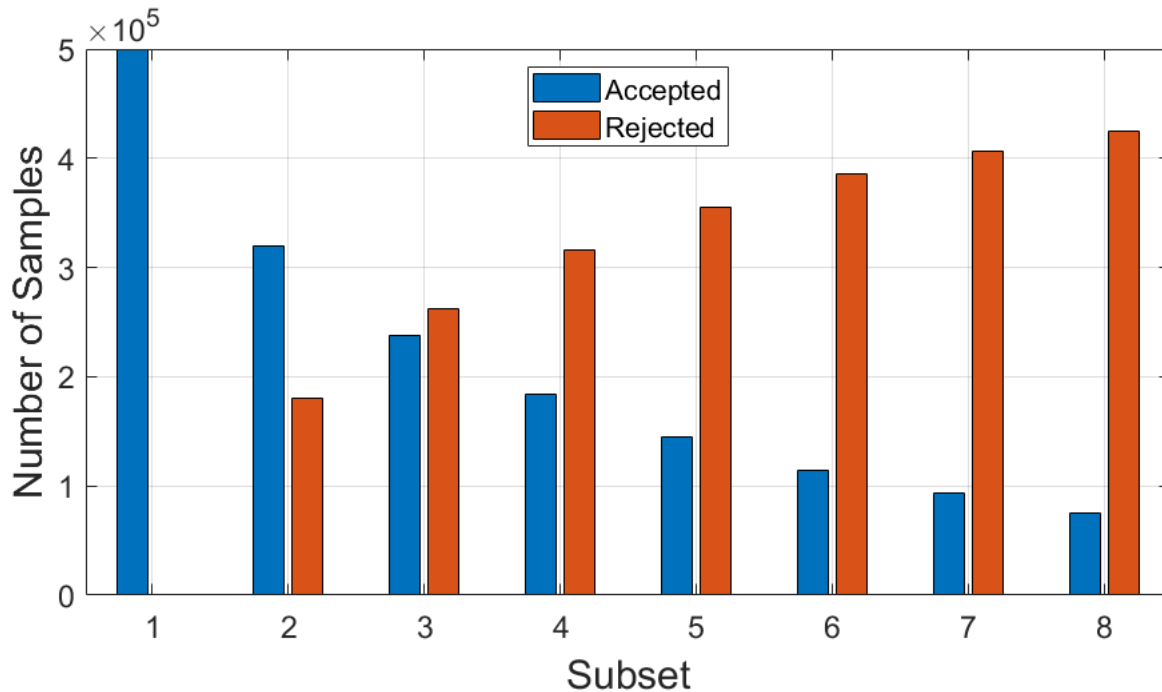


Figure 4.16 Sample Acceptances in Each Subset

This design facilitated efficient convergence to the rare-event region without the computational burden of direct Monte Carlo approaches. Employing conventional Monte Carlo sampling to achieve a precise probability estimate on a scale of  $10^{-8}$  will likely necessitate hundreds of millions of samples and might potentially require many minutes to hours. Conversely, doing a subset simulation using this toolbox takes roughly 18 seconds, resulting in a significant decrease in computational expense while maintaining a satisfactory level of accuracy. Results indicate a failure probability of  $3.57 \times 10^{-8}$ , closely aligning with the reference value of  $3.56 \times 10^{-8}$ , derived from the analytical cumulative distribution function (normcdf). This also signifies an enhancement in accuracy relative to a prior 10,000-sample execution, which yielded a marginally underestimated outcome of  $2.80 \times 10^{-8}$ . Therefore, increased sample sizes enable the simulation to investigate the failure tail region more thoroughly, improving the estimation.

It is important to highlight that although the toolbox facilitates the integration of a comprehensive model as the foundation for sampling, this was not executed in this instance. The model, as delineated in Section 4.1, is employed to ascertain the present total energy at a given moment. This contrasts with the formulation of the LOC-I threshold, which is established by a cumulative and fixed energy amount based on four criteria, for 95 seconds of flight, necessitating an additional step of numerical integration to align with the setting. The pre-computed energy distribution is utilized directly, which is more effective for estimating failure probability as it eliminates the necessity of propagating uncertainty through the model during sampling. This leads to expedited simulations as the energy values do not require recalculation from parameter inputs. Nonetheless, the drawback is that sensitivity analysis becomes increasingly manual. Although this introduces extra manual effort, it maintains the fundamental statistical integrity of the procedure and will be rigorously addressed in Section 4.2.4.

#### 4.2.3 Iterative Per-Second Simulation

To augment the overall failure probability calculation, an alternate methodology was employed wherein the subset simulation procedure is iteratively repeated at each second throughout the approach phase. This method generates a time-resolved failure probability profile utilizing distributions of flight parameters obtained from recorded data. This method dynamically reconstructs a sample distribution every second, utilizing the immediate statistical characteristics of the input values. All parameters are presumed to be normally distributed at each second, depending on their current mean and standard deviation throughout the phase. The time-varying distribution is then utilized to calculate the instantaneous energy level using the aircraft model outlined in Section 4.1.

The simulation was again conducted utilizing the same Toolbox, set with a smaller conditional probability of 0.001,  $1 \times 10^5$  samples per time step, and an adaptive MCMC sampling technique. The evaluation function was altered to dynamically compute the energy at each second, utilizing the sampled inputs and the energy rate, which was integrated forward with a time step of 1 second from the propagated value at the preceding time step. At each second, the failure probability is computed using a variable

number of subsets (from 9 to 2) and the rate of change of the acceptance ratio. This method, albeit more computationally demanding than a singular simulation, provides enhanced temporal resolution of risk progression and facilitates future exploration of time-specific hazard intervals. The runtime of each iteration is inversely proportional to the magnitude of  $P_F$ , which took around 6 hours and 24 minutes to complete all 95 seconds of flight.

Figure 4.18 juxtaposes the output distributions of total energy at two distinct intervals during the iterative subset simulation. The graphic illustrates the degree to which the simulation investigates the failure domain across various runtime situations. This visual comparison highlights the trade-off between computing effort and statistical coverage: an increase in subgroups prolongs runtime while markedly enhancing accuracy by focusing on the extremes of the energy distribution. Consequently, it underscores the necessity of adaptively calibrating the number of subgroups at each time step to ensure both efficiency and reliability in assessing time-resolved risks.

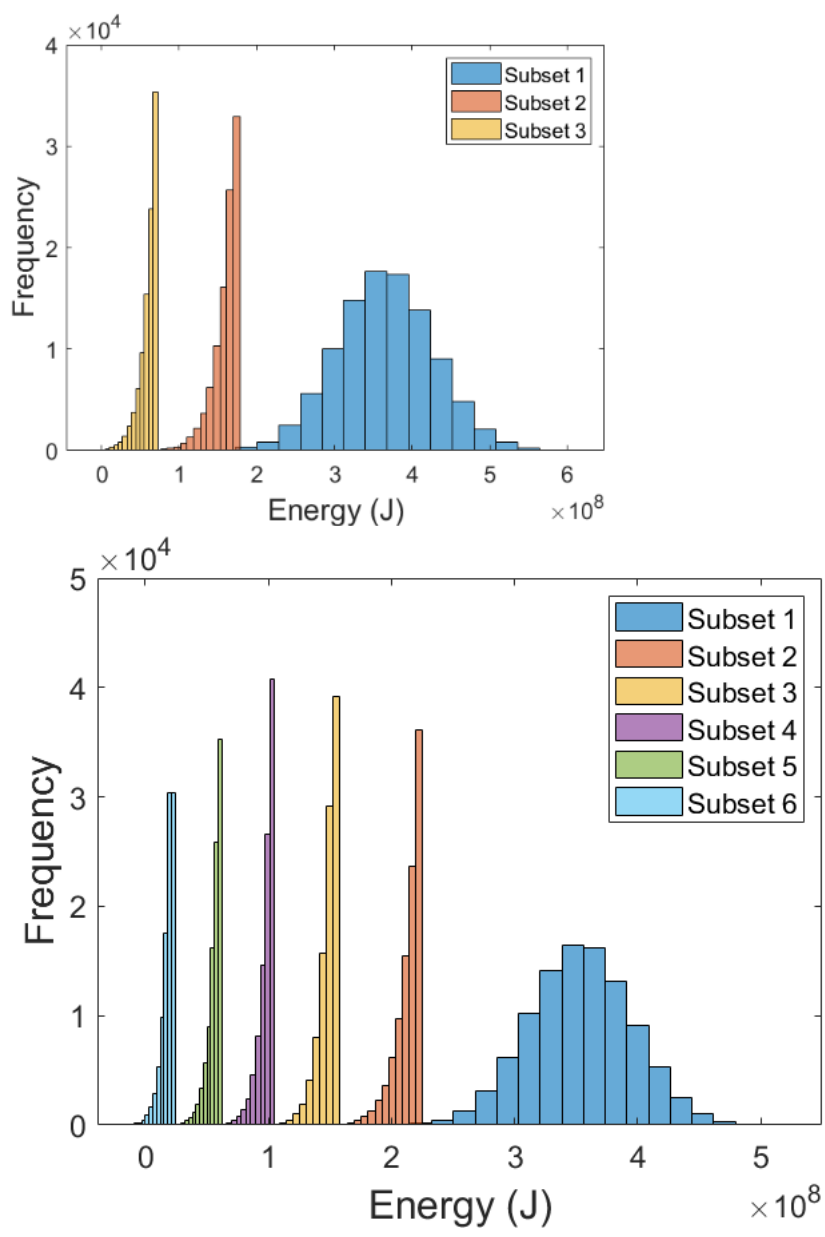


Figure 4.17 Output Plots at  $T = 25$  s (left) and  $T = 50$  s (right)

Figure 4.17 then displays complementary cumulative distribution function (CCDF) plots of total energy at two distinct time intervals during the subset simulation procedure. The left graph ( $T = 25$  s) has a more gradual and smoother curvature, suggesting that the variation in energy levels is rather small at this stage of the descent. Conversely, the right plot ( $T = 50$  s) indicates a more pronounced increase in energy towards the upper tail, implying heightened variability and potentially greater sensitivity to parameter fluctuations as the aircraft descends further.

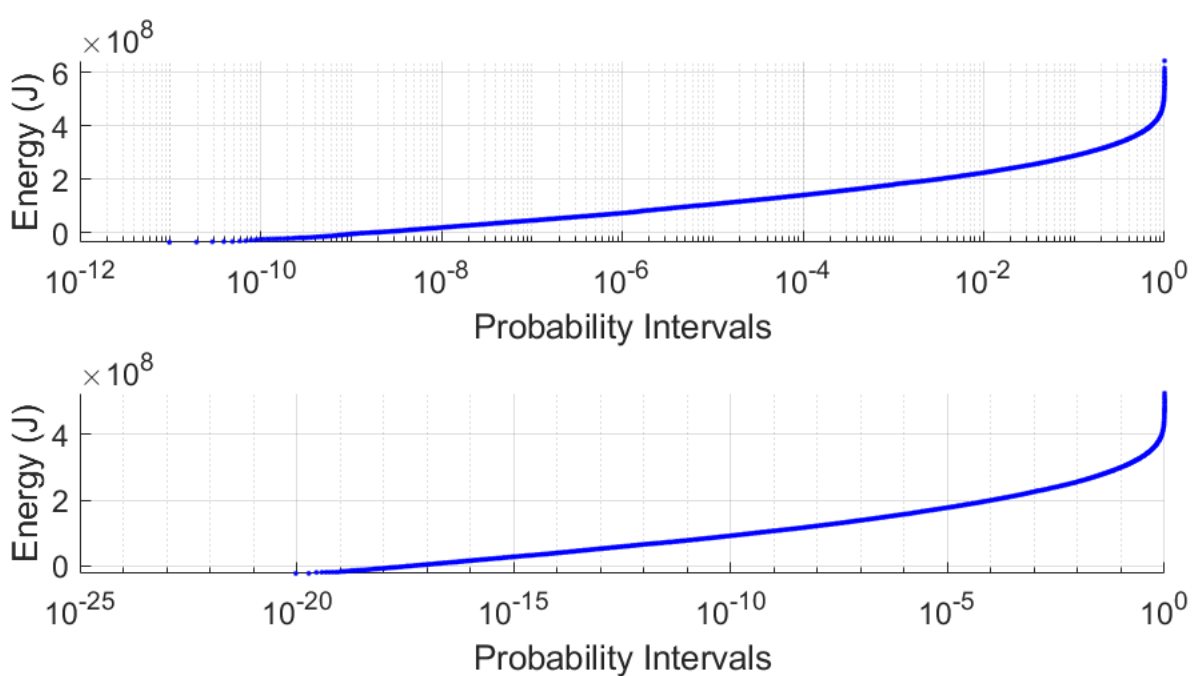


Figure 4.18 CCDF Plots for  $T = 25\text{ s}$  (bottom) and  $T = 50\text{ s}$  (top)

Figure 4.19 juxtaposes the quantities of accepted and rejected samples at each subset level across two temporal intervals. The left plot exhibits a higher quantity of subset levels, with an increased number of accepted samples in the initial stages, followed by a progressive decrease as the threshold becomes more stringent. This signifies a successful in-depth investigation into the failure domain, supported by a well-distributed acceptance rate across levels. In contrast, the right plot, restricted to merely three subgroup levels, exhibits a more pronounced decline in acceptances and an elevated rejection rate at the outset of the process.

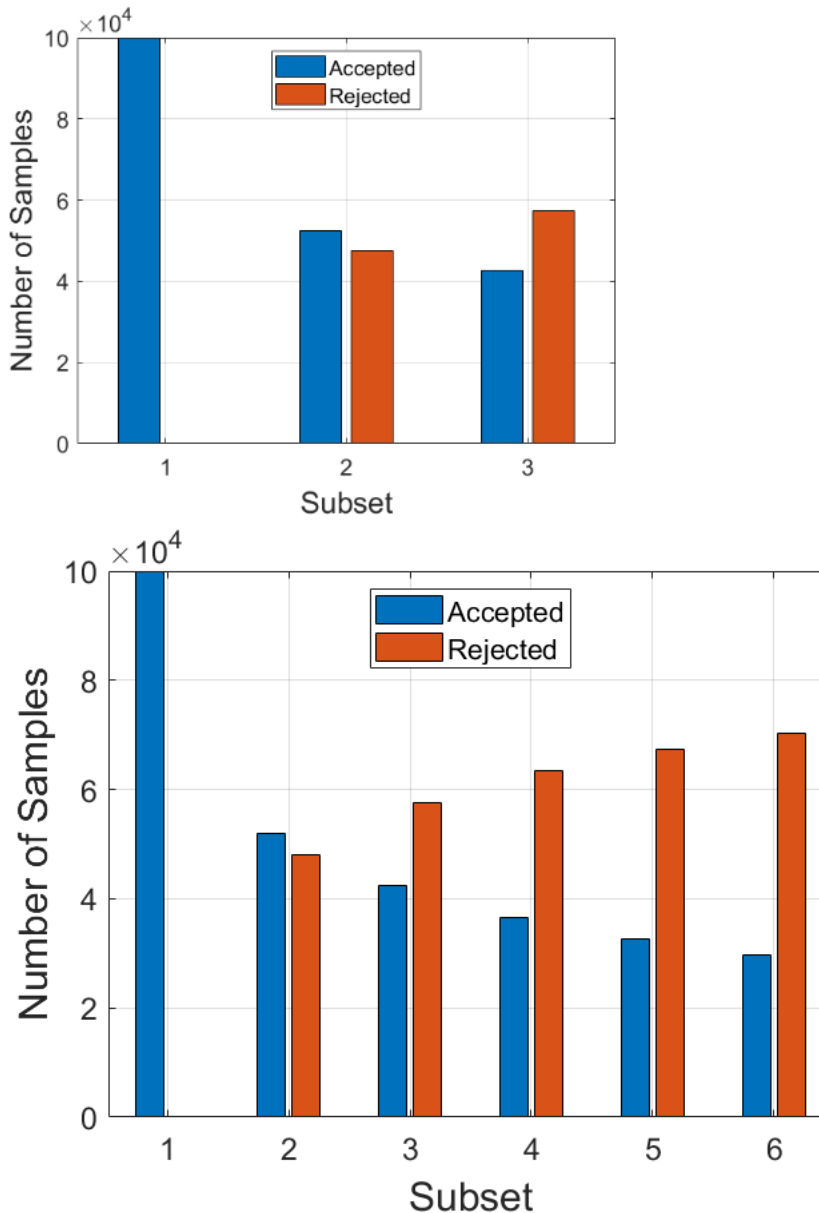


Figure 4.19 Acceptance of Samples for  $T = 25\text{ s}$  (left) and  $T = 50\text{ s}$  (right)

#### 4.2.4 Manual Sensitivity Analysis

A sensitivity analysis is performed to ascertain the impact of individual model input parameters on the estimated probability of failure,  $P(F)$ . The analysis was conducted manually by carefully adjusting each parameter by a fixed proportional increment (10% increase), recalculating the total energy progression using the model, producing a

new threshold curve, and subsequently re-executing the subset simulation to assess the resultant change in P(F).

This method offers a clearer and more interpretable means to assess the sensitivity of the model output to variations in each input variable. With a uniform percentage increase to isolate the effect of each parameter under consistent settings, it facilitates meaningful comparisons of relative impact. This method facilitates the discovery of parameters that have either stabilizing or destabilizing influences on the overall energy trajectory, and thus, on the likelihood of failure. Therefore, a foundation for comprehending the impact of parameters is established before engaging in more intricate or automated investigations.

Additionally, it is important to observe that while the toolbox offers an automated approach for doing sensitivity analysis, the conditions related to the simplification of the simulation and the absence of integration with the actual model precluded the utilization of this option for estimating the overall likelihood. Nevertheless, adopting an alternate analysis that concentrates on the individual seconds of the approach phase mitigates the previously identified limitation, hence facilitating the automated analysis through the toolbox. For example, Figure 4.20 exemplifies the alteration implemented to the angle of attack. The initial mean (black) was elevated to a new mean trajectory (green) while preserving the overall trend of the data. Comparable modifications were implemented on all other parameters in the incident model.

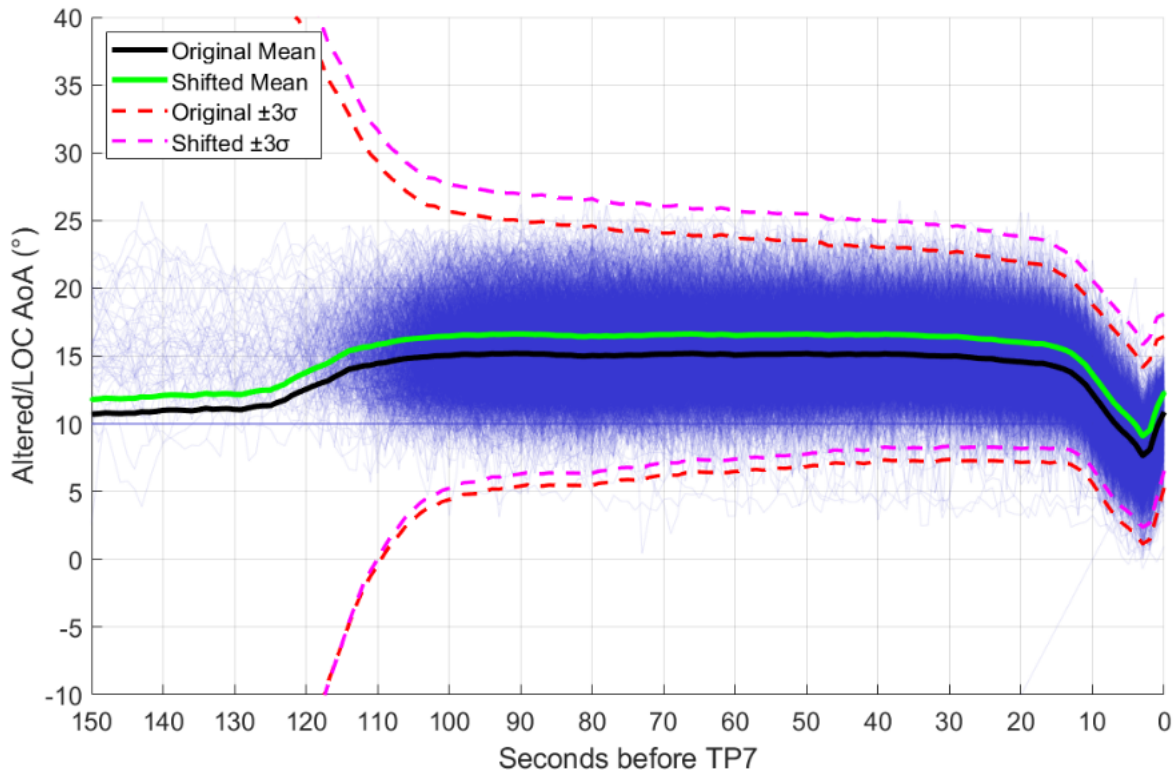


Figure 4.20 A 10% Increase in Threshold for Angle of Attack Data

Figure 4.21 then illustrates how P(F) responds to each parameter change, shown as a bar plot. This sensitivity analysis method highlights which parameters have the greatest influence on the model's prediction of stall or LOC-I risk during approach by inspecting the magnitude change.

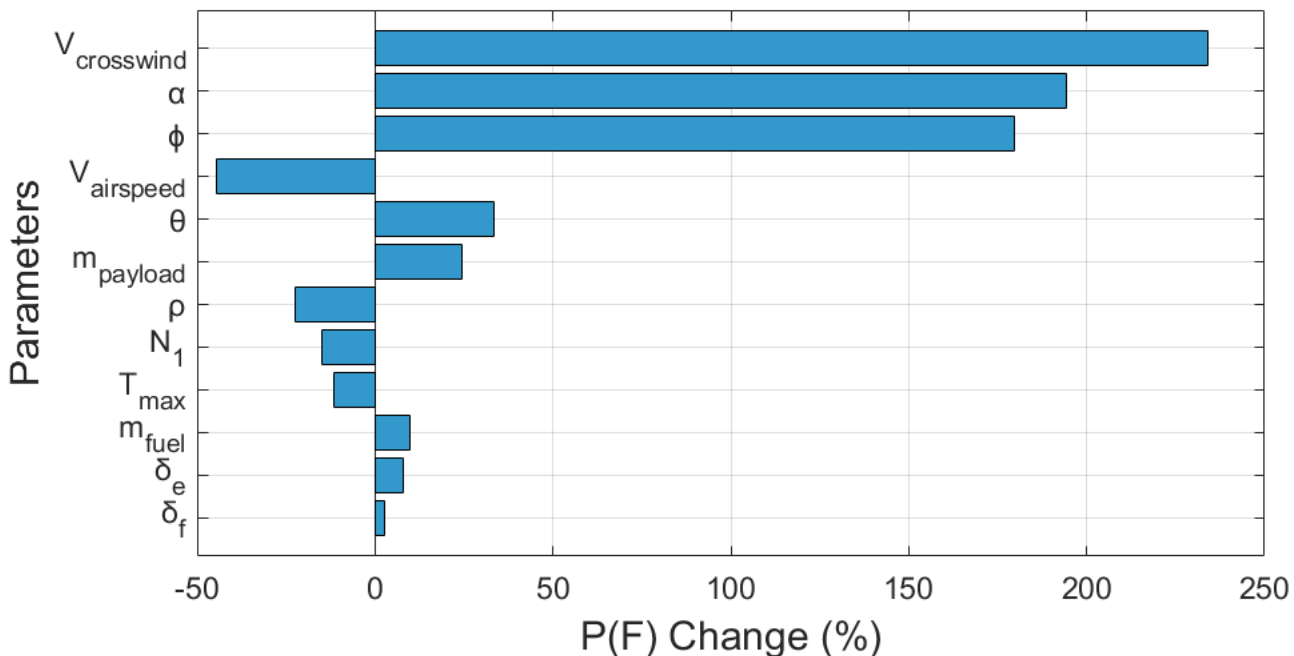


Figure 4.21 Graphical Comparison in P(F) Change by 10% Increase of Parameters

Table 4.3 ranks input parameters based on how a 10% increase in each parameter affects P(F). Crosswind, angle of attack, and bank angle show the strongest influence, significantly raising the likelihood of failure and highlighting their critical role in aircraft stability during approach. In contrast, parameters like airspeed and air density reduce failure probability, suggesting a stabilizing effect on the energy profile. Other inputs, such as thrust setting, elevator deflection, fuel, and flap position, show smaller impacts.

Table 4.3 Ranking and P(F) Change from 10% Parameter Increase

Rank	Parameter	$\Delta P(F) (%)$	Rank	Parameter	$\Delta P(F) (%)$
1	Crosswind	+233.99%	7	Air Density	-22.52%
2	AoA	+194.87%	8	$N_1$	-14.91%
3	Bank Angle	+179.75%	9	Max Thrust	-11.61%

4	Airspeed	-44.49%	10	Fuel	+9.92%
5	Pitch Angle	+33.34%	11	Elevators	+8.08%
6	Payload	+24.59%	12	Flaps	+2.78%

Considering these nonlinear, coupled relationships (illustrated in Equations 4.2 to 4.16), it is anticipated that equivalent percentage variations in each parameter will yield distinct energy output profiles and magnitudes, leading to disproportionate shifts in failure probability  $P(F)$  when subjected to subset simulation. As a result, the effects were quantified, and parameters were ranked according to their influence on the absolute magnitude of  $\Delta P(F)$ . A more profound interpretation of parameter significance will be postponed to a later section (refer to Section 5.2), where parameters will be categorized for more meaningful comparisons.

#### 4.2.5 Toolbox-Assisted Sensitivity Analysis

An automated sensitivity analysis was also performed using the Toolbox to augment the manual approach during the execution of the per-second failure probability quantification. Unlike the previous configuration that employed precomputed and altered energy distributions to circumvent the tedious recalculation through the energy model, this method integrates the model directly into the simulation loop.

The toolbox conducts a sensitivity analysis by assessing the impact of each input parameter on the probability of failure  $P(F)$  using the generated MCMC samples and their statistical contribution to the failure set. It specifically assesses conditional and marginal distributions inside parameter bins, superimposing the global distribution with the conditional distribution given failure. The sensitivity measure is determined by the divergence between these distributions spanning intervals  $j$ , as specified by:

(4.19)

Figures 4.22 and 4.23 illustrate the example output for  $\alpha$  at two specific time intervals to showcase the methodology behind the toolbox's rankings. In both subfigures, the left histogram displays the prior distribution in green, with the matching PDF overlay in red on the black, a priori curve. The right-hand histogram, which is more significant for sensitivity, illustrates the conditional in blue, with its divergence from the previous. The height and width of the blue bars signify the extent to which failures aggregate within certain parameter ranges.

At 25 s, the wider and more pronounced blue distribution relative to 50 s indicates that the angle of attack becomes progressively more critical in the advancement toward a failure outcome for the former period. For the former, the conditional samples exhibit a moderate upward shift, suggesting that elevated angle of attack values are more closely correlated with outcomes approaching the failure threshold during this initial phase of descent. Conversely, at  $T = 50$  s, the divergence intensifies, with the conditional distribution displaying a more prominent skew toward the upper tail. This indicates the growing importance of angle of attack as the aircraft approaches touchdown, implying its heightened influence in reducing total energy below the specified threshold.

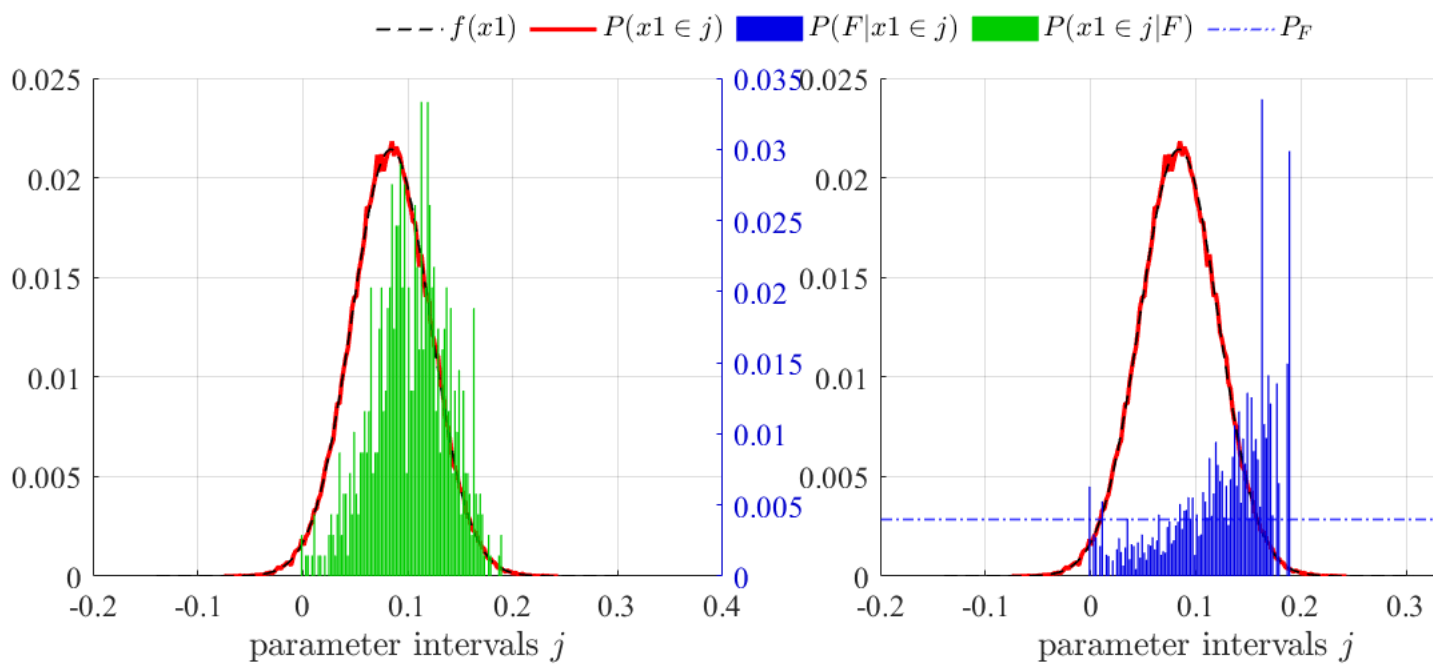


Figure 4.22 Sensitivity Plot for Angle of Attack at  $T = 25$  s

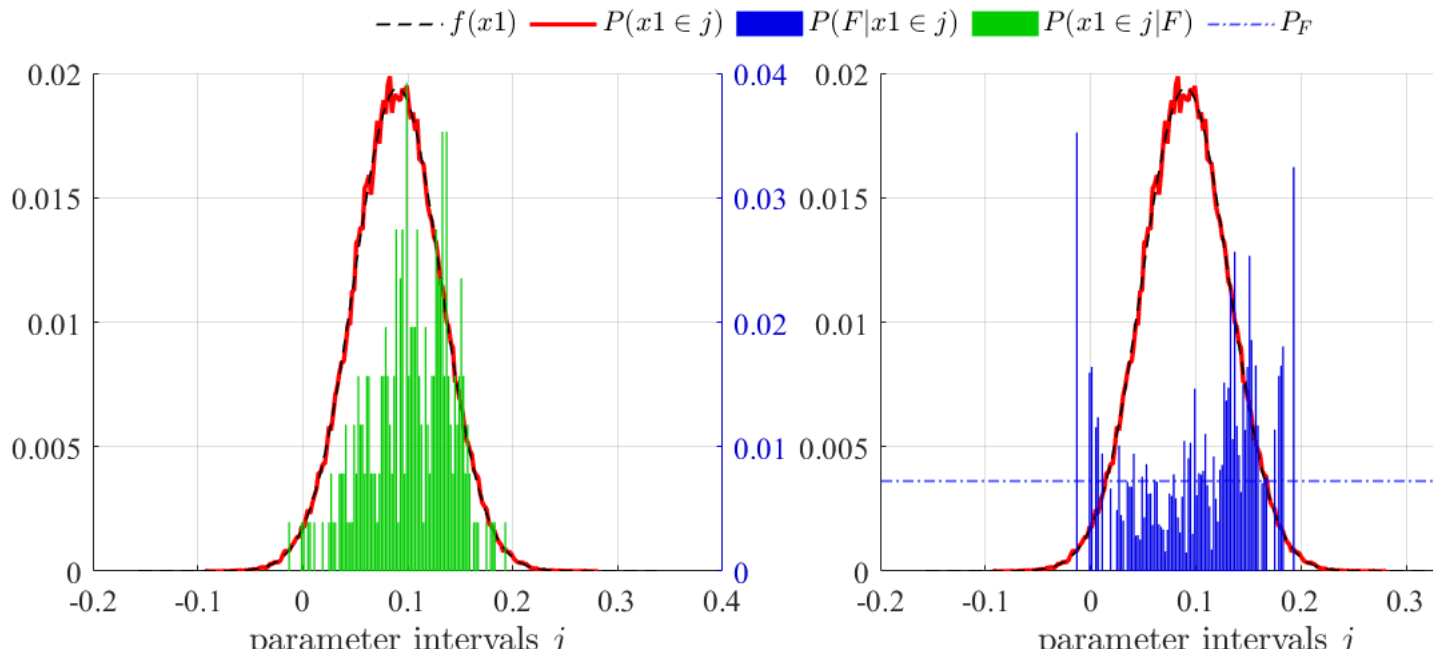


Figure 4.23 Sensitivity Plot for Angle of Attack at  $T = 50$  s

Figure 4.24 depicts the temporal evolution of sensitivity ratings for all nine input parameters during the 101-second approach window. Each line monitors the impact of a parameter on the probability of failure  $P(F)$  at each time interval. Significant increases in a parameter's score denote instances when it exerts a more substantial influence on driving the system towards failure, whilst stable regions imply intervals of negligible impact. It ascribes the fluidity of flight risk, indicating that the parameter influence fluctuates based on the aircraft's flying state.

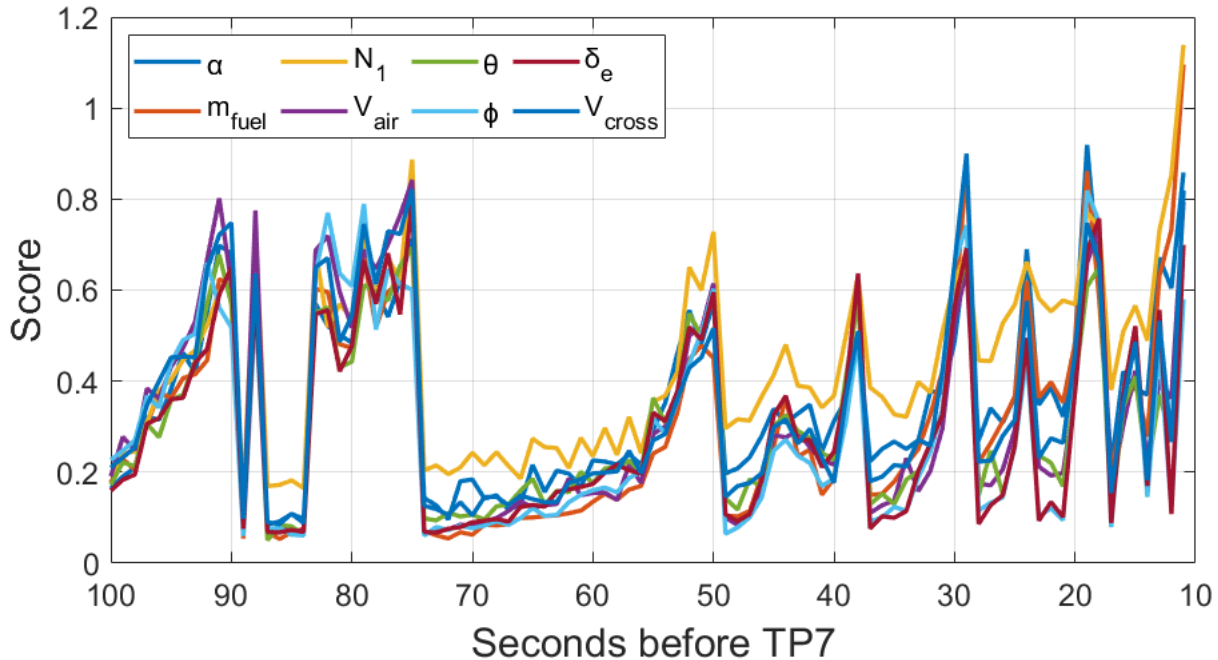


Figure 4.24 Progression of Sensitivity Scores on Final Approach

Figure 4.25 displays the cumulative sensitivity scores for all input parameters, derived via toolbox-assisted analysis. Each bar signifies the cumulative impact of a certain parameter, consolidated over time, illustrating its overall contribution to the simulated failure probability. The plot delineates a distinct hierarchy of parameter significance based on their cumulative impact, presenting a more comprehensive perspective than Figure 4.24.

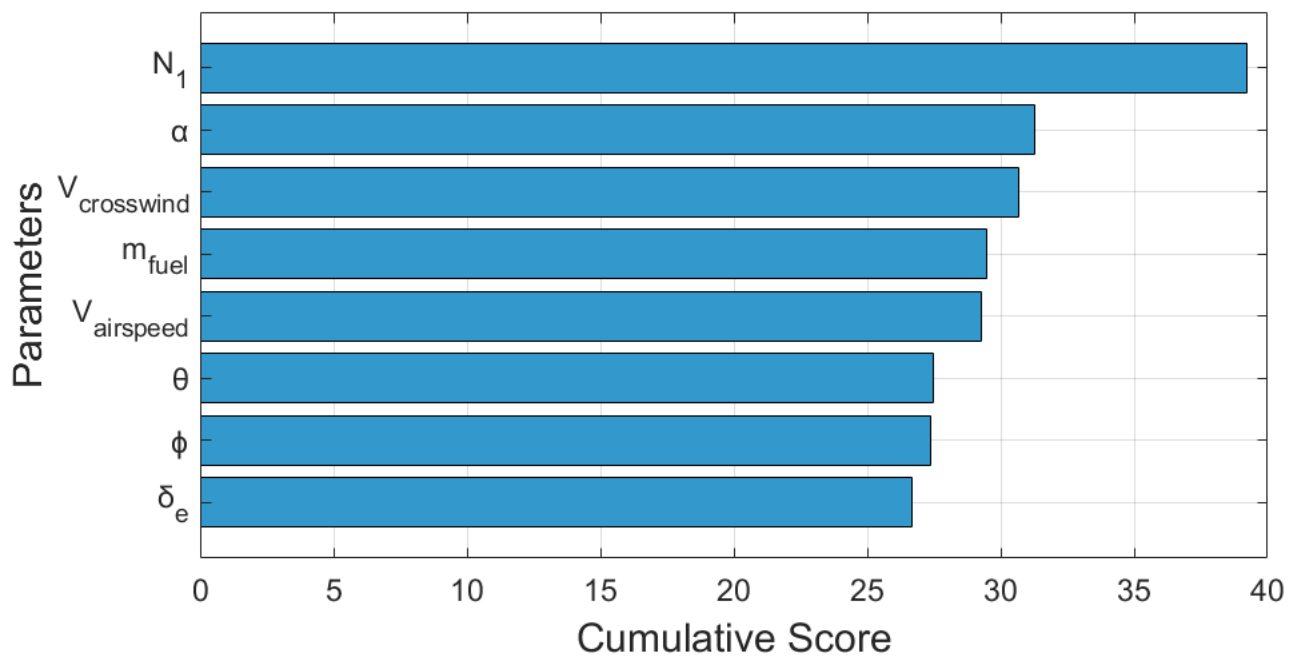


Figure 4.25 Cumulative Score Plot from Toolbox-Assisted Sensitivity Analysis

Table 4.4 enumerates the nine input parameters in descending order based on their cumulative sensitivity ratings during the entire approach length. These rankings indicate the overall impact of each parameter on failure probability, as assessed by the divergence between conditional and prior distributions at all time intervals. Parameters including angle of attack, vertical speed, and bank angle are crucial, signifying their significant and enduring influence on the aircraft's energy profile and related risk. Parameters of moderate rank, such as crosswind and elevator deflection, exhibit a moderate impact, whilst others, like flap position and  $N_1$  have a negligible contribution throughout the simulation period.

Table 4.4 ranks input parameters based on their cumulative sensitivity ratings obtained from the toolbox-assisted subset simulation. In contrast to physical intuition, the  $N_1$  fan speed is the highest, followed by the angle of attack and crosswind. Parameters of intermediate rank, including fuel mass, airspeed, and pitch angle, exert a modest influence, whereas control-related variables such as elevator deflection rank lower.

Table 4.4 Sensitivity Rankings of Parameters Based on Cumulative Score

Rank	Parameter	$\Sigma$ Score	Rank	Parameter	$\Sigma$ Score
1	$N_1$	39.24	5	Airspeed	29.30
2	AoA	31.29	6	Pitch Angle	27.49
3	Crosswind	30.67	7	Bank Angle	27.38
4	Fuel	29.49	8	Elevators	26.66

Note that this simulation method unavoidably limits sensitivity analysis to parameters that are directly input into the total energy model (see Equation 4.17). Using the toolbox meant not monitoring for intermediate or derived variables like lift coefficient or other force components. The values are computed internally within the model and are neither disrupted nor sampled during simulation; hence, their sensitivity cannot be assessed using the toolbox's inherent processes.

Also, the ranking of  $N_1$  in the toolbox output necessitates an interpretation. While thrust setting aids in energy preservation, it is generally not a principal catalyst for stall or instability. Its superior ranking in the toolbox is likely attributable to its extensive statistical variance (see Table 5.3), which exaggerates its perceived significance in the MCMC sampling. This statistical bias represents a constraint of the toolbox technique, which fails to adjust for variation or establish causality.

## Chapter 5

### Results and Analysis

#### 5.1 Simulation Results

This section delineates the results of the time-resolved subset simulation conducted over a 95-second approach segment for each permutation of the four criteria. The results from the ranking function and the comprehensive toolbox-assisted sensitivity analysis are presented, along with cross-comparisons of parameter impact via individual perturbation and scoring-based techniques.

##### 5.1.1 Probability Types

Before examining individual or combined scenarios of parameter threshold exceedance resulting in LOC-I, it is essential to first delineate the types of probabilities addressed in this study. These definitions establish the basis for all ensuing risk estimates, encompassing the baseline (full criteria) scenario and other (partial criteria) scenarios. In assessing the risk associated with the threshold exceedance of the four flight characteristics designated as criteria (see Section 4.2.1), three unique categories of probabilities are identified:

1. Criteria Occurrence or  $P$  (Criteria)

This is the likelihood that one or more parameter conditions are satisfied during the approach phase. Each parameter's time series is integrated over the specified approach window (95 s), and a threshold is calculated as the product of the parameter's critical limit (such as in Figure 5.1, where AoA is altered) and the integration duration. A flight is designated as meeting a criterion if the cumulative value passes this threshold in Figure 5.2.

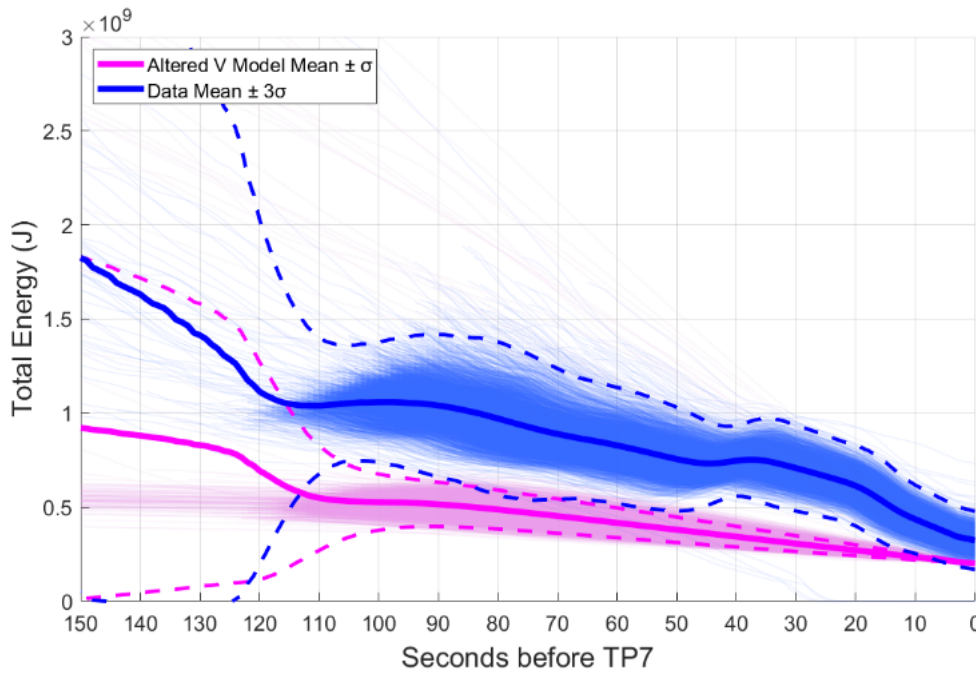


Figure 5.1 Model Energy Progression with Altered Airspeed

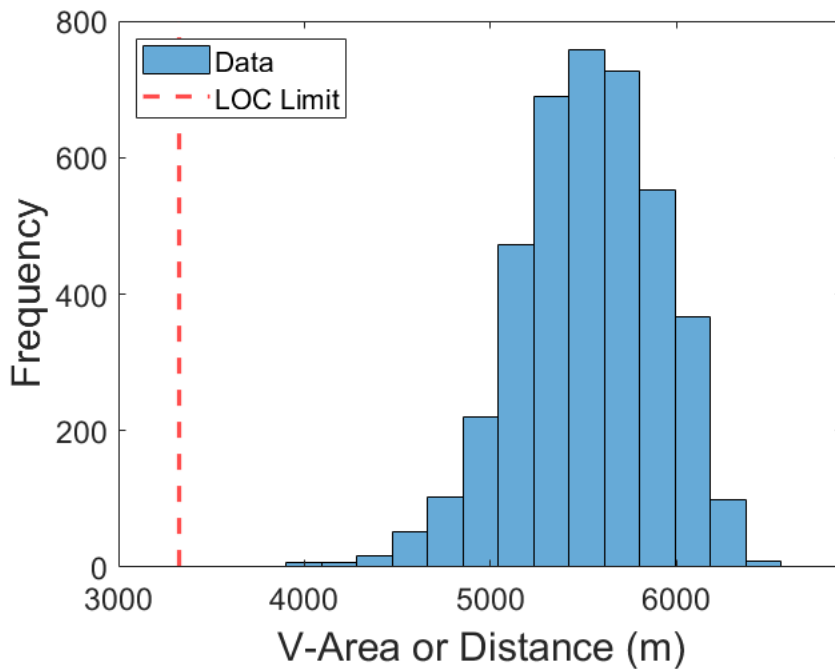
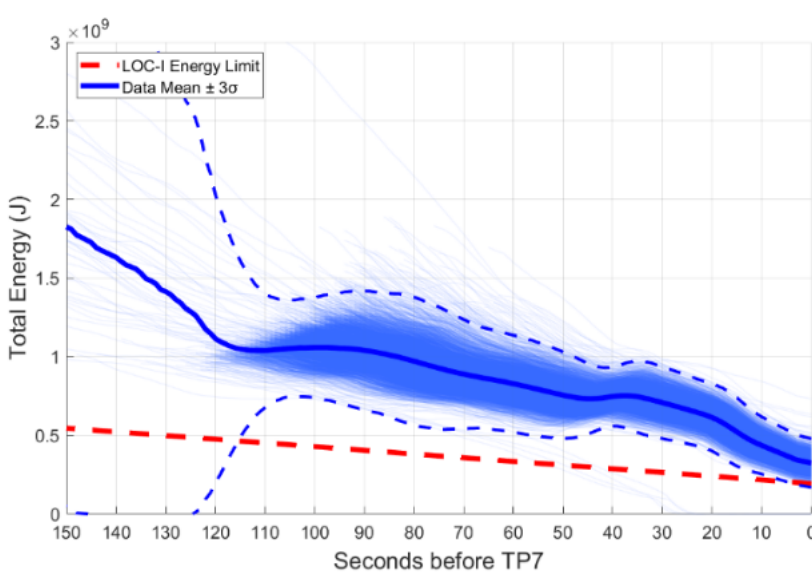


Figure 5.2 Airspeed Criteria Threshold for Total Energy Progression (left) and for Parameter Area (right)

#### 1. Conditional LOC-I or P (LOC-I | Criteria)

This case is the likelihood of a LOC-I event occurring, contingent upon the fulfillment of one or more criteria. The energy area threshold method computes this by modifying the inputs for a specific scenario to represent LOC-I conditions given one or more criteria being fulfilled, followed by a recalculation of the total energy progression. The lower limit of this energy profile is utilized as the 'LOC-I threshold' in the subset simulation, yielding an estimate of the conditional failure probability for that criterion.

#### 1. Joint LOC-I & Criteria or P (Scenario) or P (LOC-I and Criteria)

This represents the total probability of interest: the likelihood that a criterion is satisfied and that a LOC-I ensues consequently. The calculation is derived from the multiplication of the scenario likelihood and the associated conditional LOC-I probability as

(5.1)

### 5.1.2 Risk Scenarios

Table 5.1 delineates the computed probabilities for all 15 non-empty combinations of the criteria parameters (airspeed, angle of attack, crosswind, and bank angle) being surpassed during the approach phase, alongside the consequent LOC-I risk. Every scenario encompasses the three previously described forms of probability in Section 5.1.1.

Table 5.1 List of Probabilities for LOC-I Scenarios

#### Criterion P (Criteria) P (LOC-I | Criteria) P (Scenario)

In single-parameter scenarios, bank angle and sideslip are the predominant factors influencing joint-criteria LOC-I probability. The heightened hazards arise not only from elevated conditional probabilities, but from the increased frequency with which these parameters surpass their thresholds in the approach data. Conversely, infractions in airspeed and angle of attack limitations are less frequent, hence constraining their overall risk contribution despite similar conditional LOC-I probability.

Combinations of several parameters do not result in increased joint probability; rather, they significantly diminish. This arises from the infrequency of several concurrent exceedances and the non-linear scaling of the LOC-I model's response with further parameter violations. Once critical flight dynamics are disrupted, the introduction of additional violated parameters does not substantially affect the system's failure response (within the framework of the energy-based model).

A significant trend is the recurrent occurrence of bank angle and sideslip among the foremost danger situations. These metrics exhibit greater susceptibility to natural variability during the final approach due to lateral wind components, rudder application, or corrective movements in proximity to the ground. In contrast to airspeed or angle of attack, which are stringently controlled via Autoland protocols, bank and sideslip frequently exhibit active pilot inputs and atmospheric perturbations, resulting in more regular deviations outside established safety parameters.

This pattern is also evident in real-world situations, albeit not an identical replication of the studied event of interest. China Airlines Flight 605 [30], a Boeing 747-409B had significant crosswind and tailwind conditions when approaching Kai Tak Airport (Hong Kong), leading to a forceful landing and subsequent runway overrun. Other historical incidents, although differing in altitude and aircraft type, also substantiate the significance of these characteristics in LOC-I scenarios. American Eagle Flight 4184 [31] and Comair Flight 3272 [32] both experienced roll and attitude deviations due to icing during descent or approach. In both instances, the aircraft entered unrecoverable banks and elevated angles of attack just before LOC-I, situations that directly align with the criteria established in this study. While the principal cause of these accidents was atmospheric (icing), the characteristics preceding loss of control correspond with the criteria proposed for a LOC-I to occur.

### 5.1.3 Dynamic Failure Probability

With the help of the per-second simulation approach, a time-dependent failure probability curve  $P_F(t)$  can be developed, and is illustrated in Figure 5.4. The black curve demonstrates a swift decline in failure probability as the aircraft approaches touchdown, consistent with the logical assumption that risk decreases as landing occurs, where the system is generally more stable and uncertainties are minimized.

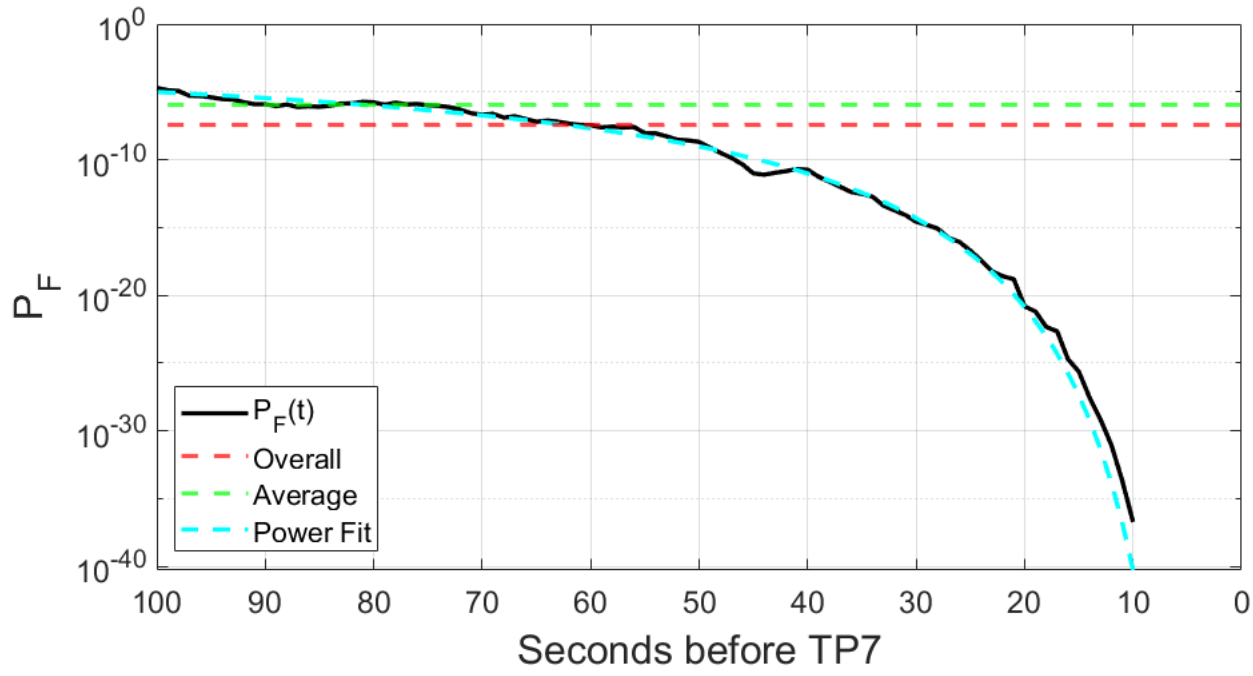


Figure 5.3 Progression of  $P_F$  During Final Approach

Two fixed reference lines are plotted: the overall failure probability of  $3.56 \times 10^{-8}$  and the average failure probability, determined as the mean of all  $P_F$  across the timeline, valued at  $9.86 \times 10^{-7}$ . Although the average may seem to signify a suitable midpoint, it inadequately represents the actual cumulative risk exposure, as it neglects the structure and interdependence of failures across time. Conversely, the comprehensive overall probability, obtained by integrating the complete energy evolution model across the entire approach window, provides a more accurate assessment of the total system susceptibility.

To better delineate the trend of  $P_F(t)$ , a nonlinear power-law representation of the form,

(5.2)

where,

(5.2a)

(5.2b)

(5.2c)

is implemented with MATLAB's Curve Fitting Toolbox.

This formulation also delineates two principal asymptotic behaviors: a vertical asymptote at  $t = 0$ , indicating the moment of touchdown, beyond which additional risk is nonexistent; and a horizontal asymptote at  $P_F = 0.13664$  (i.e.,  $10^{\epsilon}$ ), representing the upper threshold of failure probability distant from the landing phase. The resultant fit (blue dashed curve) demonstrated high goodness of fit, with a  $R^2$  value of 0.9913, corroborating the suitability of this model equation in representing the decrease in failure probability throughout the final approach.

## 5.2 Contributing Factors Breakdown

The total risk of LOC-I results from a combination of various factors; however, directly assessing the impact of each parameter is challenging due to discrepancies in units, physical significance, and their functions within the aircraft system. This section categorizes the parameters into six logical groups according to their function and physical units to elucidate their relative impact.

### 5.2.1 Landing Weight

The landing weight category includes both fuel mass and payload mass, which together constitute the aircraft's overall weight during the approach phase. The latter was presumed to remain constant, representing around 50% of the maximum cargo capacity. This assumption was essential owing to the lack of flight-specific passenger and cargo data in the dataset. Table 5.2 presents a comparison of all essential characteristics related to landing weight.

Table 5.2 Comparison of Weight Parameters on LOC-I Risk

Parameter	Average Trend Value	$\Delta P(F) (\%)$ From 10% Increase	Relative Rank
<b>Payload Mass</b>	40 666.67 kg	+ 24.59	1
<b>Fuel Mass</b>	(17 219.85 ± 9509.71) kg	+ 9.92	2

Sensitivity analysis revealed that variations in payload mass significantly influence LOC-I likelihood more than alterations in fuel mass. This is due to the former being both denser and less variant than fuel; its impact is more pronounced when altered by a certain percentage. Furthermore, fuel mass often diminishes with time, including during descent, constraining its instantaneous impact on total energy near landing.

From a risk modeling standpoint, this indicates that underestimating cargo weight may result in a non-conservative assessment of LOC-I risk, especially in scenarios when total energy is near the failure threshold. The findings highlight the necessity of precisely accounting for weight variations, particularly for factors such as payload that are frequently presumed to be constant in the absence of comprehensive manifest data.

### 5.2.2 Engine Performance

The engine performance group comprises two parameters that affect the aircraft's available thrust: engine fan speed (generally indicative of throttle setting) and maximum engine thrust. Both factors contribute to the forward force  $F_x$  in the total energy model via Equation 4.14. The comparison of all significant engine performance characteristics is displayed in Table 5.3.

Table 5.3 Comparison of Thrust Parameters on LOC-I Risk

Parameter	Average Trend Value $\Delta P(F)$ (%) From 10% Increase	Relative Rank
N <sub>1</sub> Fan Speed ( $57.14 \pm 24.33$ ) %	- 14.91	1
Max Thrust 450,000 N	- 11.61	2

In the sensitivity analysis, increasing either value led to a decrease in the likelihood of LOC-I. This aligns with expectations: more available or controlled thrust allows the aircraft to more effectively sustain or regain its energy state, hence diminishing the probability of descent instability or failing to meet the glide slope. Nevertheless, the degree of influence exhibited minor variations across the two factors.

$N_1$  assumes a marginally more significant function in the model when subjected to perturbation. The alterations influence the entire thrust profile over time, directly regulating the aircraft's kinetic energy and enhancing sustained energy levels throughout approach.  $T_{max}$ , although significant, merely elevates the maximum thrust capacity and hence has a less pronounced impact in practice unless  $N_1$  is likewise proportionately altered.

### 5.2.3 Attitude and Aerodynamic Angles

This group comprises factors that delineate the aircraft's spatial orientation and its aerodynamic interaction with airflow: angle of attack, pitch angle, and bank angle. These parameters collectively affect the force components in the energy model and the aircraft's susceptibility to instability during approach. Table 5.4 presents a comparison of all essential metrics related to the aircraft's attitude.

Table 5.4 Comparison of Aircraft Angles on LOC-I Risk

Parameter	Average Trend Value $\Delta P(F)$ (%) From 10% Increase	Relative Rank
Angle of Attack ( $5.07 \pm 8.71$ ) °	+ 194.87	1
Bank Angle ( $0.02 \pm 5.50$ ) °	+ 179.75	2
Pitch Angle ( $2.57 \pm 5.63$ ) °	+ 33.34	3

The angle of attack was shown to be the most significant parameter in the overall model in the sensitivity analysis. This is presumably due to the direct inclusion of it in the aerodynamic coefficient calculations (see Equations 4.10, 4.13, 4.14). Variations impact both lift and drag, thereby affecting the vertical and longitudinal forces incorporated in the total energy rate equation. These alterations can markedly diminish the aircraft's energy state, particularly if drag escalates abruptly, rendering it a highly sensitive factor influencing LOC-I risk.

The roll angle is subordinate to the angle of attack during perturbation. While roll does not directly influence energy through drag or lift, it decomposes gravitational forces into lateral and vertical components (refer to Equation 4.5) and affects bank-induced instability. Roll is frequently influenced by external disturbances (such as crosswinds and turbulence) or abrupt last-minute corrections near the runway, rendering it also a significant destabilizing factor.

The pitch angle exhibited a markedly diminished effect when subjected to perturbation. This is somewhat unexpected considering the geometric relationship between pitch and angle of attack (via flight path angle  $\gamma$ ), yet this finding underscores how direct aerodynamic influences prevail over indirect orientation effects in this model regarding energy outcomes. The relatively limited pitch variability in the dataset may also affect its minimal influence on the output during the sensitivity analysis.

### 5.2.4 Aircraft Velocity

This category covers the airspeed and the crosswind component of the aircraft's velocity, which characterizes the motion of the aircraft with the surrounding air. These characteristics directly affect the aircraft's kinetic energy, aerodynamic forces, and maneuverability during the approach phase. Table 5.5 presents a comparison of all essential data related to the aircraft's overall velocity.

Table 5.5 Comparison of Velocity Components on LOC-I Risk

Parameter	Average Trend Value $\Delta P(F)$ (%) From 10% Increase	Relative Rank
Crosswind ( $0.06 \pm 11.75$ ) m/s ( $58.92 \pm$ )	+ 233.99	1
Airspeed 12.93) m/s	- 44.49	2

Airspeed is commonly regarded as a fundamental measure of flying stability. This study has shown that augmenting this parameter led to a reduction in the likelihood of LOC-I. This result aligns with fundamental principles of flight physics: increased velocity enhances kinetic energy and aerodynamic control efficacy, hence granting pilots and automated systems greater command over the aircraft's orientation and responsiveness. Reduced airspeed, conversely, heightens the risk of nearing stall conditions or failing to sustain the glide path.

Conversely, the crosswind component, resulting from the lateral wind acting perpendicular to the aircraft's trajectory, exhibited a significantly lower average value and variance. Notwithstanding this, it exerted the most significant single-parameter influence on  $P(F)$  in the comprehensive analysis.

This outcome can be elucidated by the intricate way crosswind affects the energy model. Crosswind influences the sideslip angle ( $\beta$ ), which subsequently modifies the lateral force coefficient ( $C_L$ ), impacts yaw dynamics, and frequently necessitates unintentional roll adjustments, particularly during manual control or crosswind landings. The outcome is a cumulative destabilizing effect, especially in the last moments preceding touchdown.

### 5.2.5 Control Surface Deflection

This segment covers elevator deflection and flap deflection, which are metrics that indicate pilot or autopilot control inputs. The control surfaces directly affect the aircraft's aerodynamic coefficients and, consequently, its overall energy state and stability during flight. Table 5.6 presents a comparison of all essential data related to the aircraft's control surfaces.

Table 5.6 Comparison of Control Surface Deflection on LOC-I Risk

Parameter	Average Trend Value $\Delta P(F)$ (%) From 10% Increase	Relative Rank
Elevator Deflection ( $0.76 \pm 24.61$ ) °	+ 8.08	1
Flap Deflection ( $35.61 \pm 1.43$ ) °	+ 2.78	2

Flap deflection exhibited relative consistency throughout all flights. The slight variance adheres to regular operating procedures: flaps are typically fully extended or maintained at fixed positions during the final approach to enhance lift and facilitate reduced approach speeds. The smaller positive shift may indicate modest negative impacts due to higher drag or a reduction in stall margin at the energy envelope's conclusion.

In contrast, the variance of elevator deflection was noticeably greater. This larger spread suggests that elevator input fluctuates dynamically during flights, perhaps in reaction to pitch commands and precise adjustments to the vertical flight path. The model indicated that elevator deflection exerts a greater impact than flap deflection; however still minor in comparison to factors such as crosswind or angle of attack.

This comparison can also illustrate how parameter variance influences sensitivity inside the model. Flap deflection, while physically significant, is operationally constant and seldom varies. Hence, its capacity to affect the energy state is restricted. Elevator deflection, albeit exhibiting a reduced average magnitude, has significant variability across flights and time, enabling its disruption to exert a more pronounced influence on the estimated energy trajectory. The larger the natural variability, the more influence a parameter has during sensitivity analyses, as it impacts the energy trajectory across a wider spectrum of potential scenarios.

### 5.2.6 Atmospheric Conditions

The concluding parameter group comprises a singular yet fundamental variable: air density. Although not a direct control input or flight dynamic parameter, air density significantly influences aerodynamic forces and engine performance during flight, particularly during approach, where altitude, temperature, and pressure gradients can

change rapidly. Table 5.7 exclusively presents the remaining uncategorized parameter, which is air density.

Table 5.7 Atmospheric Conditions on LOC-I Risk

Parameter	Average Trend Value	$\Delta P(F) (%)$ From 10% Increase	Relative Rank
Air Density	( $1.1799 \pm 0.0245$ ) kg/m <sup>3</sup>	-22.52	1

According to the sensitivity analysis, the probability of LOC-I decreased as air density rose. This inverse relationship corresponds with scientific intuition: increased air density elevates dynamic pressure (refer to Equations 4.8, 4.9), hence enhancing lift and control authority at any specified airspeed. This can improve stability, especially in the energy model, where aerodynamic force components are proportional to  $\rho$ , affecting both lift and drag coefficients and consequently the overall energy state of the aircraft.

### 5.2.7 Rankings Overview and Comparison

To summarize the ranking outcomes, three methodologies were utilized to assess parameter significance. The initial two were thoroughly elucidated in Sections 4.4 and 4.5, in conjunction with Sections 5.2.1 to 5.2.6 on the relative ranks. The third option entails a mean-rank ordering by averaging the two preceding approaches to offer a balanced viewpoint (with a minor inclination towards the scoring methodology to address tied averages). All three are comprehensively detailed in Table 5.8, providing an overview of the ranking of input parameters associated with LOC-I.

Table 5.8 Compiled Orders of Ranking on Parameter Significance

#### Rank $\Delta P(F)$ -Based Order Scoring-Based Order Averaged Ranking Order

1	Crosswind	N <sub>1</sub> Fan Speed	Angle of Attack
2	Angle of Attack	Angle of Attack	Crosswind
3	Bank Angle	Crosswind	N <sub>1</sub> Fan Speed
4	Airspeed	Fuel Mass	Airspeed
5	Pitch Angle	Airspeed	Fuel Mass
6	N <sub>1</sub> Fan Speed	Pitch Angle	Bank Angle
7	Fuel Mass	Bank Angle	Pitch Angle
8	Elevator Deflection	Elevator Deflection	Elevator Deflection

Despite variations in rankings, three characteristics regularly occupy the highest positions: angle of attack, crosswind, and N<sub>1</sub>.  $\alpha$  is the most immediate and dependable predictor of stall, rendering it the most causally significant component in loss of control. Crosswind, while not directly associated with stall, undermines lateral stability and control, especially at touchdown. Both conform to accepted aerodynamic principles.

The manual perturbation approach more accurately represents physical causality for N<sub>1</sub>, as it directly quantifies the response of failure probability to proportional variations in each input. That method assigned N<sub>1</sub> a far lower rank, corroborating the notion that its significance score in the toolbox is more statistical than physical. This argument is also substantiated by the previous 2 observed parameter distributions: AoA and crosswind exhibited narrower spreads yet demonstrated a stronger physical connection to stall mechanics, whereas N<sub>1</sub>'s wider distribution resulted in greater overlap with failure samples, hence inflating its score.

### 5.3 Proposed Safety Improvement

This section examines and discusses a feasible, quantitative mitigation technique to further diminish the danger of LOC-I during approach, given the model's extremely low but non-zero baseline likelihood. Two primary strategies were initially evaluated: limiting crosswind thresholds during approach or altering the flight profile by varying critical factors such as airspeed, pitch, and angle of attack.

The initial option, although theoretically sound, presents considerable logistical and operational difficulties. Flights must either enter holding patterns or divert to alternate runways, both of which result in increased fuel consumption, heightened controller workload, and passenger delays. Furthermore, the current crosswind restrictions specified in the Operations Manual [27] are founded on comprehensive validation under expert supervision and recognize that safe landings in elevated crosswinds are feasible contingent upon pilot proficiency. Consequently, implementing more stringent norms may face operational resistance and could lead to less compliance or unforeseen problems.

Instead, a minor modification to the flight profile was evaluated: increasing the aircraft's airspeed by 10 knots (~5.14 m/s) during approach, while sustaining the same vertical speed and flight path angle (~3°). To offset the rise in horizontal velocity and preserve the identical descending trajectory, both the angle of attack and pitch were lowered by approximately 0.24°. N<sub>1</sub> (and thrust T as a result) was maintained constant, presuming that the higher velocity could be attained mostly by a little alteration in aerodynamic attitude rather than an increase in power.

This adjusted speed also still adheres to established operational guidelines. The FAA Airplane Flying Handbook [35] states that the advised final approach speed is 1.3V<sub>SO</sub>, with V<sub>SO</sub> representing the stall speed in landing configuration. For the estimated V<sub>SO</sub> of approximately 68 knots, the resulting approach speed is roughly 88 knots. The modified speed in this context, with a lower limit of 97 knots from 87 knots in the dataset, remains over this threshold.

To implement this proposal, the modification is reintroduced into the model threshold calculation process, and the outcome is illustrated in Figure 5.5, which displays a little leftward shift. Consequently, it indicates that the threshold for the occurrence of LOC-I has diminished, suggesting that the associated risk will similarly reduce.

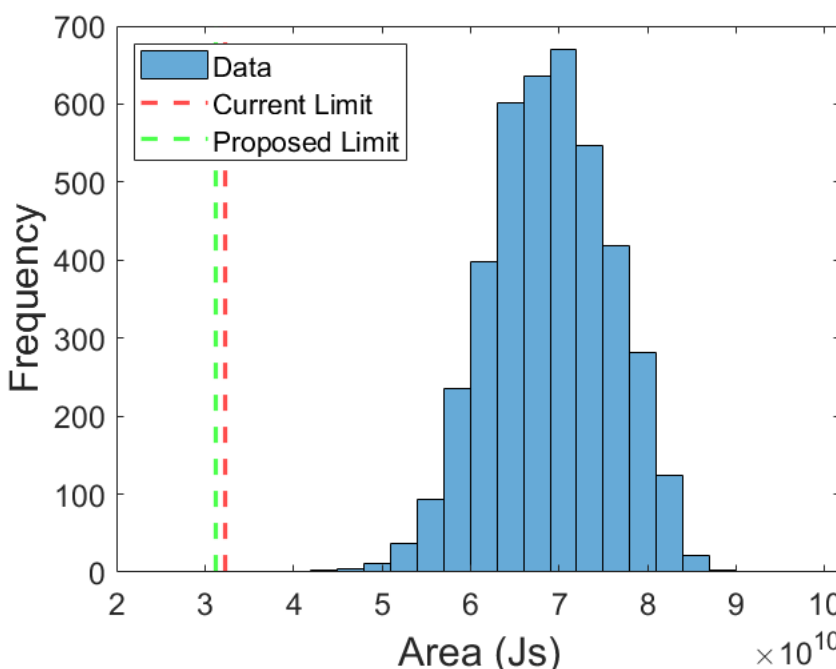


Figure 5.4 Proposed Change for LOC-I Threshold

This also alters the  $P_F(t)$  curve marginally, as illustrated in Figure 5.6, but it is not distinctly apparent (note the little blue patches along the line), indicating that the change in  $P_F$  is not represented in the logarithmic (or power) scale.

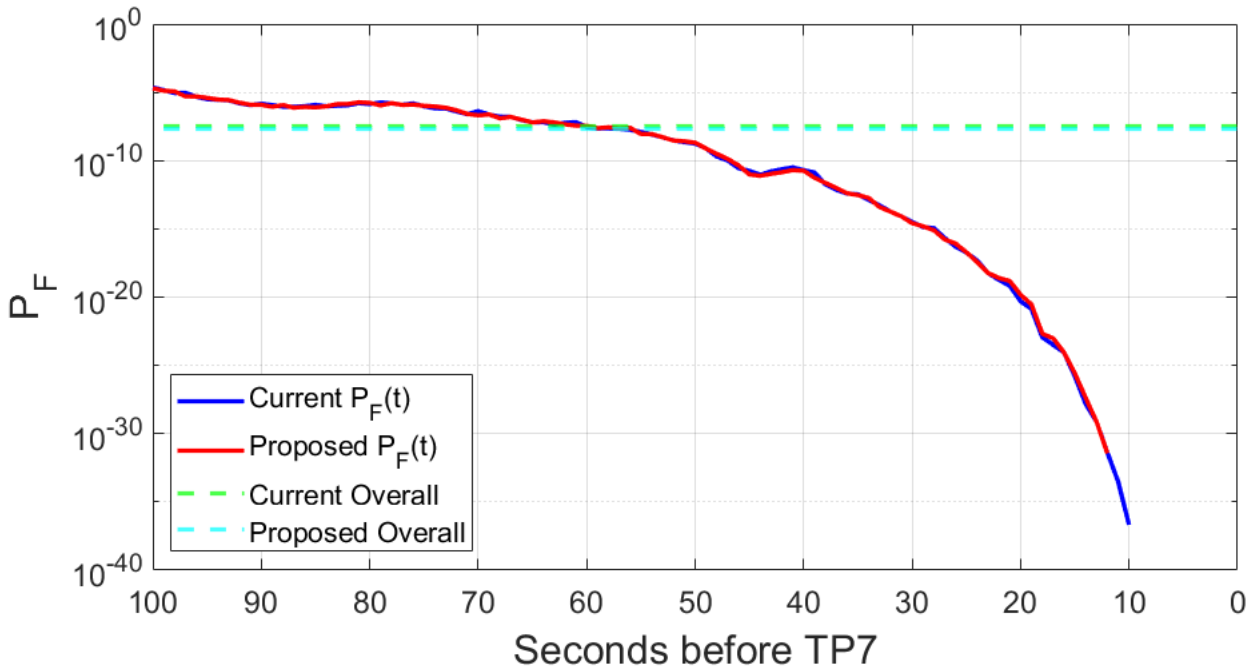


Figure 5.5  $P_F$  Change After Safety Proposal

The proposed change was modeled utilizing the previously employed energy-based subset simulation methodology. The chance of failure decreased from  $3.57 \times 10^{-8}$  to  $1.94 \times 10^{-8}$ , indicating a 45.56% reduction in the risk of LOC-I. This diminishes the aircraft's vulnerability to elevated angles of attack and low speeds, both critical factors. The small adjustments indicate that the modification is probably achievable within the current approach protocols and may align with the typical range of pilot or autopilot actions.

In addition, to validate the feasibility of the increased airspeed from a landing distance standpoint, braking deceleration from the dataset was examined. The duration was delineated from touchdown (TP7) until ground speed diminished to roughly 26 m/s (coincidentally near TP8), after which many flight data fell to zero (see Figure 3.8). The braking distance is determined using the formula

$$(5.3)$$

$$(5.4)$$

Where  $a_{brake}$  represents the average deceleration and  $t$  denotes the time in seconds (see Appendix, Time Point Data). The deceleration phase, assumed by a constant braking rate, represents a simplified approximation of the ground rollout portion after touchdown. Although actual braking performance may fluctuate due to elements like reverse thrust activation, runway gradient, surface conditions, and pilot actions, the presumption of consistent deceleration provides a pragmatic approach to predicting stopping distance over numerous flights. The decision to have a continuous brake was designed to reconcile interpretability with consistency, facilitating comparisons across various landing profiles without necessitating intricate modeling of braking mechanics. This strategy, while not capturing the complete variety of post-touchdown behavior, indicates that the grouping of distances between 600 and 900 meters serves as a fair first-order approximation for this investigation.

Figures 5.7 and 5.8 illustrate a comparison between the projected alteration in braking time and the requisite runway distance. In all instances, the suggested safety enhancement resulted in an approximate doubling of both values, potentially indicating an inversely proportionate relationship to the change in  $P_F$ , hence corroborating the presumed heightened risk after landing.

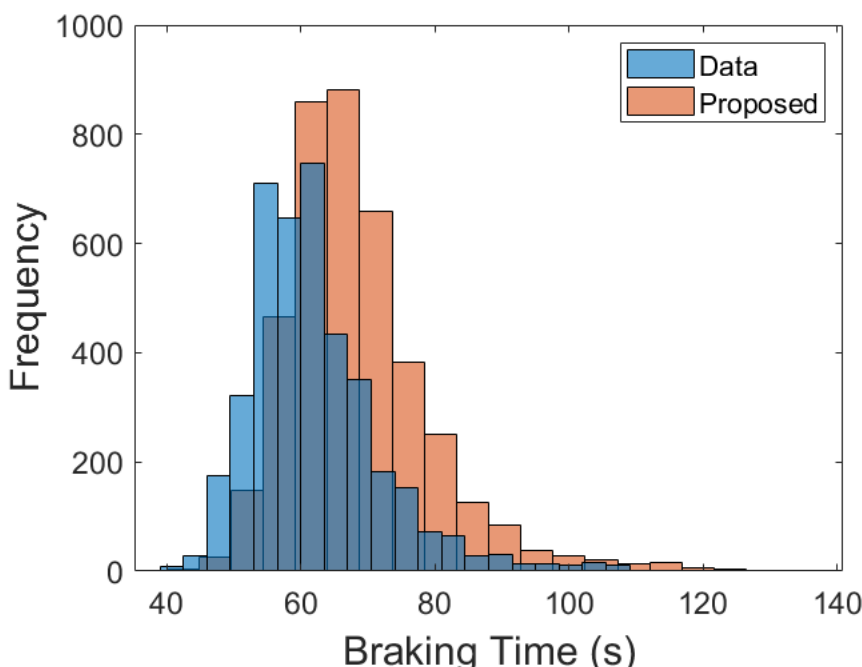


Figure 5.6 Estimated Time of Deceleration from Touchdown to  $V = 26$  m/s

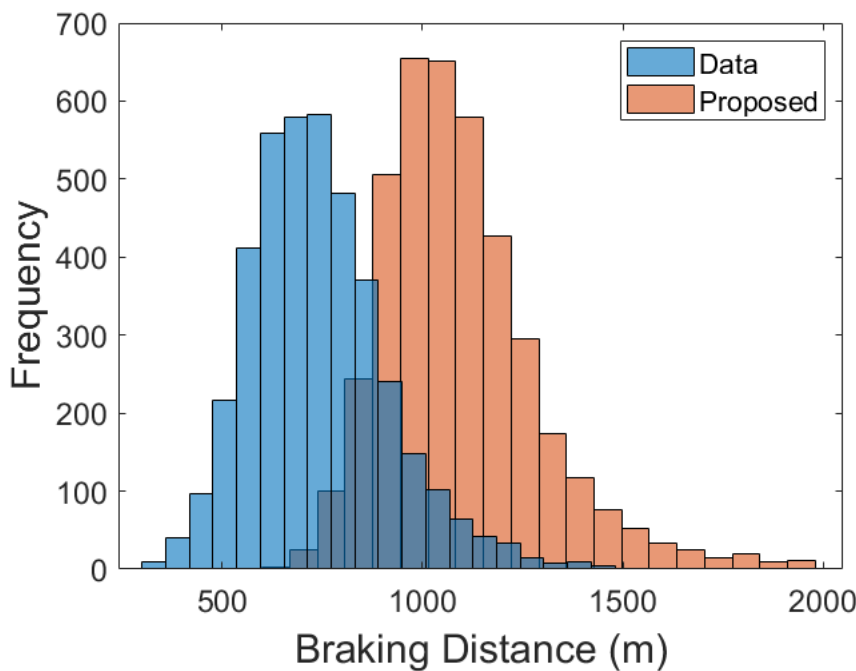


Figure 5.7 Estimated Deceleration Distance from Touchdown to V = 26 m/s

Given that the runway utilized in this study measures 2500 m (refer to Figure 3.1) and with an assumption of heavier (up to twice in magnitude) deceleration, a significant braking margin persists without any prior assumptions in existing surface conditions, aircraft configuration, or environmental variables. This suggests that despite increased kinetic energy from an elevated approach speed, the aircraft would hopefully be within reason that it is still inside a safe stopping distance. However, to accurately evaluate the runway overrun risk, another research would be needed (using a methodology that is similarly used in this paper).

## Chapter 6

### Conclusions and Recommendation

#### 6.1 Conclusion

This thesis introduced a data-driven, energy-based probabilistic model to evaluate the likelihood of Loss of Control in-flight (LOC-I) during the final approach phase of a Boeing 747. It concentrated on the last 1000 feet AGL approaching KMSP Runway 30R, aiming to quantify the impact of deviations in flight parameters on the aircraft's energy profile and the potential for these deviations to result in infrequent yet severe failure situations. It also integrates physical modeling, statistical fitting, and both static and dynamic rare-event simulation techniques to deliver a reproducible method for risk quantification and to elucidate the evolving dynamics influencing aircraft stability during this critical flight segment.

The study is organized around three key issues from which multiple conclusions can be derived:

1. This study's total energy-based model employs the physical notion of energy rate (refer to Equations 4.2, 4.3). Force components encompass contributions from aerodynamic lift and drag, gravitational forces, and engine thrust, all of which depend on critical flight parameters like airspeed, angle of attack, mass, pitch, roll, and control surface deflections. These model-based outputs were also preserved and included in the final data repository to support dynamic risk simulation in subsequent stages.

The model was then employed to produce temporal energy profiles for each trip, which were then compared to the actual energy obtained from real flight data (via QAR). Principal observations include:

- The model accurately recorded the energy trajectories over 150 seconds before touchdown.
- Downsampling and smoothing guaranteed that profiles from both the data and the model were synchronized at a 1 Hz resolution throughout 151-time steps.
- Discrepancies in data, such as radio altitude, were either unavoidable or difficult to resolve, including the possible addition of more control dynamics during the approach phase.

1. In this study, LOC-I was defined as an occurrence where the aircraft's total energy drops below a model-derived threshold, signifying aerodynamic instability, loss of lift, or incapacity to maintain controlled flight for landing. The criterion was established on:
  - Adjusting model input profiles (angle of attack, velocity, crosswind, and bank angle) to align with essential operational thresholds derived from literature and manuals.
  - Employing the lower bound (mean minus  $1\sigma$ ) of the resultant degraded energy profile as the dynamic LOC-I threshold.
  - The integration of this threshold during the approach phase yielded a critical energy area of roughly  $3.22 \times 10^9$  J, which served as a base failure benchmark.

To model the overall likelihood of such an infrequent occurrence:

- Subset simulation was executed with MCMC sampling with 500,000 samples, enhancing a previous attempt of 10,000 samples.
- The method effectively investigated the failure zone without necessitating exhaustive sampling.
- The projected baseline probability of LOC-I was:  $3.57 \times 10^{-8}$  (utilizing 500,000 samples) vs  $2.80 \times 10^{-8}$  (utilizing 10,000 samples)
- Significant reductions in computational time were achieved (about 18 seconds compared to possible hours from direct Monte Carlo).

While this single-run estimate served as a robust baseline, an extended variant of the method was introduced to capture time-varying changes:

- An iterative simulation was created by including the energy model directly into the subset simulation loop at each second of the process.
  - Parameter distributions were dynamically propagated throughout time, facilitating the estimation of failure probability as a function.
  - A power-law curve represented by Equation 5.2 was fitted to the resultant probability curve utilizing MATLAB's nonlinear least squares fitting toolbox, attaining a high goodness-of-fit ( $R^2 = 0.9913$ ).
  - The fit demonstrates an exponential decline in failure probability as the aircraft approaches touchdown, aligning with the hypothesis that risk decreases during the stabilized final approach phase.
1. A two-pronged sensitivity analysis was conducted to assess which flying characteristics most substantially influence the probability of Loss of Control (LOC-I).
    - A manual approach entailed incrementally modifying each parameter by +10% while maintaining the others constant, followed by re-executing the simulation to assess the variation in P\_F.
    - A toolbox-assisted technique utilized internal statistical rankings derived from the subset simulation toolbox, focusing on parameter prevalence in failure-inducing samples during the per-second approach simulation.

However, to unify these perspectives, a composite ranking was derived by averaging the results from both methods, providing a balanced view of each parameter's importance.

- Significant Influence: Angle of attack, crosswind, and  $N_1$  are the essential determinants of aerodynamic stability and energy availability during approach.
- Moderate Influence: Airspeed, fuel mass, and pitch angle impact the aircraft's fall energy profile and control dynamics.
- Minimal Influence: Bank angle and elevator deflection exhibited a relatively insignificant effect on the failure probability in the simulated scenario.

Subset simulation proved to be effective and scalable for predicting rare-event probabilities in high-dimensional environments, facilitating precise estimates of low-probability occurrences such as LOC-I events. Stochastic simulation methods, such as subset simulation, have been employed in domains including structural engineering, flood and climate risk evaluation, and nuclear safety. Nevertheless, they possess drawbacks, including sensitivity to the definition of failure thresholds, dependence on precise statistical models, and difficulty in interpretability within complicated, nonlinear dynamics.

Moreover, considerable work was devoted to the preparation and analysis of the flight data (4220 flights) before modeling and simulation. Preprocessing commenced with the initial truncation of each flight's data to either 500 or 250 feet AGL, followed by an analysis of the histogram of readings at these intervals for distribution fitting. Outlier identification methods, including statistical filtering like Grubbs' test, were employed to eliminate erroneous or non-physical numbers, particularly in altitude and energy measurements. Though the records were ultimately downsampled to 1 Hz and extended to a period of 1000 ft AGL, with final approach lengths varying from 100 to 150 seconds, establishing 95 seconds (before touchdown) as the reference timeframe for subsequent analyses.

## 6.2 Recommendations and Future Works

The subsequent two subsections delineate pragmatic recommendations derived from the simulation results. Section 6.2.1 outlines a pragmatic mitigation technique based on sensitivity analysis, recommending process modifications to diminish the likelihood of LOC-I during the approach. Section 6.2.2 delineates prospective research avenues focused on improving modeling precision, broadening scenario applicability, and optimizing the simulation framework for wider utilization.

### 6.2.1 Mitigation Strategy

Results indicate that the most effective mitigation option to decrease the likelihood of LOC-I during approach is to execute a modification in flight procedures. Increasing airspeed by 10 knots while proportionately decreasing both the angle of attack and pitch by approximately  $0.24^\circ$  enables the aircraft to sustain the same descent angle and vertical velocity. This alteration leads to a substantial decrease in the anticipated failure probability while adhering to operationally acceptable parameters, including the FAA's approach speed guideline. The technique maintains thrust settings, with the hope of minimizing the introduction of future additional risks like runway overruns or hard landings.

### 6.2.2 Future Works

Multiple avenues for further research are proposed:

- Expanding the overall energy model by including dynamic motion and its development to other aircraft types.

For example, incorporate dynamic flight equations to capture time-dependent motion and extend the method to different aircraft types for broader applicability.

- Integrating real-time environmental factors into the simulation process.

For example, add real-time disturbances like wind shear or turbulence into simulations to reflect more realistic operational variability.

- Simulating system degradations to assess threshold robustness.

For example, model failures in control surfaces or pilot reaction delays are used to test how resilient the thresholds are under abnormal conditions.

- Enhancing the definition of failure situations by high-fidelity simulations or pilot-in-the-loop testing.

For example, use high-fidelity aircraft simulators or human-in-the-loop testing to validate whether the failure thresholds truly reflect operational loss of control.

- Investigating consequence-driven risk models by integrating failure probability with severity assessment.

For example, go beyond just using probability by combining risk estimates with potential impact severity to prioritize safety interventions.

## References

S.-K. Au and J. L. Beck, "Estimation of small failure probabilities in high dimensions by subset simulation," *Probabilistic Engineering Mechanics*, vol. 16, no. 4, pp. 263-277, 2001.

J. S. Dag<sup>⑧</sup>

punar, *Simulation and Monte Carlo With Applications In Finance and MCMC*, England: John Wiley & Sons Ltd, 2007.

J. Sembiring, "A Heuristic Parameter<sup>⑩</sup>

Estimation Approach for FDM Data," Technische Universität München, Munich, 2019.

- [1] IATA, "Environmental Factors Affecting Loss of Control In-Flight: Best Practice for Threat Recognition & Management," Montreal, Quebec, 2016.
- [2] D. C. Nage<sup>⑥</sup>
- [3] I, "Human Error in Aviation Operations," in *Human Factors In Aviation*, Academic Press, Inc., 1988, pp. 263-303.
- [4] D. Kulkarni, Y. Wang, M. Windrem and R. Keller, "Aviation Data Integration System," NASA Ames Research Center, Moffett Field, CA, 2003.
- [5] R. Shone, K. Glazebrook and K. G. Zografos, "Applications of stochastic modeling in air traffic management: Methods, challenges and opportunities for solving air traffic problems under uncertainty," *European Journal of Operational Research*, vol. 292, no. 1, pp. 1-26, 2021.
- [6] J. D. Anderson and C. P. Cadou, *Fundamentals of Aerodynamics*, New York, NY: McGraw Hill LLC, 2024.
- [7] C. M. Belcastro and J. V. Foster, "Aircraft Loss-of-Control Accident Analysis," NASA Langley Research Center, Hampton, VA, 2010.
- [8] Federal Aviation Administration, "Chapter 4 - Approaches," in *Instrument Procedures Handbook*, U.S. Department of Transportation, 2017, pp. 4-1 - 4-78.
- [9] S. M. Ross, *Introduction to Probability Models*, Los Angeles, CA: Elsevier Inc., 2010.
- [10] S.-K. Au and Y. Wang, *Engineering Risk Assessment with Subset Simulation*, Singapore: John Wiley & Sons, 2014.
- [11] S. Karlin and H. M. Taylor, *A First Course In Stochastic Processes*, London: Academic Press, Inc., 1975.
- [12] A. Pilko, M. Ferraro and J. Scanlan, "Quantifying Specific Operation Airborne Collision Risk through Monte Carlo Simulation," *Aerospace*, vol. 10, no. 7, p. 593, 2023.
- [13] H. Chen, L. Li and Y. Sun, "Risk Assessment of Aero Engine Failure based on Monte Carlo Simulation," *Procedia Engineering*, vol. 80, pp. 415-423, 2014.
- [14] E. Soydemir and P. Petratous, "Monte Carlo Analysis: An Application to Aircraft Design and Crash," *Aerospace*, vol. 8, no. 6, p. 161, 2021.
- [15] M. Bogalecka and E. Dąbrowska, "Monte Carlo Simulation Approach to Ship Crashing Accidents Consequences Assessment," *Water*, vol. 15, no. 10, p. 1824, 2023.
- [16] A. L. Visintini, W. Glover, J. Lygeros and J. Maciejowski, "Monte Carlo Optimization for Conflict Resolution in Air Traffic Control," *IEEE Transactions on Intelligent Transportation Systems*, vol. 7, no. 4, pp. 470-482, 2006.
- [17] H. Reed, C. A. Leckey, A. Dick, G. Harvey and J. Dobson, "A Model-Based, Bayesian Solution for Characterization of Complex Damage Scenarios in Aerospace Composite Structures," *Ultrasonics*, vol. 82, pp. 272-288, 2018.
- [18] S. Xuan, Y. Xi, C. Huang, S. Hu and L. Zhang, "Spatial Markov Chain Simulation Model of Accident Risk for Marine Traffic," in *4th International Conference on Transportation Information and Safety (ICTIS)*, Banff, AB, Canada, 2017.
- [19] M. Shiao, T.-K. Chen and Z. Mao, "Probabilistic Maintenance-Free Operating Period via Bayesian Filter with Markov Chain Monte Carlo (MCMC) Simulations and Subset Simulation," *Model Validation and Uncertainty Quantification*, vol. 3, pp. 225-234, 2018.

- [21] C. Mishra, S. Maskell, S.-K. Au and J. F. Ralph, "Efficient Estimation of Probability of Conflict Between Air Traffic Using Subset Simulation," *IEEE Transactions on Aerospace and Electronic Systems*, vol. 55, no. 6, pp. 2719-2742, 2019.
- [22] D. Löbl and F. Holzapfel, "Subset Simulation for Estimating Small Failure Probabilities of an Aerial System Subject to Atmospheric Turbulences," in *AIAA Atmospheric Flight Mechanics Conference*, Kissimmee, Florida, 2015.
- [23] V. Klein and E. A. Morelli, Aircraft System Identification: Theory and Practice, Alexander Bell Drive, Reston, VA 20191: American Institute of Aeronautics and Astronautics, Inc., 2006.
- Startup, "Boeing: The right choice for the large airplane," May 2010. [Online]. Available: [https://www.boeing.com/content/dam/boeing/boeingdotcom/company/about\\_bca/startup/pdf/historical/747-400-passenger.pdf](https://www.boeing.com/content/dam/boeing/boeingdotcom/company/about_bca/startup/pdf/historical/747-400-passenger.pdf). [Accessed March 2025].
- [25] M. Cavcar, "The International Standard Atmosphere," Anadolu University, Eskisehir.
- [26]
- (10)
- [27] The Boeing Company, 747-441 Operations Manual, Seattle, WA, 2000.
- [28] J. E. Wilborn and J. V. Foster, "Defining Commercial Transport Loss-of-Control: A Quantitative Approach," in *AIAA Atmospheric Flight Mechanics Conference and Exhibit*, Providence, RI, 2004.
- [29] F. Schwaiger, D. Shi, C. Mishra, L. Höhndorf and F. Holzapfel, "A Modular Subset Simulation Toolbox for Matlab," in *AIAA Scitech 2022 Forum*, 2022.
- [30] Accidents Investigation Division, "Aircraft Accident (21) Report 1/95: Report on the (21) accident to Boeing 747-409B B-165 at Hong Kong Internat(21)ional Airport on 4 November 1993," Civil Aviation Department, Hong Kong, 1995.
- National Transportation Safety Board, "Aircraft Accident Report: In-flight Icing Encounter And Loss Of Control Simmons Airlines, D(5)b.a.
- [31] American Eagle Flight 4184 Avions De Transport R(6)e gional (ATR) Model 72-212, N401AM Ro(6)selawn, Indiana October 31, 1994," Washington D.C., 1996.
- [32] National Transportation Safety Board, "Aircraft Accident Report: In-flight Icing Encounter And Uncontrolled Collision With Terrain Comair Flight 3272 Embraer EMB-120RT, N265CA Monroe, Michigan January 9, 1997," Washington D.C., 1998.
- [33] Federal Aviation Administration, "FlightAware," 18 February 2024. [Online]. Available: <https://www.flightradar24.com/resources/airport/KMSP/IAP/ILS+OR+LOC+RWY+30R>. [Accessed 5 October 2024].
- [34] Federal Aviation Administration, "Chapter 9: Approaches and Landings," in *Airplane Flying Handbook (FAA-H-8083-3C)*, U.S. Department of Transportation, 2021, pp. 9-1 - 9-38.

## Appendix A

### GitHub Repository

A GitHub repository has been established to facilitate the replication of this investigation. The repository includes essential MATLAB scripts and curated data files utilized in the study, systematically arranged for clarity and reusability. The repository is available at:

[https://github.com/DanAlex-03/KMSP-B747\\_LOCI\\_RiskQ](https://github.com/DanAlex-03/KMSP-B747_LOCI_RiskQ)

The repository has the following contents:

### A.1 MATLAB Code

- Preprocessing Scripts
- Flight Data Trimming
- Energy Model and Threshold Calculator
- Parameter Progression Plotter
- Numerical Integration Utility and Histogram Generator
- Iterative Subset Simulation Framework (based on [31])

### A.2 Data Files

- Time Points per Flight
- Parameter Label Reference
- Sample Flight Data (.csv)
- Model-Based Total Energy Output

## Appendix B

### Sensitivity Plots

This appendix presents the outcomes of the Subset Simulation Toolbox's sensitivity plot for the remaining seven input parameters at T = 25 s for Figures B.1 to B.7.

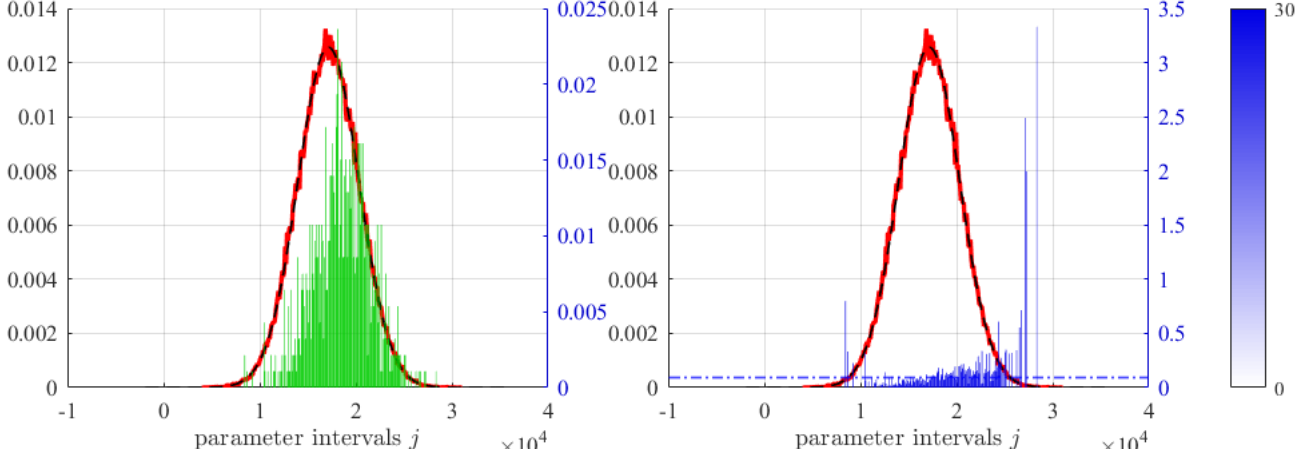
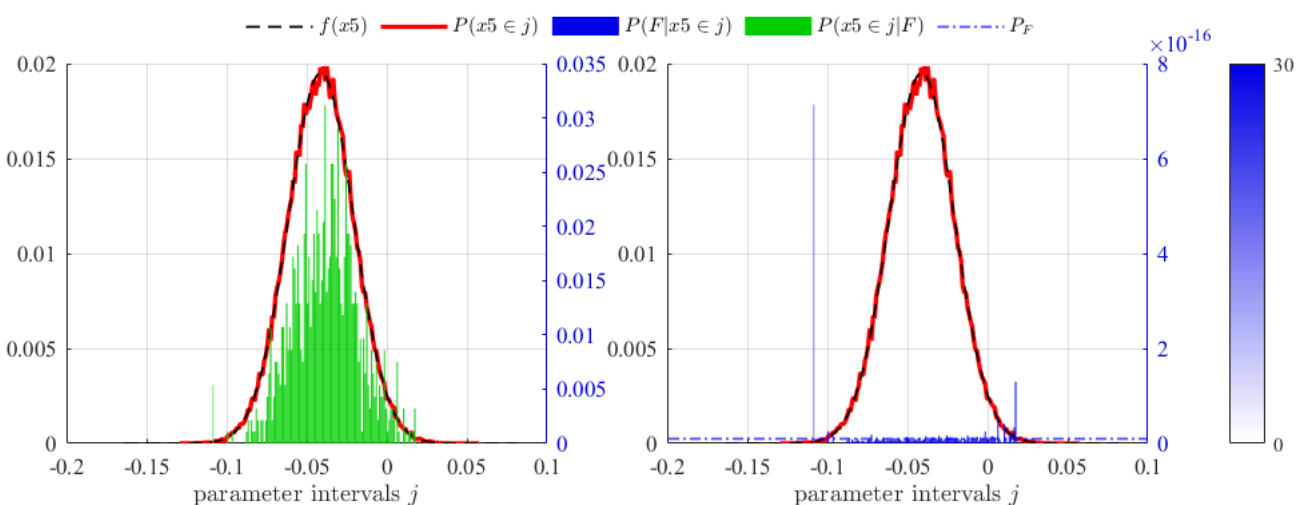
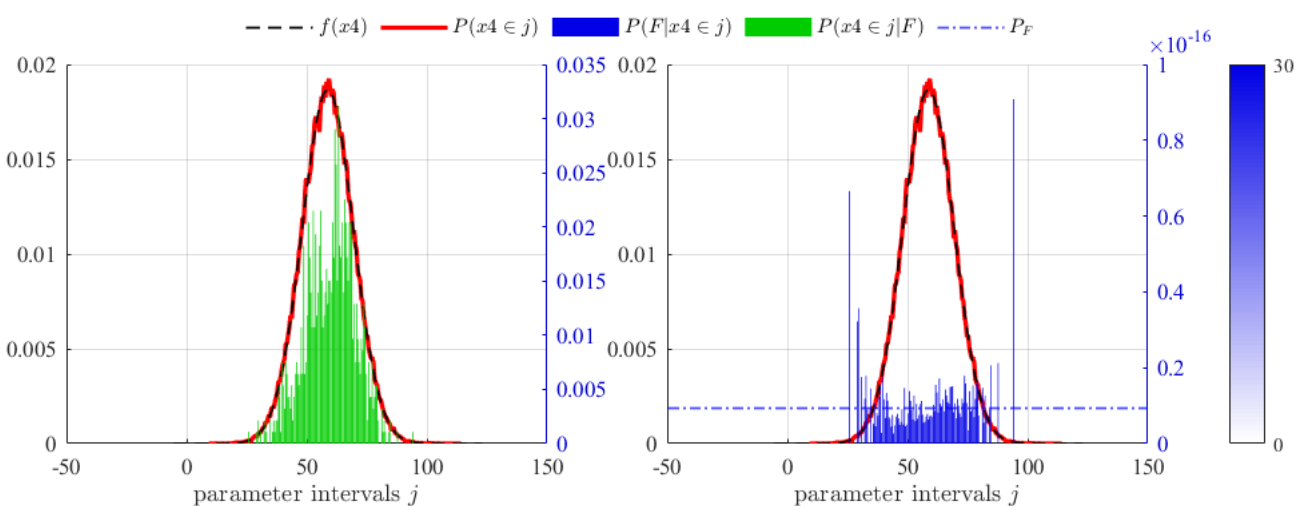
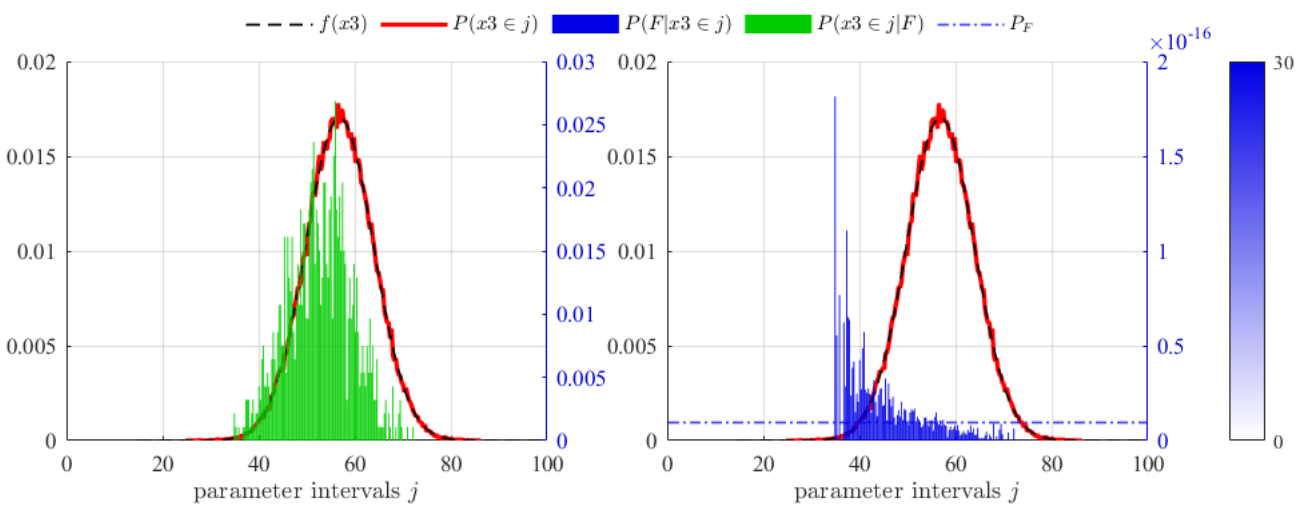


Figure B.1 Fuel Mass Sensitivity Plot at T = 25 s



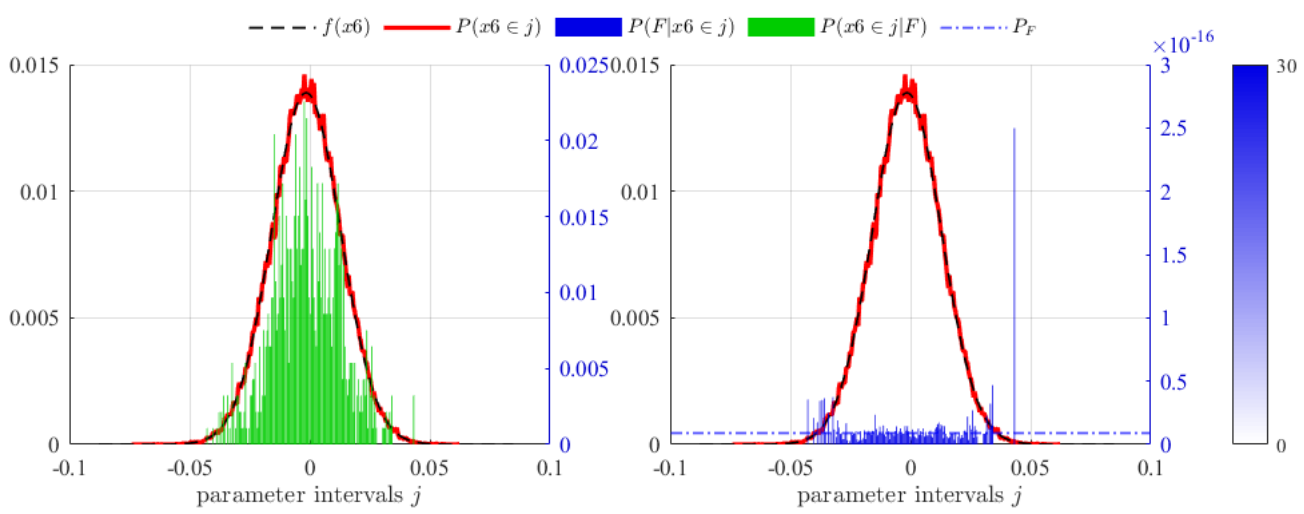


Figure B.5 Roll Angle Sensitivity Plot at  $T = 25$  s

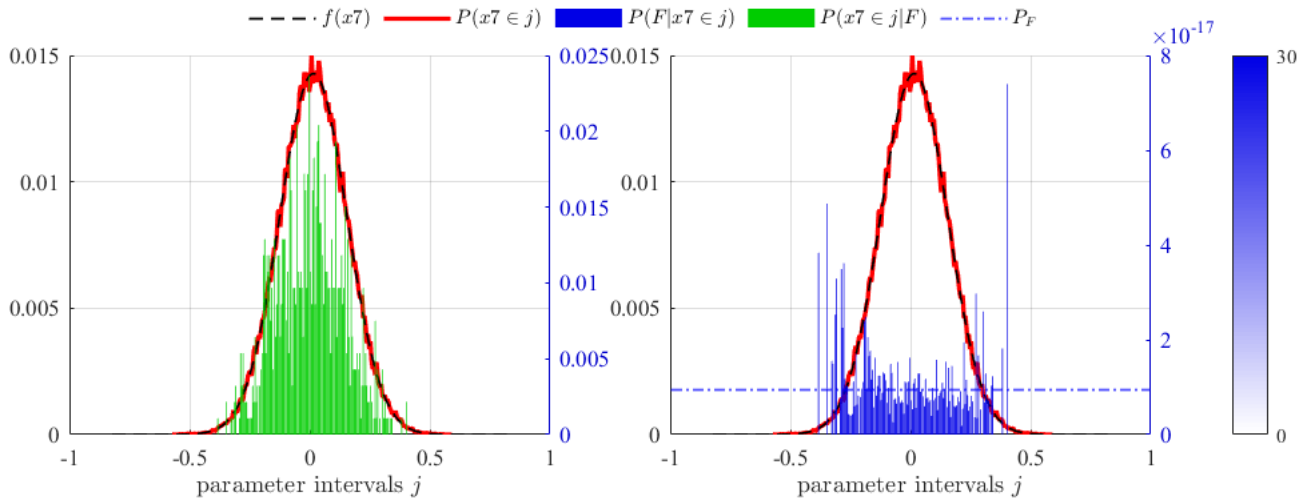


Figure B.6 Elevator Deflection Sensitivity Plot at  $T = 25$  s

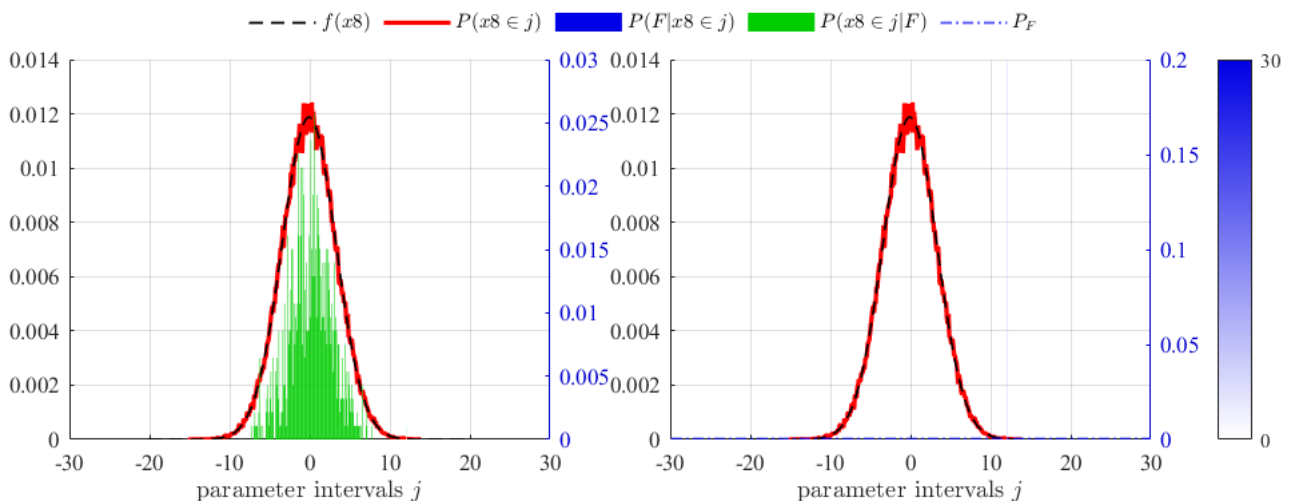


Figure B.7 Crosswind Sensitivity Plot at  $T = 25$  s

## Appendix C

### Parameter Plots

This appendix presents graphs from Figures C.1 to C.10 illustrating the variation of the LOC-I contributing parameters whose values fluctuate during the final approach phase.

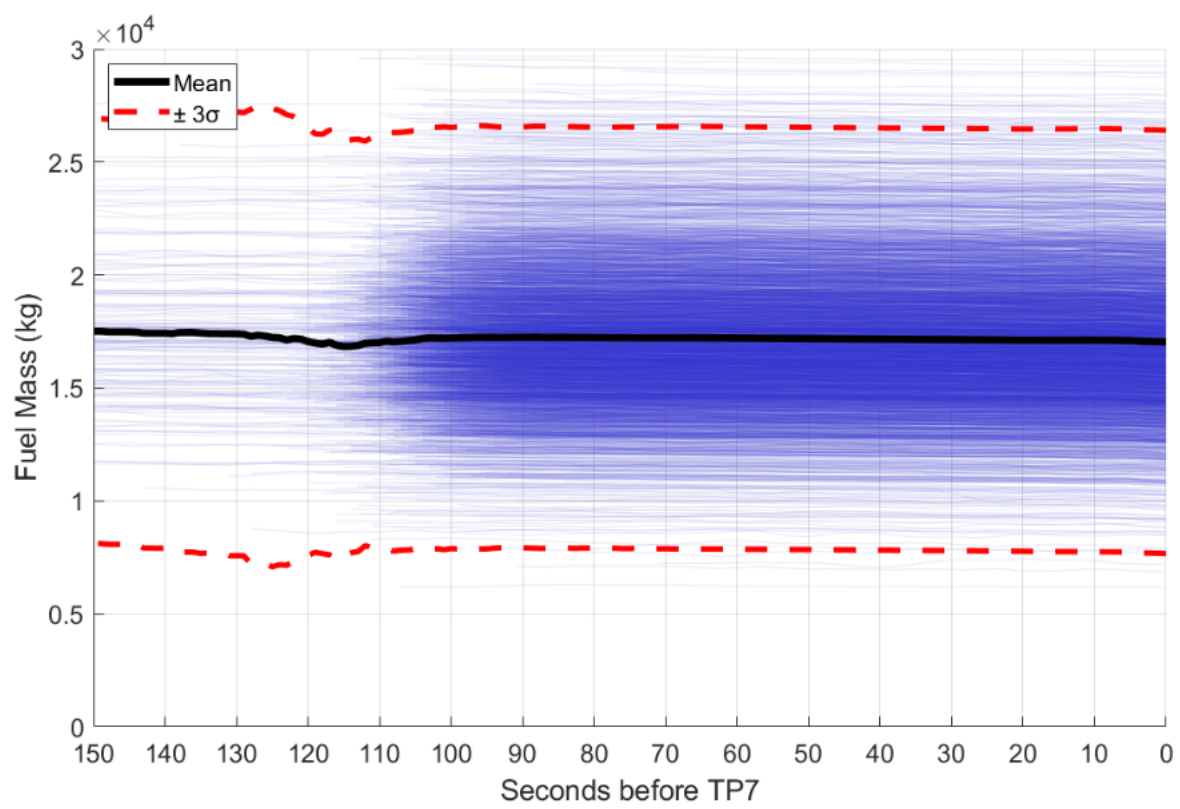


Figure C.1 Fuel Quantity Progression Plot

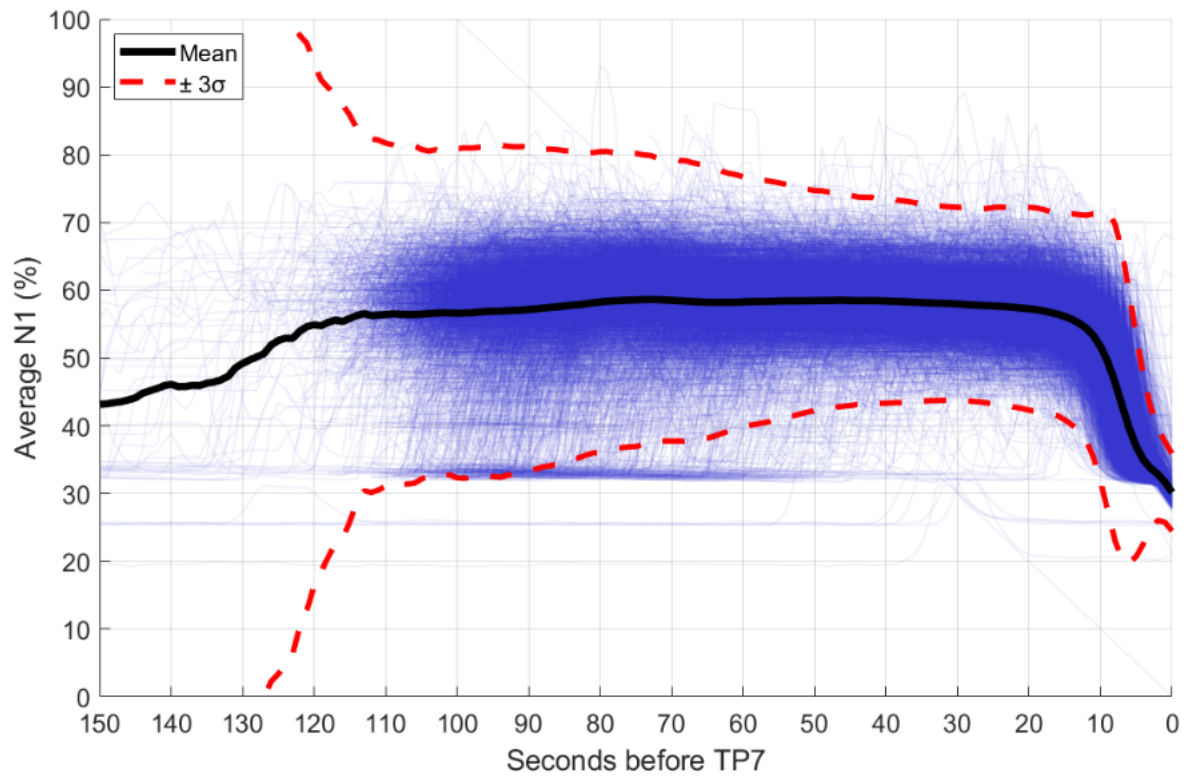


Figure C.2 N<sub>1</sub> Progression Plot

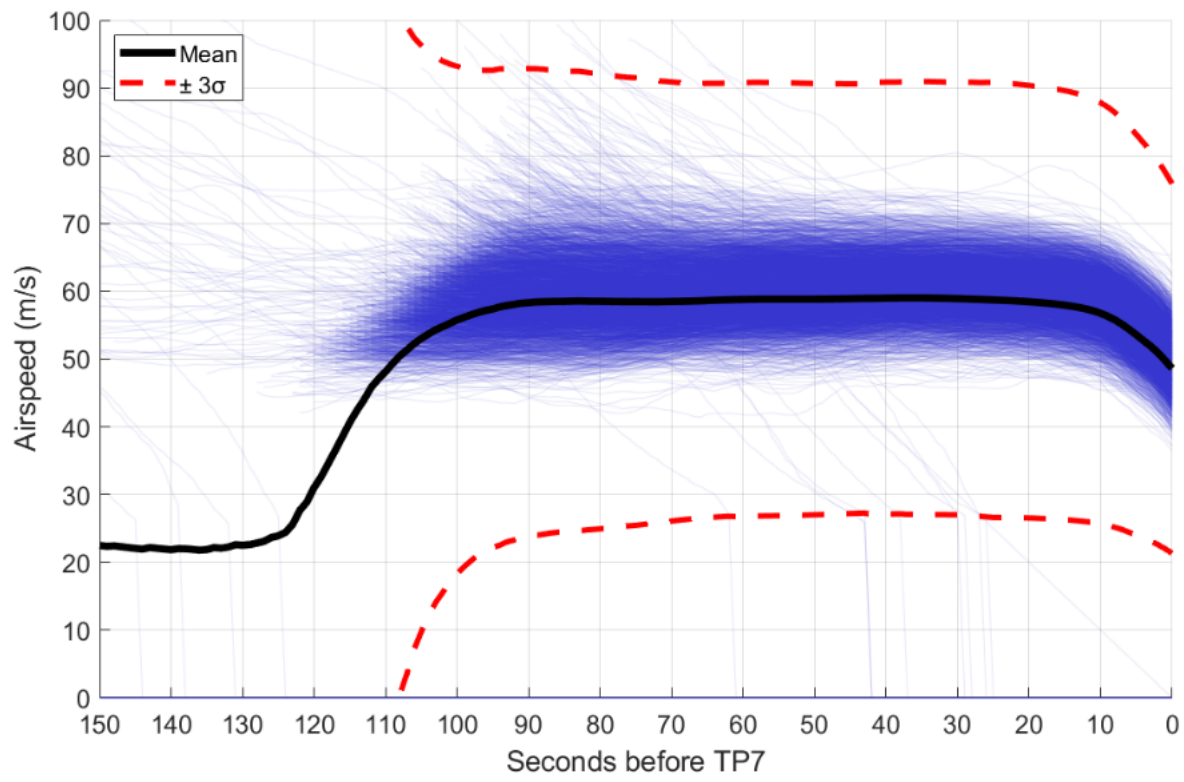


Figure C.3 Airspeed Progression Plot

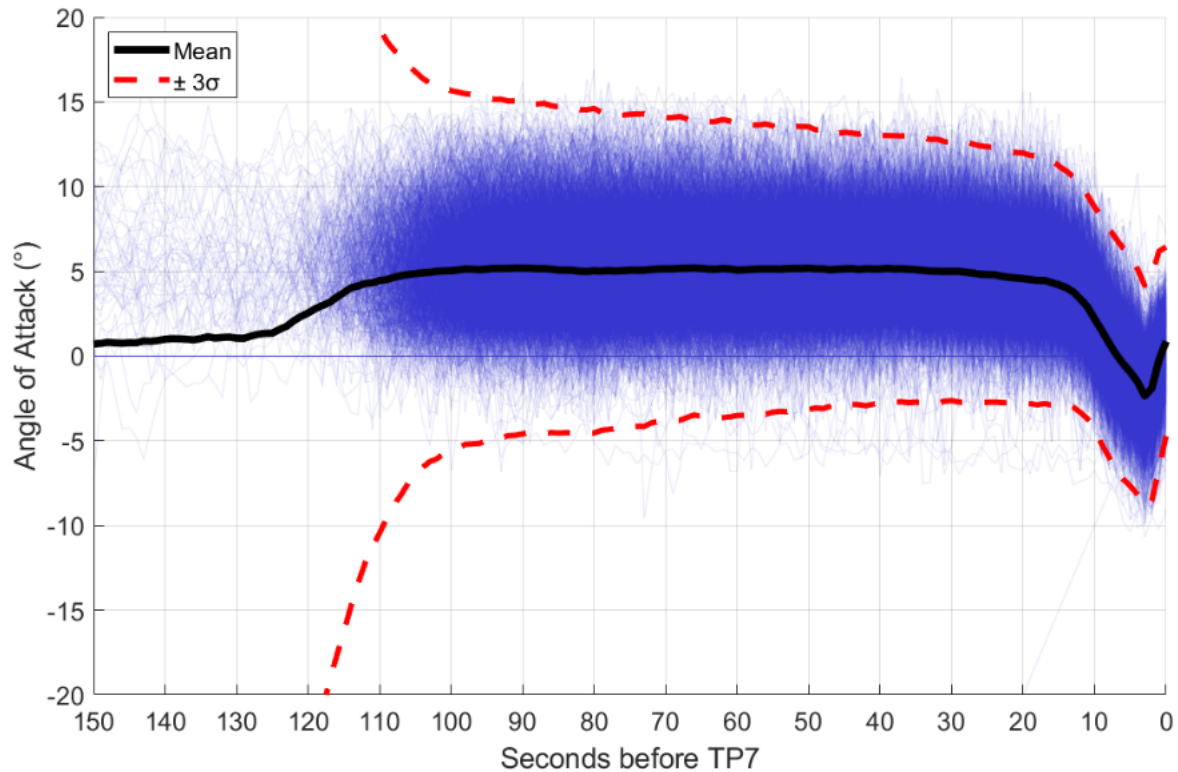


Figure C.4 Angle of Attack Progression Plot

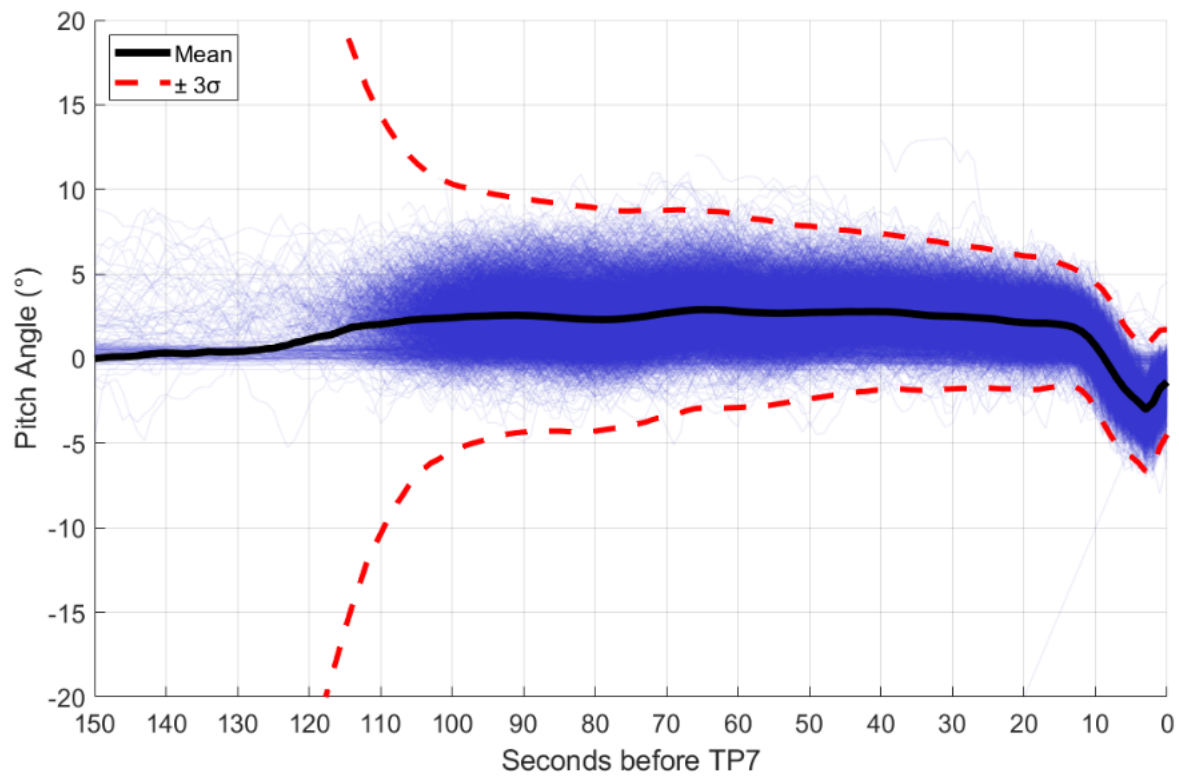


Figure C.5 Pitch Angle Progression Plot

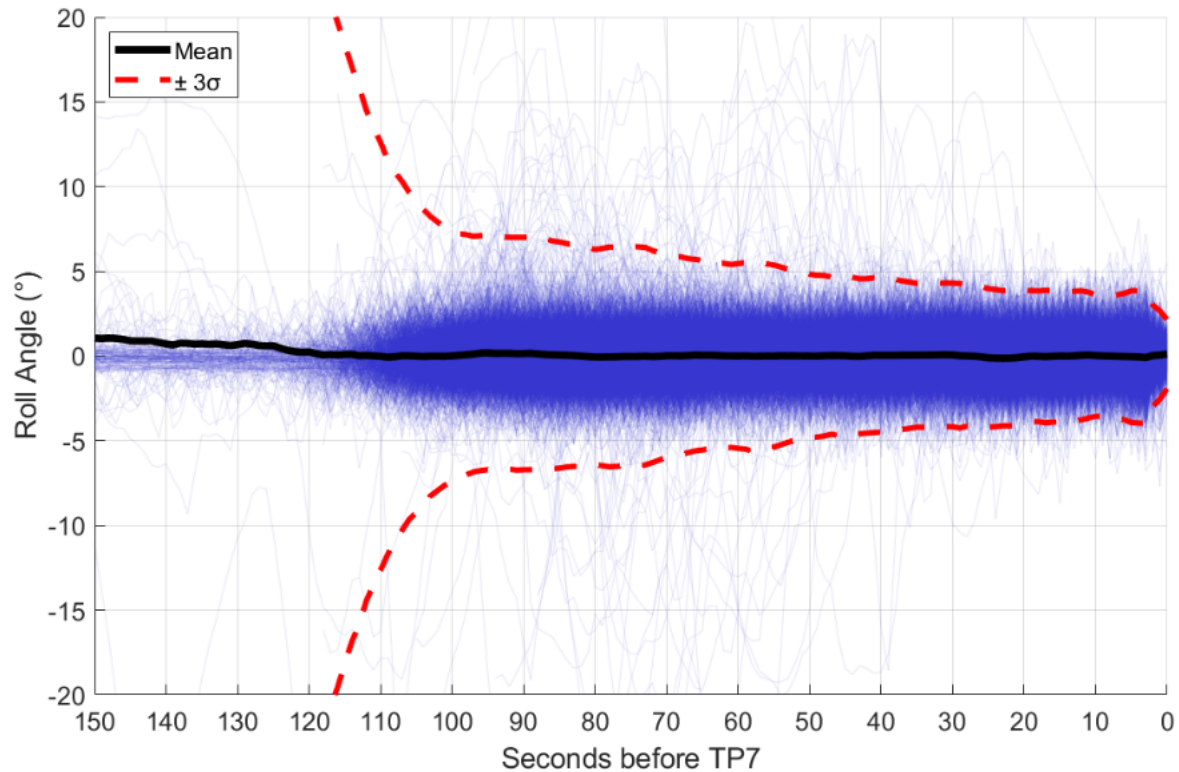


Figure C.6 Roll Angle Progression Plot

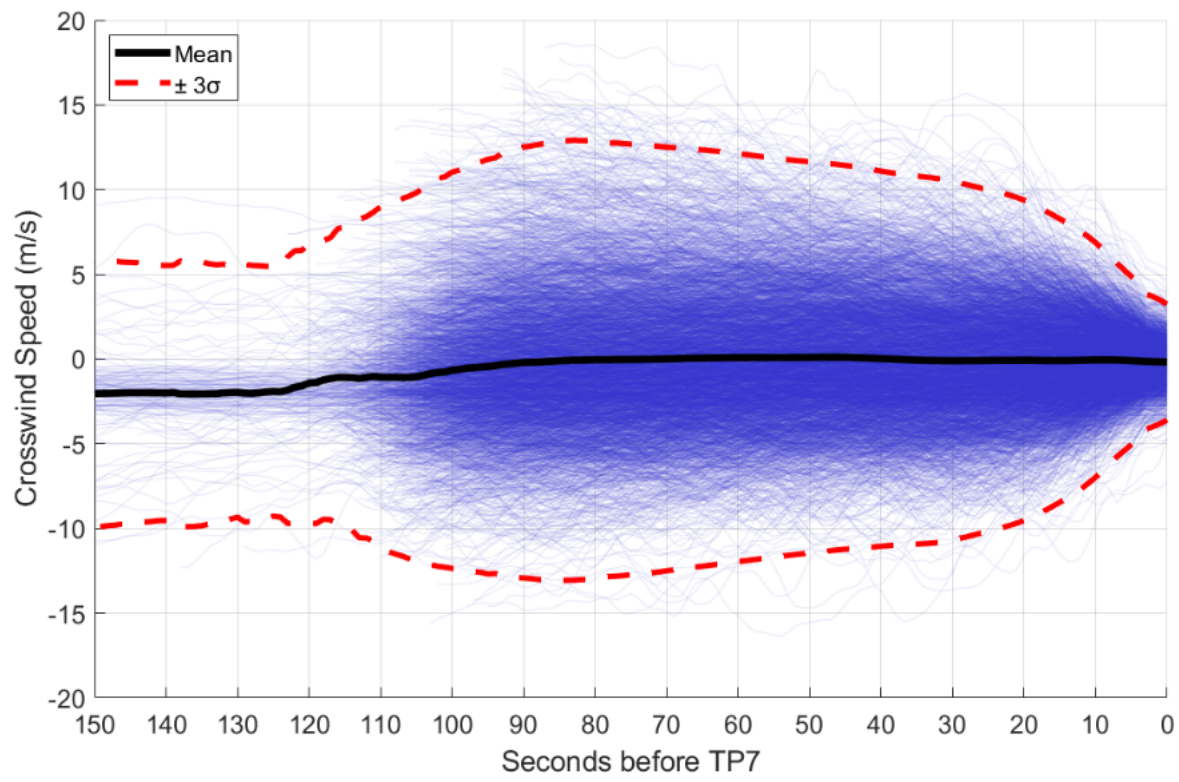


Figure C.7 Crosswind Progression Plot

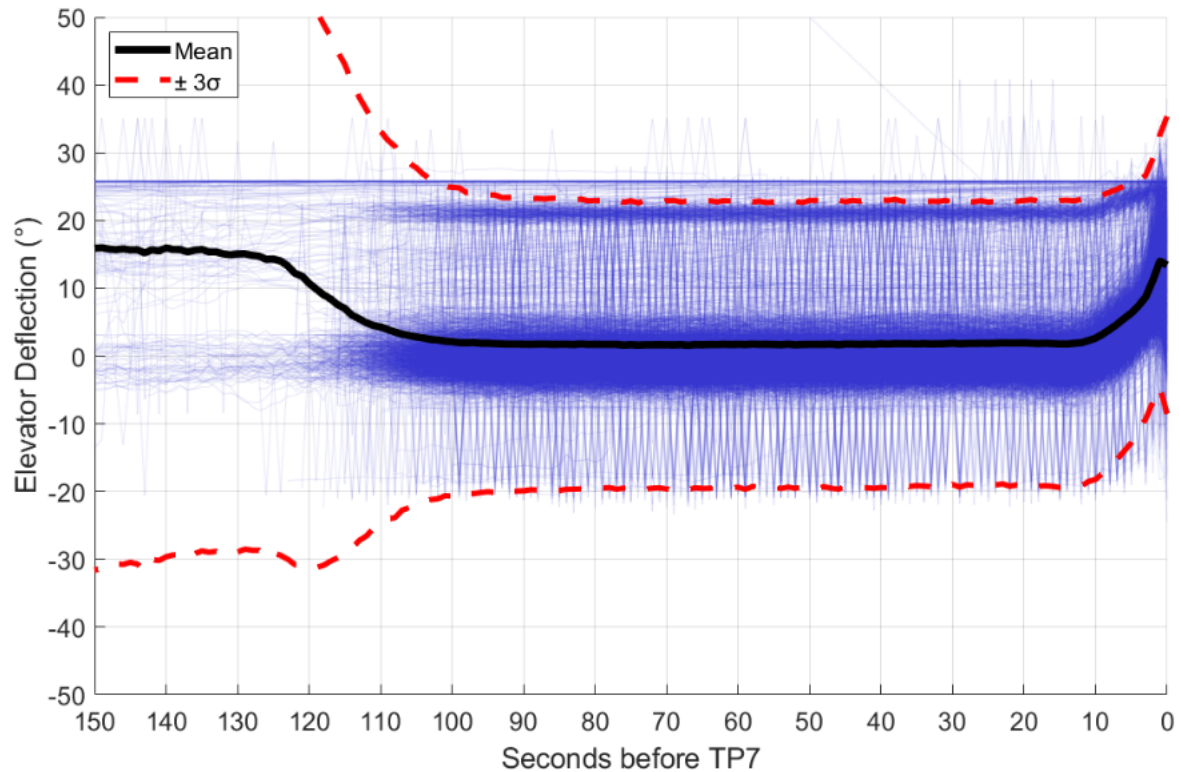


Figure C.8 Elevator Deflection Progression Plot

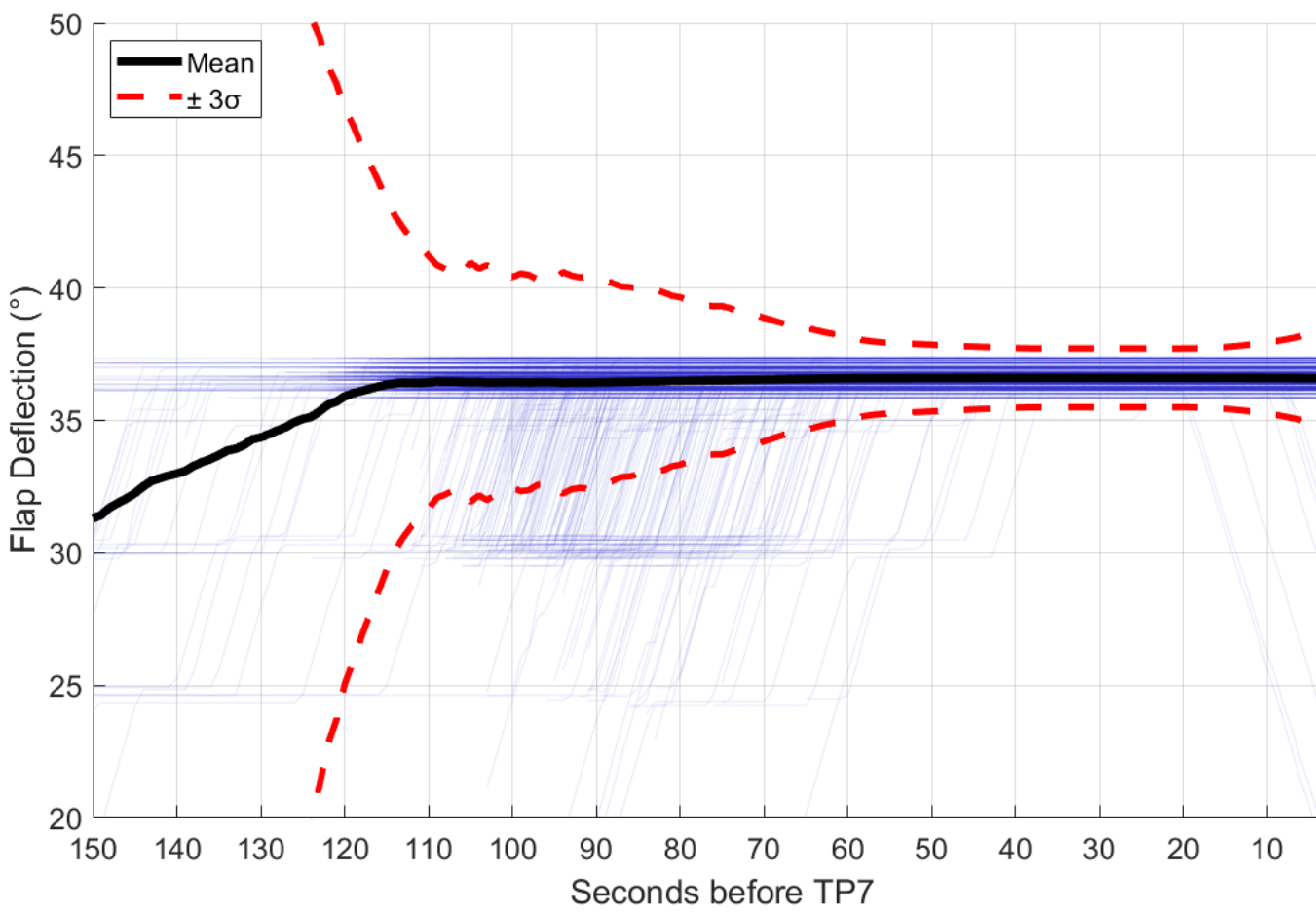


Figure C.9 Flap Deflection Progression Plot

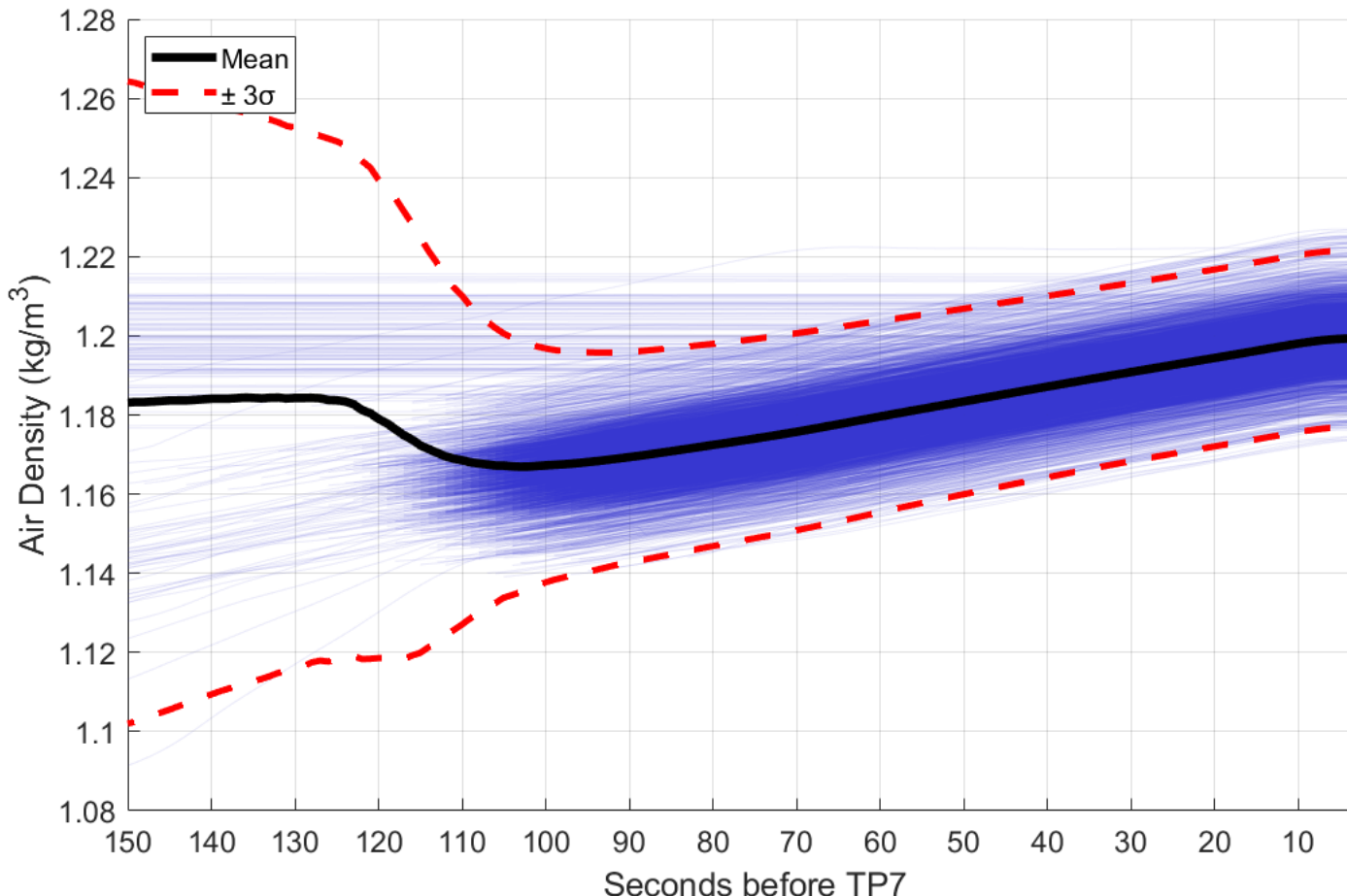


Figure C.10 Air Density Progression Plot